TAMPEREEN TEKNILLINEN YLIOPISTO
TAMPERE UNIVERSITY OF TECHNOLOGY

Mikko J. Huttunen

Second-harmonic Generation with Focused Vector Beams

Julkaisu 1130 • Publication 1130

Tampere 2013

Tampereen teknillinen yliopisto. Julkaisu 1130
Tampere University of Technology. Publication 1130

Mikko J. Huttunen

Second-harmonic Generation with Focused Vector Beams

Thesis for the degree of Doctor of Science in Technology to be presented with due permission for public examination and criticism in Tietotalo Building, Auditorium TB109, at Tampere University of Technology, on the 18th of May 2013, at 12 noon.

Tampereen teknillinen yliopisto - Tampere University of Technology
Tampere 2013

ISBN 978-952-15-3067-8 (printed)
ISBN 978-952-15-3112-5 (PDF)
ISSN 1459-2045

To Laura, Granny & My Family

Abstract

In this work, nonlinear light-matter interactions occurring at the focal volume of a tightly focused laser beam are studied and two new techniques for microscopy are developed. The techniques are based on the nonlinear phenomenon of second-harmonic generation, where two photons at the fundamental frequency combine into a single photon with doubled frequency. A mathematical treatment based on vector diffraction theory is applied for modelling the optical phenomena occurring at the focus. The vector treatment also predicts the occurrence of a new kind of multipolar light-matter interaction, which can lead to considerably large deviations from traditional scalar diffraction approaches. In order to demonstrate the predicted deviations and the capabilities of the developed imaging techniques, a nonlinear microscope is built and utilized.

The first actual microscopy technique is developed to study chiral materials on a microscopic scale. Chirality, or handedness, is a symmetry property which has importance in several branches of science as well as in nature itself. Chiral objects lack mirror symmetry, and can occur in two different configurations, known as enantiomers, which are mirror images of each other. The optical and chemical behaviour of the enantiomers can vary drastically from each other. We show that the developed imaging technique is capable of recognizing chiral objects, such as molecules or nanostructures, from their enantiomers.

The second imaging technique is developed to characterize the optical responses of three-dimensional nanostructures. These tiny man-made structures are utilized in the emerging fields of plasmonics and metamaterials. Recent advances in nanofabrication have made it possible to realize these nanostructures, which may in the future enable the control of light in unprecedented ways at the nanoscale. But these fabricated nanostructures often possess small defects, which may hinder their functionality. We show that by combining polarization-engineered focused vector beams with second-harmonic generation microscopy, we can provide an extremely sensitive tool to study the effects of nanoscale deformations on optical responses. The technique is used to characterize the optical responses of metallic nanocones, where nanoscale defects and deformations are seen to sometimes play a substantial role.

Preface

This work was carried out in the Optics Laboratory of the Tampere University of Technology during the years 2009-2012. I merrily and gratefully acknowledge the financial support from the Graduate School of Modern Optics and Photonics, the Vilho, Yrjö and Kalle Väisälä Foundation, the Emil Aaltonen Foundation and the Academy of Finland.

First, I would like to thank my supervisor, Professor Martti Kauranen, for giving me the opportunity to carry out my research, for guidance, and for being a motivating, positively-minded and supportive supervisor and advisor. I am deeply grateful to my colleagues Godofredo, Jouni, Matti, Miro and Mariusz for the years of working together. Special thanks go to Juha M. Kontio from the Optoelectronics Research Center for making those teeny tiny structures of yours and to Jouni, for providing the hardcore computational and theoretical support. I owe much of my current understanding of physics to the abovementioned. Another source of enlightenment has been the mentoring and teaching of students, so my thanks go also to Timo, Janne, Mari, Domenico, Liisa and the participants of the Optics II course in the fall of 2012. I also want to thank the co-workers and friends from the Aerosol Physics Laboratory, Matti, Juha and Heino for being great friends and even greater lunch company! I would also like to express my gratitude to all the co-workers in our laboratory, especially Sami, Albert, Samu, Jussi, Ville, Tapio, Hannu, Henna and Kalle for keeping up a superfriendly atmosphere in the lab, especially at the coffee room, as well as Inkeri Vänskä and Hanna Kivisaari for helping out with the practicalities in the friendly way you do.

Finally, I want to thank my family: Mom, Dad, Granny, Niko and Eve. In equal amounts, I want to thank my friends and especially my girlfriend Laura for making my life as fun as it is. Although I get easily lost in my work, you people get me back on track and into the real world.

Tampere, April 2013

Mikko J. Huttunen

Contents

List of Figures

List of Abbreviations and Symbols

3D	Three-dimensional
AFM	Atomic force microscopy
AP	Azimuthal polarization
ASR	Angular spectrum representation
BEM	Boundary element method
CARS	Coherent anti-Stokes Raman scattering
CD	Circular dichroism
CVB	Cylindrical vector beam
DCANP	2-docosylamino-5-nitropyridine
DDA	Discrete-dipole approximation
DFG	Difference-frequency generation
FDTD	Finite-difference time-domain
HG	Hermite-Gaussian
LB	Langmuir-Blodgett
LG	Laguerre-Gaussian
NA	Numerical aperture
OA	Optical activity
ORD	Optical rotatory dispersion
RP	Radial polarization

SEM	Scanning electron microscopy
SFG	Sum-frequency generation
SHG-CD	Second-harmonic generation circular dichroism
SHG	Second-harmonic generation
SiN	Silicon-nitride
SLM	Spatial light modulator
TERS	tip-enhanced Raman scattering
THBQ	Tetradodecyloxy-helicenebisquinone
TPL	Two-photon luminescence
VPSF	Vector point-spread function
$\widehat{\mathbf{A}}$	Fourier transform of the field $\mathbf{A}$ with respect to position
$\mathbf{B}$	Magnetic-flux density
c	Speed of light in vacuum
$\mathbf{D}$	Electric displacement
$\mathbf{E}$	Electric field
$\mathbf{E}_\infty$	Electric far-field
f_w	Apodization function
f_0	Filling factor
F	Focal point
$\bar{G}$	Dyadic Green's function
G	Scalar Green's function
$\mathbf{H}$	Magnetic field
$\mathbf{J}$	Free current density
J_n	Bessel function of the first kind and n^{th} order
$\mathbf{k}$	Wave vector
k	Wave number
k_x,k_y,k_z	Cartesian components of wave vector $\mathbf{k}$
$\mathbf{n}_\varrho$,$\mathbf{n}_\phi$,$\mathbf{n}_z$	Unit vectors of cylindrical coordinate system

$\mathbf{n}_r$,$\mathbf{n}_\phi$,$\mathbf{n}_\theta$	Unit vectors of spherical coordinate system
n	Refractive index
$\mathbf{P}$	Polarization
$\mathbf{r}$	Position vector
r,θ,ϕ	Spherical coordinates
$\mathbf{s}$	Dimensionless unit vector in direction of $\mathbf{r}$
t	Time
t^s, t^p	Fresnel transmission coefficients
V	Volume
x,y,z	Cartesian coordinates
$Z_{\mu\epsilon}$	Wave impedance
$\widetilde{\ }$	Quantity that varies rapidly in time, e.g. $\widetilde{\mathbf{E}}$
ρ	Free charge density
ϱ,ϕ,z	Cylindrical coordinates

List of Publications

Paper 1 M. J. Huttunen, M. Erkintalo, and M. Kauranen, "Absolute nonlinear optical probes of surface chirality," Journal of Optics A: Pure and Applied Optics **11**, 034006 (2009).

Paper 2 M. J. Huttunen, M. Virkki, M. Erkintalo, E. Vuorimaa, A. Efimov, H. Lemmetyinen, and M. Kauranen, "Absolute probe of surface chirality based on focused circularly polarized light," The Journal of Physical Chemistry Letters **1**, 1826–1829 (2010).

Paper 3 M. J. Huttunen, G. Bautista, M. Decker, S. Linden, M. Wegener, and M. Kauranen, "Nonlinear chiral imaging of subwavelength-sized twisted-cross gold nanodimers [Invited]," Optical Materials Express **1**, 46–56 (2011).

Paper 4 G. Bautista, M. J. Huttunen, J. Mäkitalo, J. M. Kontio, J. Simonen, and M. Kauranen, "Second-harmonic generation imaging of metal nano-objects with cylindrical vector beams," Nano Letters **12**, 3207–3212 (2012).

Paper 5 M. J. Huttunen, J. Mäkitalo, G. Bautista, and M. Kauranen, "Multipolar second-harmonic emission with focused Gaussian beams," New Journal of Physics **14**, 113005 (2012).

Chapter 1

Introduction

Optical microscopy is an almost 400 year-old invention, but it still attracts considerable scientific attention since the interesting questions in nature as well as in modern science often occur on microscopic, or even smaller, nanoscopic scale. Optical microscopy is a branch of natural science which tries to answer some of those questions by optical means. The field has also been very successful in providing those answers, due to which numerous applications exist in fields ranging from biological imaging [1–3] to the study of man-made nanostructures, such as metamaterials [4,5] or optical antennas [6,7].

Key advances in optical microscopy occurred in the late 1950s and early 1960s, when confocal microscopy were invented [8,9]. The principle of confocal microscopy enabled optical sectioning, solving a key issue in bioimaging, but required more powerful light sources than available at the time. Thus it fully matured to a standard technique only several decades later.

At the same time, the invention of the laser had another profound effect on optical sciences. This effect was the birth of nonlinear optics [10]. In nonlinear optical phenomena, the light-matter interaction depends on several optical fields (or photons in the quantum picture), giving rise to new optical processes. Perhaps the most well-known of such nonlinear phenomena is second-harmonic generation (SHG), where two photons with equal energy combine to form a single photon with doubled energy.

In addition to the fundamental interest, nonlinear optical processes have found a range of applications, including new imaging techniques. The first SHG microscopes were built and demonstrated in the 1970s[11,12]. A true breakthrough occurred in 1990, when two-photon fluorescence (TPL) microscopy was demonstrated to provide intrinsic optical sectioning with reduced photobleching[13]. A decade later, various nonlinear processes have been applied for imaging several biologically relevant systems, demonstrating the feasibility and capabilities of these new nonlinear imaging modalities[14–16]. Especially microscopy modalities based on SHG, due to its simplicity[17–20], and coherent anti-Stokes Raman scattering (CARS), due to its potential in providing chemical sensitivity[21–25], have attracted considerable attention.

Although nonlinear imaging modalities are starting to establish themselves as useful techniques, they are only the tip of the iceberg on recent advances on optical microscopy. One such advance has been the surpassing of the far-field diffraction barrier formulated by Ernst Abbe in 1873.[26] The first experiments where the diffraction barrier was beaten were demonstrated by near-field optical microscopy[27,28]. Other approaches came later, mostly based on the properties of fluorescent probes, which are commonly used in optical microscopies for providing contrast[1,29–31]. But although these super-resolution techniques are revolutionizing biological imaging, they still have their limitations and no single technique can surpass the others[1,31]. In general, these techniques suffer from slow imaging speeds although progress is on the way[32,33]. Another hindrance is that the most applied super-resolution techniques require labelling, although also label-free super-resolution techniques have recently been proposed[34–40]. This restriction does not in general apply to coherent nonlinear techniques such as SHG microscopy. In addition, the nonlinear techniques can provide additional contrast mechanisms and thus new information on the samples under study making them interesting imaging modalities.

To conclude, optical microscopy is undergoing interesting developments. The advent of super-resolution techniques are making their impact on the field. Nevertheless nonlinear techniques still hold their potential and interest, since they are ideally label-free and can provide additional contrast mechanisms and thus new information on the samples under study.

1.1 Aim and Scope of This Work

In nonlinear optical processes, several photons participate in the light-matter interaction. The simplest nonlinear process is SHG, where two photons are combined into a single photon. Unlike for example TPL, SHG is a parametric process. This means that the initial and the final quantum-mechanical states of the material system are identical and no energy is transferred to the system [41]. Due to this, parametric processes occur sufficiently rapidly and the interacting photons retain their coherence properties. This is important, since it for example gives rise to the extreme sensitivity of second-order processes, such as SHG, to the symmetry properties of the material system. For example, SHG is within the electric dipole approximation forbidden from centrosymmetric media, but is allowed from surfaces or interfaces [41]. In general, the structural symmetry of the material and the polarization of the incident light dictate the optical responses. Thus, information of the structural properties of the material can be extracted by techniques based on polarization measurements.

At the beginning of this work in 2009, our laboratory had a strong background in studying nonlinear light-matter interactions, and had developed several nonlinear characterization techniques to study molecular thin films and nanostructures. We were also very interested in trying to understand the nonlinear optical processes occuring in very small length scales, for example to study individual nanostructures, but had no real expertise in performing microscopy experiments. The aim of this work was thus to develop new polarization-based nonlinear techniques to study materials on a microscopic scale.

But combining polarization measurements and microscopy is not trivial, since the measurement geometry in microscopy is more restricted than in traditional techniques. For example, the field component along the surface normal usually plays an important role in the polarization-based SHG techniques, and can be easily controlled when collimated or weakly focused beams at oblique angles of incidence are used. However, in microscopy the samples are placed at normal angles of incidence with respect to the input beam, which limits the degrees of freedom to control the excitation field. Thus new degrees of freedom to control the excitation field in three dimensions were needed. To achieve this, we planned to utilize tightly focused and polarized higher-order laser modes. A known example of such modes is radial polarization (RP) [42–46]. Unlike with traditional polarizations, tightly focused RP beam results in a strong field component

along the direction of propagation. Thus we thought it worthwhile to study in more detail, whether these more exotic modes and polarization distributions could provide us the tools for three-dimensional (3D) field control. First, we needed to implement the mathematical tools to model the phenomena occurring at the focal volume of a microscopic setup while using these higher-order modes. Then, a nonlinear stage-scanning microscope was built. Finally, two new polarization-based techniques for microscopy were developed and utilized to study molecular thin films and nanostructures.

1.2 Structure of the Thesis

In this Thesis, nonlinear light-matter interactions at the focal volume of tightly focused laser beams are studied. First, some fundamental aspects of nonlinear optics and the underlying mathematics are presented in Chapter 2. The emphasis is on second-order effects, which are especially sensitive to symmetry properties of matter. This sensitivity to symmetry is the cornerstone of this Thesis, which is utilized in the developed microscopy techniques.

In Chapter 3, the mathematical treatment to describe the 3D electromagnetic field in the focal volume of tightly focused laser beams is formulated. The treatment is based on vector diffraction theory, making possible the full tensorial treatment of nonlinear light-matter interactions introduced in Chapter 2.

Chapter 4 combines the previously introduced mathematics to formulate a model to describe the tensorial nonlinear light-matter interactions at the focal volume of a focused laser beam. Also, the propagation of light out of the focal volume is formulated by using Green's function approach. The latter part of Chapter 4 discusses experimental arrangements and briefly reviews the main results of this Thesis.

Finally, state of the current work, potential applications as well as possible future research directions are discussed in Chapter 5.

1.3 Author's Contribution

This Thesis consists of five papers. **Papers 1-3** deal with the development of a microscopy technique to distinguish chiral and achiral materials and their enantiomers from each other. In **Paper 4**, we demonstrate a technique to optically probe defects and deformations of 3D metal nanostructures. **Paper 5** provides an example of new phenomena that may arise when light is fully treated as a vector quantity. The subjects of the articles included in the Thesis and their key results are:

Paper 1 This paper formulates a theoretical description for second-order nonlinear light-matter interactions for chiral and anisotropic surfaces under tight focusing illumination. Three different microscopic techniques to probe the chirality of surfaces are proposed. The techniques are shown to be unambiguous in the sense, that material anisotropy and chirality can be distinguished from each other. SHG responses are modelled forming the theoretical basis for the experimental work in **Paper 2** and **Paper 3**.

Paper 2 This paper describes the proof-of-principle experiments and results for one of the techniques proposed in **Paper 1**. We measure SHG responses from two different molecular thin films, both being anisotropic, but only one being chiral. The proposed technique is demonstrated to be unambiguous in the sense that it can differentiate possible in-plane anisotropy from possible chirality of the sample.

Paper 3 In this paper, we apply the previously developed technique (**Papers 1-2**) to perform nonlinear microscopy of chiral metal nanostructures. We demonstrate that the technique can be used to probe the chirality of individual nano-objects, and study the role of defects to the measured SHG signals.

Paper 4 In this paper, the previously found sensitivity of SHG towards defects in metal nanostructures is studied in greater depth. Gold nanocones are fabricated and individual cones are imaged by scanning electron microscopy and SHG microscopy. The measurements are complemented by rigorous state-of-the-art nonlinear modelling.

Paper 5 In this paper, we demonstrate that full vector treatment of light can lead to interference phenomena and directional emission, which is not predicted by traditional scalar treatments. We demonstrate the effect by measuring strongly asymmetric second-harmonic emission from thin silicon nitride films. The phenomenon is interpreted as a new form of multipolar light-matter interactions.

All the results in this work, as is usual in science, arise from collaborations and team effort. The author's contribution to each of the Papers is shown in Table 1.1. The contribution is divided into three categories; **Preparation**, **Experiments**, and **Reporting**. Preparation consists of theory, design and evaluation of the experimental method, experiments includes the implementation of the experimental method and the actual experimental work. Reporting contains the data analysis and the preparation of the manuscript.

Table 1.1. Summary of author's contribution to articles included in this Thesis.

Paper	Preparation	Experiments	Reporting
Paper 1	70 %	90 %	70 %
Paper 2	60 %	80 %	80 %
Paper 3	60 %	80 %	70 %
Paper 4	50 %	75 %	20 %
Paper 5	80 %	90 %	70 %

Chapter 2

Nonlinear Optics

Nonlinear optics is an active sub-field of modern optics. Since the first experimental demonstration of nonlinear optical phenomena in 1961,[10] the field has contributed enormously to the development of new optical applications. In this Chapter, we introduce the fundamentals of nonlinear optics by starting from Maxwell's equations and the parameters that describe the optical responses of materials, the susceptibilities. In this Chapter, we also describe how different symmetries can influence the nonlinear optical phenomena.

2.1 Maxwell's Equations and the Nonlinear Wave Equation

The propagation of electromagnetic radiation can be described classically by the wave equation derived from Maxwell's equations. When radiation propagates inside a medium, the optical properties of this medium need to be considered. This is taken into account by introducing proper constitutive relations, which describe how the material response depends on the electromagnetic fields. Next, a wave equation is derived to describe the nonlinear light-matter interaction by starting from Maxwell's equations using the notation of the classic Boyd's book on nonlinear optics[41].

Maxwell's equations can be written in SI-units as*

$$\begin{aligned} \nabla\cdot\widetilde{\mathbf{D}} &= \tilde{\rho}, & \nabla\times\widetilde{\mathbf{E}} &= -\frac{\partial\widetilde{\mathbf{B}}}{\partial t}, \\ \nabla\cdot\widetilde{\mathbf{B}} &= 0, \qquad \text{and} & \nabla\times\widetilde{\mathbf{H}} &= \frac{\partial\widetilde{\mathbf{D}}}{\partial t}+\widetilde{\mathbf{J}}, \end{aligned} \tag{2.1}$$

where $\widetilde{\mathbf{D}}$ and $\widetilde{\mathbf{E}}$ are the electric displacement and field, respectively. Similarly $\widetilde{\mathbf{B}}$ denotes the magnetic-flux density and $\widetilde{\mathbf{H}}$ is the magnetic field. $\tilde{\rho}$ and $\widetilde{\mathbf{J}}$ are the free charge density and the free current density, respectively. By assuming that the medium is dielectric, the free charge and current densities vanish. By assuming the medium to be also non-magnetic, the constitutive relations can be written as

$$\widetilde{\mathbf{D}} = \epsilon_0\widetilde{\mathbf{E}}+\widetilde{\mathbf{P}}, \qquad \text{and} \qquad \widetilde{\mathbf{B}} = \mu_0\widetilde{\mathbf{H}}, \tag{2.2}$$

where $c = 1/\sqrt{\epsilon_0\mu_0}$ and $\widetilde{\mathbf{P}}$ is polarization. Now by taking curl of the $\nabla\times\widetilde{\mathbf{E}}$ and using Eqs. (2.1) and (2.2), we obtain the expression

$$\nabla\times\nabla\times\widetilde{\mathbf{E}}+\frac{1}{c^2}\frac{\partial^2\widetilde{\mathbf{E}}}{\partial^2 t} = -\frac{1}{\epsilon_0 c^2}\frac{\partial^2\widetilde{\mathbf{P}}}{\partial t^2}, \tag{2.3}$$

which is a general form of the wave equation. We can simplify this equation further by assuming that the electric field is a transverse plane wave, for which $\nabla\cdot\widetilde{\mathbf{E}} = 0$. Then we can write Eq. (2.3) using the vector identity $\nabla\times\nabla\times\mathbf{A} = \nabla(\nabla\cdot\mathbf{A})-\nabla^2\mathbf{A}$ as

$$\nabla^2\widetilde{\mathbf{E}}-\frac{1}{c^2}\frac{\partial^2\widetilde{\mathbf{E}}}{\partial^2 t} = \frac{1}{\epsilon_0 c^2}\frac{\partial^2\widetilde{\mathbf{P}}}{\partial t^2}. \tag{2.4}$$

Next, we decompose the polarization and the displacement into their linear and non-linear parts

$$\widetilde{\mathbf{P}} = \widetilde{\mathbf{P}}^{(1)}+\widetilde{\mathbf{P}}^{\mathrm{NL}}, \qquad \text{and} \qquad \widetilde{\mathbf{D}} = \widetilde{\mathbf{D}}^{(1)}+\widetilde{\mathbf{P}}^{\mathrm{NL}}, \tag{2.5}$$

where the linear parts $\widetilde{\mathbf{P}}^{(1)}$ and $\widetilde{\mathbf{D}}^{(1)}$ are interrelated through the definition:

$$\widetilde{\mathbf{D}}^{(1)} = \epsilon_0\widetilde{\mathbf{E}}+\widetilde{\mathbf{P}}^{(1)}. \tag{2.6}$$

*We denote quantities that vary rapidly in time by a tilde (~).

Eq. (2.4) can now be written using Eqs. (2.5) and (2.6) as

$$\nabla^2\widetilde{\mathbf{E}} - \frac{1}{\epsilon_0 c^2}\frac{\partial^2\widetilde{\mathbf{D}}^{(1)}}{\partial^2 t} = \frac{1}{\epsilon_0 c^2}\frac{\partial^2\widetilde{\mathbf{P}}^{\mathrm{NL}}}{\partial t^2}. \tag{2.7}$$

Now by considering first the case of a lossless and dispersionless medium, using a real and frequency-independent dielectric tensor $\epsilon^{(1)}$ we can write the relation of Eq. (2.6) into form

$$\widetilde{\mathbf{D}}^{(1)} = \epsilon_0\epsilon^{(1)}\cdot\widetilde{\mathbf{E}}, \tag{2.8}$$

where $\epsilon^{(1)}$ depends on the properties of the material. Now the wave equation can be written as

$$\nabla^2\widetilde{\mathbf{E}} - \frac{1}{c^2}\epsilon^{(1)}\cdot\frac{\partial^2\widetilde{\mathbf{E}}}{\partial^2 t} = \frac{1}{\epsilon_0 c^2}\frac{\partial^2\widetilde{\mathbf{P}}^{\mathrm{NL}}}{\partial t^2}. \tag{2.9}$$

From this form of inhomogeneous wave equation, we can see that the nonlinear part of the polarization acts as a source for new electromagnetic radiation.

In general, the polarization of the medium cannot respond instantaneously. The time-dependent response can be taken into account by replacing Eq. (2.8) by a convolutional constitutive relationship:

$$\widetilde{\mathbf{D}}^{(1)}(t) = \int_{-\infty}^{\infty}\epsilon_0\epsilon^{(1)}(t-t')\cdot\widetilde{\mathbf{E}}(t')\mathrm{d}t', \tag{2.10}$$

where due to causality $\epsilon^{(1)}(t-t') = 0$ for $t' > t$. This also means that the permittivity tensor becomes frequency-dependent, i.e., the medium becomes dispersive. We therefore must formulate the wave equation separately for each frequency component. To proceed, we write the electric field, the electric displacement and the nonlinear polarization as sums of their frequency components by defining the following Fourier transforms

$$\widetilde{\mathbf{A}}(t) = \int_{-\infty}^{\infty}\mathbf{A}(\omega)\mathrm{e}^{-i\omega t}\mathrm{d}\omega, \tag{2.11a}$$

$$\mathbf{A}(\omega) = \frac{1}{2\pi}\int_{-\infty}^{\infty}\widetilde{\mathbf{A}}(t)\mathrm{e}^{i\omega t}\mathrm{d}t, \tag{2.11b}$$

where $\mathbf{A}$ is any of the field quantities $\mathbf{E}$, $\mathbf{D}^{(1)}$, or $\mathbf{P}^{\mathrm{NL}}$. Since the fields are physically measurable quantities, we require $\mathbf{E}(-\omega) = \mathbf{E}(\omega)^*$ where $(^*)$ stands for complex conjugation. Now using the convolution theorem and Eq. (2.11b) we get a multiplicative

relationship for Eq. (2.10) in the frequency domain

$$\mathbf{D}^{(1)}(\omega) = \epsilon_0 \epsilon^{(1)}(\omega) \cdot \mathbf{E}(\omega), \tag{2.12}$$

where $\epsilon^{(1)}(\omega)$ stands for expression:

$$\epsilon^{(1)}(\omega) = \int_{-\infty}^{\infty} \epsilon^{(1)}(t) \mathrm{e}^{i\omega t} \mathrm{d}t. \tag{2.13}$$

Using Eqs. (2.11) and (2.12) we can then write Helmholtz equation analogous to Eq. (2.7) which holds separately for each frequency component:

$$\nabla^2 \mathbf{E}(\omega) + \frac{\omega^2}{c^2} \epsilon^{(1)}(\omega) \cdot \mathbf{E}(\omega) = -\frac{\omega^2}{\epsilon_0 c^2} \mathbf{P}^{\mathrm{NL}}(\omega). \tag{2.14}$$

2.2 Nonlinear Optical Phenomena

In the previous section we saw how the nonlinear polarization can give rise new electromagnetic radiation. Here, we focus on the structure and properties of the nonlinear polarization in more detail. We start by assuming that the incident field $\mathbf{E}$ is sufficiently weak so that we can expand the nonlinear polarization into power series. Then we can write Eq. (2.5) in a general convolutional way [47]

$$\begin{aligned}
\widetilde{\mathbf{P}}(\mathbf{r},t) =& \widetilde{\mathbf{P}}^{(1)}(\mathbf{r},t) + \widetilde{\mathbf{P}}^{(2)}(\mathbf{r},t) + \widetilde{\mathbf{P}}^{(3)}(\mathbf{r},t) + \cdots && \text{(2.15a)} \\
=& \int_{-\infty}^{\infty} \epsilon_0 \chi^{(1)}(\mathbf{r}-\mathbf{r}', t-t') \cdot \widetilde{\mathbf{E}}(\mathbf{r}',t') \mathrm{d}\mathbf{r}' \mathrm{d}t' && \text{(2.15b)} \\
&+ \int_{-\infty}^{\infty} \epsilon_0 \chi^{(2)}(\mathbf{r}-\mathbf{r}_1, t-t_1; \mathbf{r}-\mathbf{r}_2, t-t_2) : \\
&\qquad \widetilde{\mathbf{E}}(\mathbf{r}_1,t_1) \widetilde{\mathbf{E}}(\mathbf{r}_2,t_2) \mathrm{d}\mathbf{r}_1 \mathrm{d}t_1 \mathrm{d}\mathbf{r}_2 \mathrm{d}t_2 && \text{(2.15c)} \\
&+ \int_{-\infty}^{\infty} \epsilon_0 \chi^{(3)}(\mathbf{r}-\mathbf{r}_1, t-t_1; \mathbf{r}-\mathbf{r}_2, t-t_2; \mathbf{r}-\mathbf{r}_3, t-t_3) \vdots \\
&\qquad \widetilde{\mathbf{E}}(\mathbf{r}_1,t_1) \widetilde{\mathbf{E}}(\mathbf{r}_2,t_2) \widetilde{\mathbf{E}}(\mathbf{r}_3,t_3) \mathrm{d}\mathbf{r}_1 \mathrm{d}t_1 \mathrm{d}\mathbf{r}_2 \mathrm{d}t_2 \mathrm{d}\mathbf{r}_3 \mathrm{d}t_3 && \text{(2.15d)} \\
&+ \cdots,
\end{aligned}$$

where $\widetilde{\mathbf{P}}^{(n)}$ and $\chi^{(n)}$ are the nth-order polarization and susceptibility, respectively. The susceptibilities are thus material parameters, which describe the optical properties

of the medium. Next we assume that in our cases of interest the electric dipole approximation holds[47,48]. Then $\chi^{(n)}(\mathbf{r},t)$ are independent of $\mathbf{r}$ and thus their Fourier transforms

$$\begin{aligned}\chi^{(n)}&(\mathbf{k}=\mathbf{k}_1+\mathbf{k}_2+...+\mathbf{k}_n,\omega=\omega_1+...+\omega_n)\\&=\int_{-\infty}^{\infty}\chi^{(n)}(\mathbf{r}-\mathbf{r}_1,t-t_1;...;\mathbf{r}-\mathbf{r}_n,t-t_n)\\&\times\mathrm{e}^{-i[\mathbf{k}_1(\mathbf{r}-\mathbf{r}_1)-\omega_1(t-t_1)+...+\mathbf{k}_n(\mathbf{r}-\mathbf{r}_n)-\omega_1(t-t_n)]}\mathrm{d}\mathbf{r}_1\mathrm{d}t_1...\mathrm{d}\mathbf{r}_n\mathrm{d}t_n,\end{aligned}\tag{2.16}$$

are independent of $\mathbf{k}$. The convolutional form of polarization given by Eq. (2.15) can then be Fourier transformed and simplified to

$$\mathbf{P}(\omega)=\mathbf{P}^{(1)}(\omega)+\mathbf{P}^{(2)}(\omega)+\mathbf{P}^{(3)}(\omega)+\cdots\tag{2.17a}$$

$$=\epsilon_0\chi^{(1)}(\omega)\cdot\mathbf{E}(\omega)\tag{2.17b}$$

$$+\epsilon_0\chi^{(2)}(\omega=\omega_1+\omega_2)\vdots\,\mathbf{E}(\omega_1)\mathbf{E}(\omega_2)\tag{2.17c}$$

$$+\epsilon_0\chi^{(3)}(\omega=\omega_1+\omega_2+\omega_3)\vdots\,\mathbf{E}(\omega_1)\mathbf{E}(\omega_2)\mathbf{E}(\omega_3)\tag{2.17d}$$

$$+\cdots,$$

where $\chi^{(n)}(\omega)$ and $\mathbf{E}(\omega)$ are the frequency domain representations of the susceptibilities and the electric fields, respectively. From this form we see that, e.g., two incident fields at frequencies ω_1 and ω_2 can interact with the medium to create an oscillating polarization (and thus radiating field) at the third frequency $\omega=\omega_1+\omega_2$. In general, two different new frequencies are possible

$$\mathbf{P}^{(2)}(\omega_1+\omega_2)=\epsilon_0\chi^{(2)}(\omega_1+\omega_2)\vdots\,\mathbf{E}(\omega_1)\mathbf{E}(\omega_2)\,,\tag{2.18}$$

$$\mathbf{P}^{(2)}(\omega_1-\omega_2)=\epsilon_0\chi^{(2)}(\omega_1-\omega_2)\vdots\,\mathbf{E}(\omega_1)\mathbf{E}^*(\omega_2)\,,\tag{2.19}$$

where the consequent processes are called sum-frequency generation (SFG) and difference-frequency generation (DFG). When the frequencies are equal ($\omega_1=\omega_2=\omega$), the processes degenerate into SHG and optical rectification, respectively. And since two interacting fields are responsible for the generated polarizations, the occurring processes are of second order.

2.3 Second-order Effects and Symmetry

In the previous sections, the susceptibilities were introduced as the material parameters describing the nonlinear light-matter interactions. Next, we consider the properties of the susceptibilities in more detail. The emphasis will be on second-order processes and the effects of symmetries on those processes.

We start by assuming that two electric fields at frequencies ω_1 and ω_2 interact with the nonlinear medium and the second-order process of SFG occurs. The interaction can be described by rewriting Eq. (2.18) as

$$P_i^{(2)}(\omega_1+\omega_2) = \epsilon_0 \sum_{jk} \sum_{(1,2)} \chi_{ijk}^{(2)}(\omega_1+\omega_2;\omega_1,\omega_2) E_j(\omega_1) E_k(\omega_2), \tag{2.20}$$

where i, j and k correspond to Cartesian components (x, y, z). First, we see that since the interacting fields are vectors, the susceptibility is a tensor consisting of $3^3 = 27$ components[†]. Due to the mathematical notation, and the physical reality, we can equate tensor components for which the Cartesian components and the frequency components are permuted simultaneously, i.e., we can write

$$\chi_{ijk}^{(2)}(\omega_1+\omega_2;\omega_1,\omega_2) = \chi_{ikj}^{(2)}(\omega_2+\omega_1;\omega_2,\omega_1). \tag{2.21}$$

This is known as *intrinsic permutation symmetry*. It is due to the fact that the order of the fields in Eq. (2.20) should not change the physical outcome. For the case of SHG the input fields are not separable from each other ($\omega_1 = \omega_2 = \omega$), and the condition of Eq. (2.21) simplifies into

$$\chi_{ijk}^{(2)}(2\omega;\omega,\omega) = \chi_{ikj}^{(2)}(2\omega;\omega,\omega), \tag{2.22}$$

reducing the number of independent tensor components to 18[‡].

Next we consider how spatial symmetry of the medium can affect its nonlinear responses. If the nonlinear medium remains unchanged under a certain transformation, such as rotation or reflection, then neither can its physical response change. The

[†]Compared to linear processes, which can be described by matrices, i.e. using $3^2 = 9$ components.

[‡]By assuming negligible dispersion ($\frac{\mathrm{dn}}{\mathrm{d}\omega} = 0$) for the susceptibility, the same condition applies also for SFG. In fact, negligible dispersion leads to *Kleinman's symmetry condition*, where the indices of the susceptibility can be freely permuted.

corresponding transformation is then a symmetry operation, which can be utilized to impose further restrictions to the susceptibility tensor.

Centrosymmetric Medium

We start by considering the second-order response of a centrosymmetric medium, for which an inversion center exist. Such medium is invariant under parity transformation ($\mathbf{r} \to -\mathbf{r}$). For simplicity we assume that the medium responds immediately to the incident fields and we consider only SHG, but the result holds also for other second-order processes. The nonlinear polarization is then

$$\widetilde{\mathbf{P}}^{(2)}(2\omega) = \epsilon_0 \chi^{(2)} \widetilde{\mathbf{E}}^2(\omega). \tag{2.23}$$

By inverting the excitation field we end up with a similar equation

$$-\widetilde{\mathbf{P}}^{(2)}(2\omega) = \epsilon_0 \chi^{(2)} (-\widetilde{\mathbf{E}})^2(\omega) = \epsilon_0 \chi^{(2)} \widetilde{\mathbf{E}}^2(\omega), \tag{2.24}$$

where the sign of the polarization is also changed due to the inversion. But since physically nothing changes, these equations must be equal. This can hold only if $\chi^{(2)} = 0$, meaning that SHG is forbidden in centrosymmetric media.

Isotropic Surface

As a next example, we assume that our nonlinear medium is an isotropic, achiral surface in vacuum belonging thus to a symmetry group of $C_{\infty v}$ [Fig. 2.1(a)]. Such a surface is uniform in all directions along the surface, and the corresponding symmetry operations are thus all rotations with respect to the surface normal, and all mirror operations in planes including the surface normal. Thus the only thing breaking the symmetry is the fact that we're now considering a *surface*, i.e., an interface exists between the vacuum and the medium. For the case of SHG the resulting susceptibility of the surface then consists of only three non-zero independent components, which can

be written as

$$\begin{aligned} zzz, \\ zxx = zyy, \\ xxz = xzx = yyz = yzy, \end{aligned} \tag{2.25}$$

where z points along the surface normal and x and y along the surface. Thus second-order processes are always allowed at interfaces [49–51], due to which they can be utilized to study surfaces.

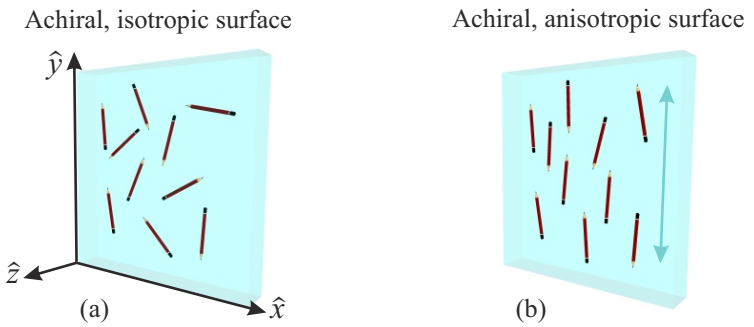

Figure 2.1 Achiral, (a) isotropic and (b) anisotropic surfaces. For achiral surfaces, there exists a mirror operation in planes including the surface normal. For isotropic surfaces, any rotation with respect to the surface normal (z) is also a symmetry operation. For anisotropic surfaces, only some of the rotations along the surface normal are symmetry operations.

Anisotropic Surface

We next assume a surface for which some of the rotations with respect to the surface normal are no longer symmetry operations, making the surface anisotropic. An example where the surface has only 180° rotational symmetry is illustrated in Fig. 2.1(b). For anisotropic surfaces, the non-zero components of the susceptibility are

$$\begin{aligned} zzz, \\ zxx \quad , \quad zyy, \\ xxz = xzx \quad , \quad yyz = yzy. \end{aligned} \tag{2.26}$$

Clearly $x \neq y$ and thus the equality between the zxx and zyy components or xxz and yyz components no longer holds. Due to this, the number of independent components

increases to five from the case of the susceptibility of isotropic and achiral surfaces.

Chiral Surface

Chirality is another important symmetry property, which to be precise is lack of mirror symmetry [see illustration in Fig. 2.2(a),(b)]. Chirality is commonly referred to as handedness, since a hand is a familiar example of a chiral object. Chiral objects and their mirror images are called *enantiomorphs* (or enantiomers)¶. Objects possessing some mirror symmetry are called achiral objects. Chirality is an intriguing property of nature and is of fundamental interest especially in chemistry and in biology, since different enantiomers of chiral molecules can have substantially different biochemical and physiological properties[52].

If we consider a chiral isotropic surface [Fig. 2.2(d)], the second-order susceptibility for the case of SHG consists of four independent and non-zero susceptibility components

$$\begin{aligned} zzz, \\ zxx = zyy, \\ xxz = xzx = yyz = yzy, \\ xyz = xzy = -yxz = -yzx, \end{aligned} \tag{2.27}$$

where the last components are due to the surface chirality. An important aspect of this is that in nonlinear optics the light-matter interactions associated with chirality are allowed also in the electric dipole approximation[48], which does not generally hold for linear light-matter interactions[53]. Thus, although in general nonlinear light-matter interactions are weaker than linear interactions, their relative strength can be considerably higher facilitating development of more sensitive measurement techniques.

To conlude, second-order processes are strongly affected by the symmetry of the medium and this fact can be utilized in developing new nonlinear optical characterization techniques. These concepts related to symmetry and applying that knowledge were also one of the cornerstones of this Thesis.

¶More precisely, term enantiomer usually refers to chiral molecules, and term enantiomorph refers to chiral objects in general. The consequent transformation between the two enantiomorphs is the parity transformation. Electromagnetism is invariant under parity transformation i.e., the laws of electromagnetism are not handed.

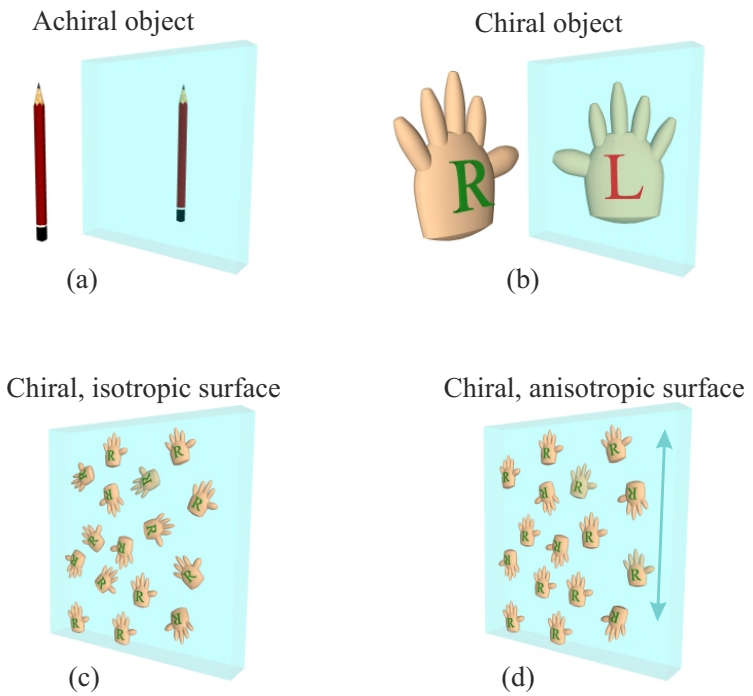

Figure 2.2 (a) Achiral and (b) chiral objects behave differently under reflection operation. (c-d) Chiral surfaces lack mirror symmetry. (d) For chiral anisotropic surfaces, only some of the rotations along the surface normal are symmetry operations.

Chapter 3

Focused Laser Beams

In this Chapter, we introduce the mathematical tools to describe tightly focused laser beams. When light is tightly focused, the regular scalar diffraction approaches are no longer accurate, but a full vector description of the propagating electromagnetic field is needed. We start from the basics of Fourier optics and the well-known angular spectrum representation (ASR) of optical fields in terms of plane waves, and proceed to describe the tight focusing of laser beams using vector diffraction theory. For this, we mainly adopt the approach presented by Novotny and Hecht [54].

3.1 Angular Spectrum Representation

We start by taking the wave equation of Eq. (2.4), and assume propagation of light in a homogeneous and source-free medium, i.e., that $\widetilde{\mathbf{P}} = 0$. We assume that the electric field of interest propagates mainly along z-axis, and is of the form $\widetilde{\mathbf{E}}(\mathbf{r}, t) = \mathbf{E}(\mathbf{r})\widetilde{T}(t)$, which is often the case in optics, and always so for time-harmonic fields. Now the wave equation simplifies to vector Helmholtz equation [54]

$$(\nabla^2 + k^2)\mathbf{E} = \mathbf{0}, \tag{3.1}$$

where $k = ||\mathbf{k}|| = \sqrt{k_x^2 + k_y^2 + k_z^2}$ is the wave number and k_i is the corresponding component of the wave vector $\mathbf{k}$ in Cartesian coordinates. The possible imaginary part of k_z is assumed positive. After some trivial algebra we see that plane waves propagating mainly in $\pm z$-direction are solutions for the homogeneous wave equation

$$\mathbf{E}(x, y, z) = \widehat{\mathbf{E}}(k_x, k_y; z)\mathrm{e}^{i(k_x x + k_y y)} = \widehat{\mathbf{E}}(k_x, k_y; 0)\mathrm{e}^{i(k_x x + k_y y \pm k_z z)}, \tag{3.2}$$

where $\widehat{\mathbf{E}}$ is the amplitude vector of the plane wave with transverse components k_x and k_y. Now a general solution for the Helmholtz equation can be formed by superimposing all possible plane wave solutions as

$$\mathbf{E}(x, y, z) = \iint_{-\infty}^{\infty} \widehat{\mathbf{E}}(k_x, k_y; z)\mathrm{e}^{i(k_x x + k_y y)}\,\mathrm{d}k_x\mathrm{d}k_y. \tag{3.3}$$

This equation is known as *plane wave spectrum representation* or ASR and is the basic foundation of Fourier optics. It states that an arbitrary electric field distribution can be described as a superposition of plane waves. In order to understand Eq. (3.3), we first remember that the Helmholtz equation is linear. Second, we note that plane waves propagating in either k_x, k_y or k_z directions are orthogonal[†]. This implies that proper plane wave solutions can be used to span the complete geometric vector space $\mathbb{R}^3$, i.e., can be utilized to describe an arbitrary electric field distribution.

The beauty of Eq. (3.3) arises from the observation that $\widehat{\mathbf{E}}(k_x, k_y; z)$ is a two-dimensional Fourier transform of field $\mathbf{E}(x, y, z)$ in plane $z = constant$ implying that the well-known mathematical tools of Fourier analysis can be utilized in solving optical problems. The Fourier transformed field can then be solved using the definition of the inverse Fourier transform

$$\widehat{\mathbf{E}}(k_x, k_y; z) = \frac{1}{4\pi^2} \iint_{-\infty}^{\infty} \mathbf{E}(x, y, z)\,\mathrm{e}^{-i(k_x x + k_y y)}\,\mathrm{d}x\,\mathrm{d}y. \tag{3.4}$$

Now if the field in plane $z = 0$ is known, accounting for the propagation of the field in z-direction is a simple task of multiplication in the spatial frequency domain.

We next assume a lossless dielectric medium, for which the refractive index n is a

[†]Orthogonality for functions means mathematically that $\int_{-\infty}^{\infty} \phi_i^*(\mathbf{r})\phi_j(\mathbf{r})\mathrm{d}\mathbf{r} = \delta_{ij}$ for any two functions $\phi_i(\mathbf{r})$ and $\phi_j(\mathbf{r})$.

real quantity. Then the wavenumber component k_z becomes either real or imaginary giving rise to two different characteristic solutions to Eq. (3.4)

$$\text{Propagating plane waves:} \quad \mathrm{e}^{-i(k_x x + k_y y)} \mathrm{e}^{\pm i |k_z| z}, \quad k_x^2 + k_y^2 \leq k^2, \tag{3.5}$$

$$\text{Evanescent waves:} \quad \mathrm{e}^{-i(k_x x + k_y y)} \mathrm{e}^{-|k_z||z|}, \quad k_x^2 + k_y^2 > k^2. \tag{3.6}$$

where the latter exponential factor leads to either oscillatory or exponentially decaying behaviour as a function of z.

3.2 Far-field Approximation in Angular Spectrum Representation

In order to utilize ASR in describing tightly focused laser beams, we next show how Fourier optics and ray optics arise from ASR. We start by solving the electric field in a far-field point $\mathbf{r} = \mathbf{r}_\infty$. We define a dimensionless unit vector $\mathbf{s}$ as

$$\mathbf{s} = (s_x, s_y, s_z) = \left(\frac{x}{r}, \frac{y}{r}, \frac{z}{r} \right), \tag{3.7}$$

where $r = \sqrt{x^2 + y^2 + z^2}$ is the distance of $\mathbf{r}_\infty$ from origin. We then assume that the point is sufficently far, so that only the freely propagating plane waves contribute and we can neglect the evanescent waves for which $k_x^2 + k_y^2 \geq k^2$. Now Eq. (3.3) can be approximated using the following limit

$$\mathbf{E}_\infty(s_x, s_y, s_z) = \lim_{kr \to \infty} \iint\limits_{k_x^2 + k_y^2 \leq k^2} \widehat{\mathbf{E}}(k_x, k_y; 0)\, \mathrm{e}^{ikr\left(\frac{k_x}{k} s_x + \frac{k_y}{k} s_y + \frac{k_z}{k} s_z\right)} \,\mathrm{d}k_x \,\mathrm{d}k_y. \tag{3.8}$$

The integal of Eq. (3.8) can be solved e.g. using the stationary phase method[‡]

$$\mathbf{E}_\infty(s_x, s_y, s_z) = -i 2\pi k s_z \widehat{\mathbf{E}}(k s_x, k s_y; 0) \frac{e^{ikr}}{r}, \tag{3.9}$$

where by replacing $k_x \to k s_x$ and $k_y \to k s_y$ the Fourier transform of the field at the object plane ($z = 0$) now defines the far-field $\mathbf{E}_\infty$. Then for the unit vector $\mathbf{s}$ following

[‡]Stationary phase or steepest descent method is often used to solve oscillatory integrals. These kinds of integrals commonly occur in Optics and in quantum field theories. A good introduction to these methods is given in Chapter 1.2 of 'Quantum field theory in a nutshell' by Zee[55].

applies

$$\mathbf{s} = (s_x, s_y, s_z) = \left(\frac{k_x}{k}, \frac{k_y}{k}, \frac{k_z}{k}\right). \tag{3.10}$$

The field at the object plane can then be written as

$$\widehat{\mathbf{E}}(k_x, k_y; 0) = \frac{ire^{-ikr}}{2\pi k_z}\mathbf{E}_\infty(k_x, k_y). \tag{3.11}$$

Now we see that only one plane wave component $\mathbf{k} = (k_x, k_y, k_z)$ of the ASR affects the far-field in point $\mathbf{r}_\infty$ justifying the approximation used in ray or geometrical optics, where light is treated as bundle of rays. Finally, Eq. (3.3) can be simplified using Eq. (3.11) into the form

$$\mathbf{E}(x, y, z) = \frac{ir\mathrm{e}^{-ikr}}{2\pi} \iint\limits_{k_x^2+k_y^2\leq k^2} \mathbf{E}_\infty(k_x, k_y)\, \mathrm{e}^{i(k_x x + k_y y + k_z z)} \frac{1}{k_z}\, \mathrm{d}k_x\, \mathrm{d}k_y. \tag{3.12}$$

Now we see, that in the far-field approximation the field $\mathbf{E}$ and its subsequent far-field $\mathbf{E}_\infty$ are almost Fourier transform pairs at $z = 0$. Only the factor $1/\,k_z$ separates them from being perfect Fourier pairs. Thus we arrive at the limit of Fourier Optics where $k_z \approx k$, and have now tools to go beyond.

3.3 Tight Focusing

Next we derive the equations to describe the electric field in the focal volume due to focusing with high numerical aperture (NA) elements. For simplicity, we assume that the focusing element is aplanatic, i.e., free of spherical aberration. Then we assume the refracted wavefront after the element to be spherical with point F as the center point and focal length f as the radius. Let us now denote an arbitrary point near the focal point F in Cartesian and cylindrical coordinate systems as $\mathbf{r} = (x, y, z) = (\varrho, \varphi, z)$ and a point near the refracting surface by Cartesian and spherical coordinate systems as $\mathbf{r}_\infty = (x_\infty, y_\infty, z_\infty) = (f, \theta, \phi)$ (see Fig. 3.1 for illustration). The unit vectors for the spherical coordinate systems are denoted as $\mathbf{n}_r$, $\mathbf{n}_\phi$ and $\mathbf{n}_\theta$.

Due to symmetry reasons, also the input field before the focusing element is convenient to describe using the cylindrical coordinates (ϱ, ϕ, z) with corresponding unit vectors as $\mathbf{n}_\varrho$, $\mathbf{n}_\phi$ and $\mathbf{n}_z$ (see Fig. 3.1). The relations between the unit vectors $\mathbf{n}_\varrho$, $\mathbf{n}_\phi$ and

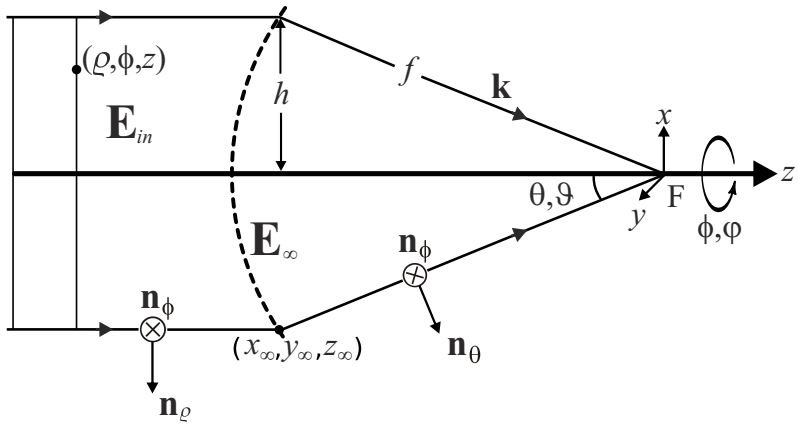

Figure 3.1 Coordinate systems used for describing the focusing of the input field $\mathbf{E}_{in}$. Also the cylindrical coordinate system (ϱ, ϕ, z) used in calculations is shown.

$\mathbf{n}_\theta$ and the unit vectors of the Cartesian coordinate system are then found as

$$\mathbf{n}_\varrho = \cos\phi\ \mathbf{n}_x + \sin\phi\ \mathbf{n}_y \tag{3.13a}$$

$$\mathbf{n}_\phi = -\sin\phi\ \mathbf{n}_x + \cos\phi\ \mathbf{n}_y \tag{3.13b}$$

$$\mathbf{n}_\theta = \cos\theta\cos\phi\ \mathbf{n}_x + \cos\theta\sin\phi\ \mathbf{n}_y - \sin\theta\ \mathbf{n}_z\,. \tag{3.13c}$$

Now the integral in Eq. (3.12) can be simplified by transforming the components of the wave vector $\mathbf{k}$ into the spherical coordinates using relations

$$k_x = k\sin\theta\cos\phi, \tag{3.14a}$$

$$k_y = k\sin\theta\sin\phi, \tag{3.14b}$$

$$k_z = k\cos\theta, \tag{3.14c}$$

and at the same time transforming the differentials of integration as

$$\mathrm{d}k_x\,\mathrm{d}k_y = k^2\cos\theta\ \sin\theta\,\mathrm{d}\theta\,\mathrm{d}\phi\,. \tag{3.15}$$

The integral of Eq. (3.12) can then be written as

$$\mathbf{E}(\varrho,\varphi,z) = \frac{ikf\mathrm{e}^{-ikf}}{2\pi}\int_0^{\theta_{max}}\int_0^{2\pi}\mathbf{E}_\infty(\theta,\phi)\,\mathrm{e}^{ikz\cos\theta}\,\mathrm{e}^{ik\varrho\sin\theta\cos(\phi-\varphi)}\sin\theta\,\mathrm{d}\phi\,\mathrm{d}\theta, \tag{3.16}$$

where $\mathbf{E}(\varrho, \varphi, z)$ represents the field near the focus and the limit of integration $\theta_{\max}$ is related to the NA of the focusing element through

$$\mathrm{NA} = n \sin \theta_{\max} , \qquad \text{where } \theta_{\max} \in [0, \pi/2], \tag{3.17}$$

and n is the refractive index of the medium.

Next, we proceed to solve the exact form of the incoming field $\mathbf{E}_{in}$ and relate that to the far-field $\mathbf{E}_{\infty}$ in Eq. (3.16). First we divide the incoming field into two orthogonal components $\mathbf{E}_{in}^{(s)}$ and $\mathbf{E}_{in}^{(p)}$, where the superscripts s and p correspond to linear polarizations parallel and perpendicular to the local plane of incidence, respectively. This division is performed to facilitate easier description of the refraction at the spherical surface. In cylindrical coordinates the field components can be described by following equations

$$\mathbf{E}_{in}^{(s)} = (\mathbf{E}_{in} \cdot \mathbf{n}_{\phi})\, \mathbf{n}_{\phi}, \tag{3.18a}$$

$$\mathbf{E}_{in}^{(p)} = (\mathbf{E}_{in} \cdot \mathbf{n}_{\varrho})\, \mathbf{n}_{\varrho}, \tag{3.18b}$$

using which the refracted far-field $\mathbf{E}_{\infty}$ can be written in the form

$$\begin{aligned} \mathbf{E}_{\infty}(\theta, \phi) &= \left(t^s \mathbf{E}_{in}^{(s)} + t^p \mathbf{E}'^{(p)}_{in} \right) \sqrt{\cos\theta} \\ &= \left[t^s \left(\mathbf{E}_{in} \cdot \mathbf{n}_{\phi} \right) \mathbf{n}_{\phi} + t^p \left(\mathbf{E}_{in} \cdot \mathbf{n}_{\varrho} \right) \mathbf{n}_{\theta} \right] \sqrt{\cos\theta}, \end{aligned} \tag{3.19}$$

where the unit vectors of the spherical coordinate system have been utilized and t^s t^p are the Fresnel transmission coefficients. The refraction of the far-field at the spherical surface and the corresponding change from cylindrical coordinate system of the collimated beam into the spherical one of the focused beam has important consequences. First, the direction of the p-polarized component changes ($\mathbf{n}_{\varrho} \rightarrow \mathbf{n}_{\theta}$). Secondly, due to the conservation of energy the cosine factors appear.

For simplicity, we next assume that the focusing element is perfectly transparent, so that $t^s = t^p = 1$ applies. Now Eq. (3.19) simplifies to

$$\mathbf{E}_{\infty}(\theta, \phi) = \left[\left(\mathbf{E}_{in} \cdot \mathbf{n}_{\phi} \right) \mathbf{n}_{\phi} + \left(\mathbf{E}_{in} \cdot \mathbf{n}_{\varrho} \right) \mathbf{n}_{\theta} \right] \sqrt{\cos\theta}. \tag{3.20}$$

For the case of x-polarized input beam Eq. (3.20) can be written using simple geo-

metrical arguments as[††]

$$\begin{aligned}
\mathbf{E}^{\mathbf{x}}_{\infty}(\theta,\phi) &= E_{in}(\theta,\phi)\left[(\mathbf{n}_x\cdot\mathbf{n}_\phi)\,\mathbf{n}_\phi+(\mathbf{n}_x\cdot\mathbf{n}_\varrho)\,\mathbf{n}_\theta\right]\sqrt{\cos(\theta)}\\
&= E_{in}(\theta,\phi)\left(-\sin\phi\begin{bmatrix}-\sin\phi\\-\cos\phi\\0\end{bmatrix}+\cos\phi\begin{bmatrix}\cos\phi\cos\theta\\\sin\phi\cos\theta\\-\sin\theta\end{bmatrix}\right)\sqrt{\cos\theta}\\
&= E_{in}(\theta,\phi)\frac{1}{2}\begin{bmatrix}(1+\cos\theta)-(1-\cos\theta)\cos 2\phi\\-(1-\cos\theta)\sin 2\phi\\-2\cos\phi\ \sin\theta\end{bmatrix}\sqrt{\cos\theta},
\end{aligned}\tag{3.21}$$

where $E_{in}(\theta,\phi)$ is the scalar field amplitude.

In this work, we were interested in finding tools to control the 3D electric field distribution at the focal volume. This can be achieved, e.g., by utilizing polarized higher-order laser modes, which we next show. Since the collimated input beam before the focusing element can be well approximated using paraxial approximation, it is a simple task to find the form of the amplitude profile of some higher-order laser mode. We start by solving the form of the first few orders of Hermite-Gaussian (HG) modes[§]. Due to the orthogonality of the HG modes, and linearity of the Helmholtz equation, analogous to ASR, we can use different HG modes to span a mode space of more arbitrary input beams and polarizations.

[††]Remember: $\sin^2\theta=\frac{1}{2}(1-\cos 2\phi)$, $\cos^2\theta=\frac{1}{2}(1+\cos 2\phi)$ and $\sin 2\phi=2\sin\phi\cos\phi$.

[§]Laguerre-Gaussian (LG) modes would be another interesting choice for basis functions. They are cylindrically symmetric and have an elegant mathematical reppresentation for orbital angular momentum in the form of $e^{il\phi}$, $l\in\mathbb{Z}$.

In spherical coordinates the first three HG modes can be written as

$$\begin{aligned} \mathrm{HG}_{00}: \qquad E_{in} &= E_0 \mathrm{e}^{-(x_\infty^2+y_\infty^2)/w_0^2} = E_0 \mathrm{e}^{-f^2\sin^2\theta/w_0^2} \\ &= E_0 f_w(\theta), \end{aligned} \tag{3.22a}$$

$$\begin{aligned} \mathrm{HG}_{10}: \qquad E_{in} &= E_0 (x_\infty/w_0) \mathrm{e}^{-(x_\infty^2+y_\infty^2)/w_0^2} \\ &= E_0 (f/w_0) \sin\theta\cos\phi \; f_w(\theta), \end{aligned} \tag{3.22b}$$

$$\begin{aligned} \mathrm{HG}_{01}: \qquad E_{in} &= E_0 (y_\infty/w_0) \mathrm{e}^{-(x_\infty^2+y_\infty^2)/w_0^2} \\ &= E_0 (f/w_0) \sin\theta\sin\phi \; f_w(\theta), \end{aligned} \tag{3.22c}$$

where w_0 is the beam waist and notation is simplified by noticing that the factor $f_w(\theta) = \exp(-f^2\sin^2\theta/w_0^2)$ appears in all equations. By defining a filling factor f_0 as the ratio of the beam waist to the aperture radius

$$f_0 = \frac{w_0}{f\sin\theta_{\max}}, \tag{3.23}$$

we can write the factor $f_w(\theta)$ in a form

$$f_w(\theta) = \exp\left(-\frac{1}{f_0^2}\frac{\sin^2\theta}{\sin^2\theta_{\max}}\right), \tag{3.24}$$

which is known as the apodization function.

The calculation of Eq. (3.16) can be further simplified by noticing that the integration over ϕ can be performed analytically by utilizing the following equations

$$\int_0^{2\pi} \cos(n\phi)\mathrm{e}^{ix\cos(\phi-\varphi)}\,\mathrm{d}\phi = 2\pi(i^n)J_n(x)\cos(n\varphi), \tag{3.25a}$$

$$\int_0^{2\pi} \sin(n\phi)\mathrm{e}^{ix\cos(\phi-\varphi)}\,\mathrm{d}\phi = 2\pi(i^n)J_n(x)\sin(n\varphi), \tag{3.25b}$$

where the integral form of the definition of the Bessel functions of the first kind J_n is utilized. For future notational convenience, we now adopt short-hand notations for

the following integrals[54]

$$I_{00} = \int_0^{\theta_{\max}} f_w(\theta)\sqrt{\cos\theta}\sin\theta(1+\cos\theta)J_0(k\varrho\sin\theta)\mathrm{e}^{ikz\cos\theta}\,\mathrm{d}\theta, \tag{3.26a}$$

$$I_{01} = \int_0^{\theta_{\max}} f_w(\theta)\sqrt{\cos\theta}\sin^2\theta J_1(k\varrho\sin\theta)\mathrm{e}^{ikz\cos\theta}\,\mathrm{d}\theta, \tag{3.26b}$$

$$I_{02} = \int_0^{\theta_{\max}} f_w(\theta)\sqrt{\cos\theta}\sin\theta(1-\cos\theta)J_2(k\varrho\sin\theta)\mathrm{e}^{ikz\cos\theta}\,\mathrm{d}\theta, \tag{3.26c}$$

$$I_{10} = \int_0^{\theta_{\max}} f_w(\theta)\sqrt{\cos\theta}\sin^3\theta J_0(k\varrho\sin\theta)\mathrm{e}^{ikz\cos\theta}\,\mathrm{d}\theta, \tag{3.26d}$$

$$I_{11} = \int_0^{\theta_{\max}} f_w(\theta)\sqrt{\cos\theta}\sin^2\theta(1+3\cos\theta)J_1(k\varrho\sin\theta)\mathrm{e}^{ikz\cos\theta}\,\mathrm{d}\theta, \tag{3.26e}$$

$$I_{12} = \int_0^{\theta_{\max}} f_w(\theta)\sqrt{\cos\theta}\sin^2\theta(1-\cos\theta)J_1(k\varrho\sin\theta)\mathrm{e}^{ikz\cos\theta}\,\mathrm{d}\theta, \tag{3.26f}$$

$$I_{13} = \int_0^{\theta_{\max}} f_w(\theta)\sqrt{\cos\theta}\sin^3\theta J_2(k\varrho\sin\theta)\mathrm{e}^{ikz\cos\theta}\,\mathrm{d}\theta, \tag{3.26g}$$

$$I_{14} = \int_0^{\theta_{\max}} f_w(\theta)\sqrt{\cos\theta}\sin^2\theta(1-\cos\theta)J_3(k\varrho\sin\theta)\mathrm{e}^{ikz\cos\theta}\,\mathrm{d}\theta. \tag{3.26h}$$

Using these notations[¶] and simple trigonometric arguments, Eq. (3.16) can be written

[¶]It is interesting to note the similarity of the defined integrals to Hankel transformations. The integration is now performed over angle θ instead of the usual variable of radial distance r. One could transform the integrals into proper Hankel transformations by transforming the Fourier transform of Eq. (3.3) into cylindrical coordinates instead of the spherical coordinates we chose. That way one might be able to find some analytical solutions to the given equations, which now need to be calculated numerically.

for our example case of x-polarized HG_{00} beam simply as

$$\mathbf{E}^{\mathbf{x}}_{00}(\mathbf{r}) = \frac{ikf}{2} E_0 \mathrm{e}^{-ikf} \begin{bmatrix} I_{00} + I_{02}\cos 2\phi \\ I_{02}\sin 2\phi \\ -2iI_{01}\cos\phi \end{bmatrix}, \tag{3.27a}$$

$$\mathbf{H}^{\mathbf{x}}_{00}(\mathbf{r}) = \frac{ikf}{2Z_{\mu\epsilon}} E_0 \mathrm{e}^{-ikf} \begin{bmatrix} I_{02}\sin 2\phi \\ I_{00} - I_{02}\cos 2\phi \\ -2iI_{01}\sin\phi \end{bmatrix}, \tag{3.27b}$$

where $Z_{\mu\epsilon} = \sqrt{\mu/\epsilon}$ is the wave impedance. The magnetic field $\mathbf{H}$ is given for completeness, and can be derived by applying a 90° rotation transformation ($\phi \to \phi' + 90°$) to Eq. (3.27a) and multiplying by $Z_{\mu\epsilon}$. We proceed to write similar equations also for x-polarized HG_{01} and HG_{10} beams

$$\mathbf{E}^{\mathbf{x}}_{01}(\mathbf{r}) = \frac{ikf^2}{2w_0} E_0 \mathrm{e}^{-ikf} \begin{bmatrix} i(I_{11} + 2I_{12})\sin\phi + iI_{14}\sin 3\phi \\ -iI_{12}\cos\phi - iI_{14}\cos 3\phi \\ 2I_{13}\sin 2\phi \end{bmatrix}, \tag{3.28a}$$

$$\mathbf{H}^{\mathbf{x}}_{01}(\mathbf{r}) = \frac{ikf^2}{2w_0 Z_{\mu\epsilon}} E_0 \mathrm{e}^{-ikf} \begin{bmatrix} iI_{12}\cos\phi - iI_{14}\cos 3\phi \\ -iI_{11}\sin\phi - iI_{14}\sin 3\phi \\ -2I_{10} - 2I_{13}\cos 2\phi \end{bmatrix}, \tag{3.28b}$$

$$\mathbf{E}^{\mathbf{x}}_{10}(\mathbf{r}) = \frac{ikf^2}{2w_0} E_0 \mathrm{e}^{-ikf} \begin{bmatrix} iI_{11}\cos\phi + iI_{14}\cos 3\phi \\ -iI_{12}\sin\phi + iI_{14}\sin 3\phi \\ -2I_{10} + 2I_{13}\cos 2\phi \end{bmatrix}, \tag{3.28c}$$

$$\mathbf{H}^{\mathbf{x}}_{10}(\mathbf{r}) = \frac{ikf^2}{2w_0 Z_{\mu\epsilon}} E_0 \mathrm{e}^{-ikf} \begin{bmatrix} -iI_{12}\sin\phi + iI_{14}\sin 3\phi \\ i(I_{11} + I_{12})\cos\phi - iI_{14}\cos 3\phi \\ 2I_{13}\sin 2\phi \end{bmatrix}, \tag{3.28d}$$

which we can utilize to form more arbitrary beams and polarizations.

3.4 Vector Point-spread Function Engineering

Now we have the mathematical tools to rigorously describe 3D vector fields at the focal volume of tightly focusing, or high NA, elements. Next, we briefly highlight the possibilities it opens for designing and controlling 3D field distributions by vector point-spread function (VPSF) engineering[56].

We start by considering how a normal Gaussian beam (HG_{00}) behaves when focused tightly. The mathematical description is given by Eqs. (3.27), from which we already see that clearly a distribution of non-zero field component in the propagation z-direction exists (see Fig. 3.2). This contradicts predictions of traditional scalar approaches, where the electric field distributions are assumed to be purely transverse with respect to the propagation direction. In order to somehow quantify the magnitude of this deviation, we calculate the maximum value for the ratio between the transverse ($E_{x,y}$) and longitudinal (E_z) field components. This ratio is for example roughly 3.5 for the previously mentioned focusing conditions, and can be controlled by changing either the NA, filling factor f_0 or the shape of the apodization function $f_w(\theta)$. But, interestingly the actual relative shape of the field distribution does not change, as is known to occur when paraxial approximation holds. Thus the only thing the focusing condition changes is the relative strength of the distribution of the longitudinal field component. To conlude, tight focusing gives us a tool to study how the longitudinal field component can affect light-matter interactions, where traditional scalar approaches assume that the longitudinal field is non-existent.

Next we consider higher-order laser modes, namely HG and LG modes[42,54,57], which are also eigensolutions of the wave equation (and Fourier transform) and thus properly propagating modes*. Essentially by utilizing these higher-order laser modes we get a new degree of freedom to control the apodization function. This new degree of freedom has been been utilized for example in controlled excitation of higher-order particle plasmon resonances in nanostructures[58]. Another very interesting application is optical resolution enhancement, which has been demonstrated for linear as well as

*LG modes are eigensolutions of wave equation in cylindrical coordinates (and thus eigensolutions of Hankel transforms).

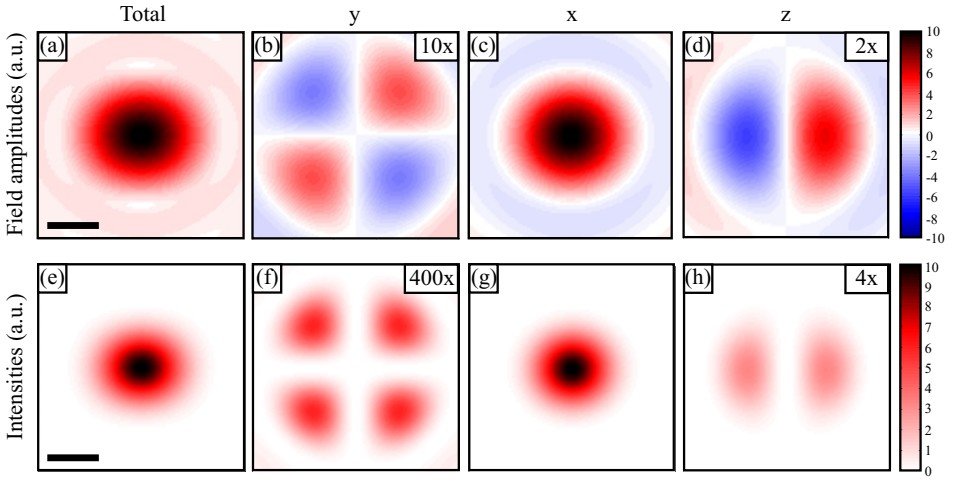

Figure 3.2 Normalized electric field and intensity distributions of linearly polarized (in x-direction) focused HG_{00} beam at the focal plane ($z = 0$). (a) Modulus of total field amplitudes as well as the (b-d) Cartesian components are plotted. (e) Total intensity and (f-h) the individual Cartesian components are also plotted. For better visibility Figures (b),(d),(f) and (h) have been scaled. The scaling factors are indicated in the figures. Focusing conditions of NA=0.8 and f_0=1 were used in the calculations. The scale bars correspond to one wavelength.

nonlinear (THG and CARS) imaging modalities[34,36,37,39,40].

Even more controlled field distributions can be achieved by superimposing various HG and LG modes into cylindrically symmetric vector beams (CVBs), which can also have spatially inhomogeneous polarization distribution[59–61]. The most well-known examples of CVBs are RP and azimuthally polarized (AP) beams[42–46]. Also higher-order RP beams have been realized[62]. The field distributions of RP and AP can be formed by the following superpositions

$$\mathbf{E}^{\mathrm{RP}}(\mathbf{r}) = \mathbf{E}^{\mathbf{x}}_{10}(\mathbf{r}) + \mathbf{E}^{\mathbf{y}}_{01}(\mathbf{r}) = \frac{ikf^2}{2w_0} E_0 \mathrm{e}^{-ikf} \begin{bmatrix} i(I_{11} - I_{12})\cos\phi \\ i(I_{11} - I_{12})\sin\phi \\ -4I_{10} \end{bmatrix}, \tag{3.29a}$$

$$\mathbf{E}^{\mathrm{AP}}(\mathbf{r}) = \mathbf{E}^{\mathbf{x}}_{01}(\mathbf{r}) - \mathbf{E}^{\mathbf{y}}_{10}(\mathbf{r}) = \frac{ikf^2}{2w_0} E_0 \mathrm{e}^{-ikf} \begin{bmatrix} i(I_{11} + 3I_{12})\cos\phi \\ -i(I_{11} + 3I_{12})\sin\phi \\ 0 \end{bmatrix}. \tag{3.29b}$$

From Eq. (3.29b) we now see, that the longitudinal (z-direction) electric field component of AP is identically zero. But for RP the longitudinal field is moderately strong, as is illustrated in Fig. 3.3 which shows the calculated and normalized electric field amplitudes corresponding to focusing conditions of NA=0.8 and f_0=1.

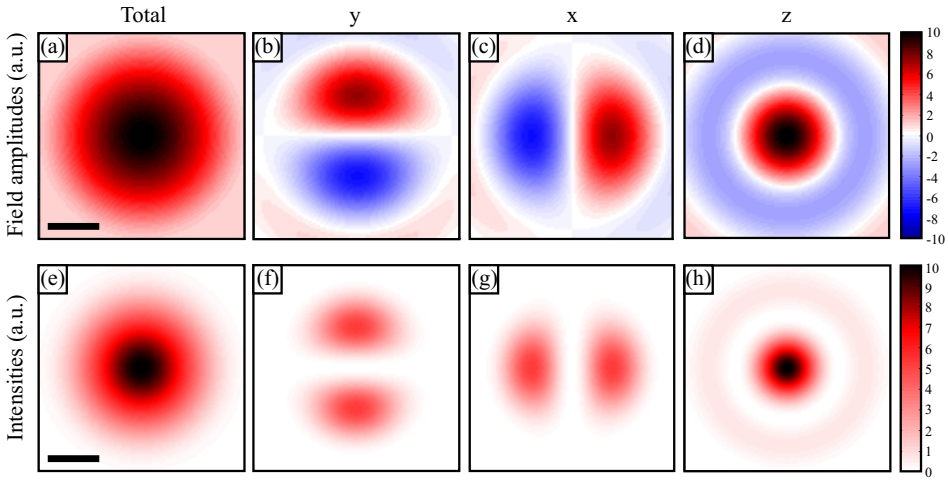

Figure 3.3 Normalized electric field and intensity distributions of a RP focused beam at the focal plane ($z = 0$). (a) Modulus of total field amplitudes as well as the (b-d) Cartesian components (y, x and z, respectively) are plotted. (e) Total intensity and (f-h) the individual Cartesian components are also plotted. Focusing conditions of NA=0.8 and f_0=1 were used in the calculations. The scale bars correspond to one wavelength.

RP has found more applications than AP, and has been utilized for example in particle acceleration[63], in laser welding[64–66], in various microscopy techniques[44,67–71], optical trapping[72,73] and in 3D molecular orientation studies[46,74–76]. CVBs have also been utilized to achieve 3D polarization control at the focal volumes of high NA objectives[77–79]. Recently, similar to previous work with HG beams[58], CVBs have also been proposed for controlled excitation of higher-order particle plasmon modes[80]. The main reason why RP has been found useful, is that focused RP beam has a strong field component in z-direction (Fig. 3.3)[46,81–85]. Very recently, the predicted phase difference between the transverse and the longitudinal field components has also been experimentally verified using a phase-sensitive detection scheme at THz frequencies[86].

There are several techniques to realize VSPF engineering and CVBs in practise. CVBs have been generated using for example fibers,[87,88] interferometric approaches[43,89],

laser intra-cavity axicons[90], metal gratings[91,92], segmented phase- or wave plates[93,94], or liquid-crystals[95,96]. A particularly elegant way utilizes spatial light modulators (SLMs), which give even more flexibility to generate different mode and polarization distributions[56,57]. So far, two techniques (segmented wave plates and liquid crystal devices) have been commercialized, due to which CVBs have also become more available to researchers.

Chapter 4

Second-harmonic Generation Microscopy

In this Chapter, we finally combine the concepts of the previous Chapters 2 and 3 to describe SHG using focused vector beams. Then we apply the formalism to polarized SHG microscopy. The propagation of SHG light is treated using Green's function approach and relies heavily on the book by Novotny and Hecht[54]. We note that although the following treatment is given only for SHG, it would be straightforward to generalize the treatment to other nonlinear processes.

4.1 Second-harmonic Generation Using Focused Beams

In Chapter 2, we described the nonlinear phenomenon of SHG. In the following, the driving field of the second-order polarization is the focused field at the fundamental wavelength. The radiated field due to the polarization is described using Green's function approach, where for simplicity only free-space functions are considered[97–99].

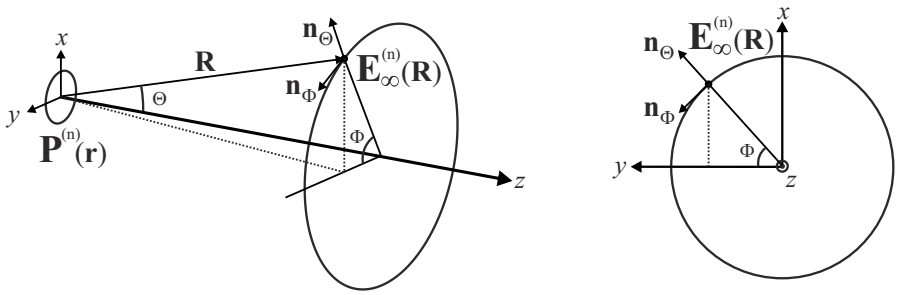

Figure 4.1 Focused beam at the fundamental frequency ω creates nonlinear polarization in the vicinity of the focal plane, which further radiates into point $\mathbf{R}$. Spherical coordinates (R,Θ,Φ) with their corresponding unit vectors are also defined in the picture.

We start by assuming that the indices of refraction for all the media of interest are unity. The field oscillating at the fundamental frequency ω creates a nonlinear polarization $\mathbf{P}$ at point $\mathbf{r}$ (see more detailed description from Chapter 2) at the second-harmonic frequency 2ω as[41]

$$P_i^{(2)}(\mathbf{r},2\omega) = \epsilon_0 \sum_{jk} \chi_{ijk}^{(2)}(\mathbf{r}) E_j(\mathbf{r},\omega) E_k(\mathbf{r},\omega), \tag{4.1}$$

where the susceptibility $\chi_{ijk}^{(2)}$ as well as the focused field $\mathbf{E}$ are assumed inhomogeneous and $(i,j,k) \in \{x,y,z\}$. The local polarization $\mathbf{P}^{(2)}(2\omega)$ then acts as a driving term in the inhomogeneous wave equation [see Eq. (2.3)] and creates radiation at the 2ω frequency. The wave equation and thus the radiated SHG far-field in point $\mathbf{R} = (X,Y,Z) = (R,\Theta,\Phi)$ due to the local confined source distribution can be expressed in the form[54,98]

$$\mathbf{E}_\infty(\mathbf{R},2\omega) = -\frac{8\pi\omega^2}{c^2} \iiint_V \bar{G}(\mathbf{R},\mathbf{r}) \mathbf{P}^{(2)}(\mathbf{r},2\omega)\, \mathrm{d}V, \tag{4.2}$$

where $\bar{G}(\mathbf{R},\mathbf{r})$ is the dyadic Green's function. Although in this work we are mainly interested in thin films and surfaces, for generality, the integration is performed over volume V. By neglecting reflections, only the free-space Green's function needs to be considered, which can be written as

$$\bar{G}(\mathbf{R},\mathbf{r}) = \left(\bar{I} + \frac{\nabla \otimes \nabla}{k_2^2}\right) G(\mathbf{R},\mathbf{r}), \tag{4.3}$$

where k_2 is the wavenumber of the SHG field and $\bar{I}$ is the dyadic identity tensor of

second rank. The dyadic operator $\nabla \otimes \nabla$[‡] acts on the scalar Green's function $G(\mathbf{R}-\mathbf{r})$ of the form

$$G(\mathbf{R},\mathbf{r}) = \frac{\exp(ik_2\,|\mathbf{R}-\mathbf{r}|)}{4\pi\,|\mathbf{R}-\mathbf{r}|}. \tag{4.4}$$

Then by assuming that the point of interest ($\mathbf{R}$) is far from the radiating source, the relation $|\mathbf{R}| = R \gg |\mathbf{r}|$ applies, and the norm $|\mathbf{R}-\mathbf{r}|$ can be approximated by $R - \mathbf{r}\cdot\mathbf{R}/R$. The scalar Green's function then becomes

$$G(\mathbf{R},\mathbf{r}) = \frac{\exp(ik_2R)}{4\pi R}\exp\left(\frac{-ik_2\mathbf{r}\cdot\mathbf{R}}{R}\right), \tag{4.5}$$

which can be used to approximate Eq. (4.3) as

$$\begin{aligned}\bar{G}(\mathbf{R},\mathbf{r}) \approx G(\mathbf{R},\mathbf{r})\mathbf{G}(\mathbf{R}) = \frac{\exp(ik_2R)}{4\pi R}\exp\left(-\frac{ik_2\mathbf{r}\cdot\mathbf{R}}{R}\right) \\ \times\begin{bmatrix}(1-X^2/R^2) & -XY/R^2 & -XZ/R^2\\ -XY/R^2 & (1-Y^2/R^2) & -YZ/R^2\\ -XZ/R^2 & -YZ/R^2 & (1-Z^2/R^2)\end{bmatrix}.\end{aligned} \tag{4.6}$$

Due to the spherical symmetry of the radiation problem, it is convenient to transform the matrix part $\mathbf{G}(\mathbf{R})$ of Eq. (4.6) using spherical coordinates[§]:

$$\mathbf{G}(\mathbf{R}) = \begin{bmatrix}1-\cos^2\Phi\sin^2\Theta & -\sin\Phi\cos\Phi\sin^2\Theta & -\cos\Phi\sin\Theta\cos\Theta\\ -\sin\Phi\cos\Phi\sin^2\Theta & 1-\sin^2\Phi\sin^2\Theta & -\sin\Phi\sin\Theta\cos\Theta\\ -\cos\Phi\sin\Theta\cos\Theta & -\sin\Phi\sin\Theta\cos\Theta & \sin^2\Theta\end{bmatrix}, \tag{4.7}$$

using which the SHG field of Eq. (4.2) can be calculated.

Next we assume that the radiated SHG field is collimated by a perfectly transparent and antireflective element. By modifying Eq. (3.20) we can now write the collimated field as

$$\mathbf{E}_{out}(2\omega) = [(\mathbf{E}_\infty(2\omega)\cdot\mathbf{n}_\phi)\mathbf{n}_\phi + (\mathbf{E}_\infty(2\omega)\cdot\mathbf{n}_\theta)\mathbf{n}_\varrho]\,\frac{1}{\sqrt{\cos\Theta}}. \tag{4.8}$$

Since the radiated electric far-field $\mathbf{E}_\infty(2\omega)$ is transverse, we can simplify the calcula-

[‡] dyadic product: $\mathbf{c} = \mathbf{a}\otimes\mathbf{b}, c_{ij} = a_ib_j$.
[§] $X = R\sin\Theta\cos\Phi, \quad Y = R\sin\Theta\sin\Phi \quad$ and $\quad Z = R\cos\Theta.$

tion of Eq. (4.8) by transforming $\mathbf{E}_\infty(2\omega)$ from the Cartesian basis into the spherical one using the following transformation matrix

$$\mathbb{M} = \begin{pmatrix} 0 & 0 & 0 \\ \cos\Theta\cos\Phi & \cos\Theta\sin\Phi & -\sin\Theta \\ -\sin\Phi & \cos\Phi & 0 \end{pmatrix}. \tag{4.9}$$

The first row is now identically zero due to the transverse nature of the radiated field. Combining these results with those of Chapter 3 for the tightly focused incident field allows the collimated SHG signal field to be calculated, providing the theoretical basis for this work.

4.2 Modelling Work

In the past, several modelling schemes for solving the nonlinear scattering problem have been formulated. Such approaches include nonlinear Mie scattering[100–102], finite-difference time-domain (FDTD) method[103–105], Fourier modal method[106,107], finite element method[108], volume integral method[109,110] and boundary element method (BEM)[111]. Despite the range of developed modelling tools, no single technique surpasses the others, and the most suitable technique depends on the nature of the problem in question.

Not counting the BEM modelling work in **Paper 4**, all calculational results in this Thesis are essentially based on the previously introduced formalism, which is a commonly utilized approach in nonlinear microscopy[98,99,112,113]. The crucial assumption is that we treat the nonlinear medium as weakly scattering at the fundamental wavelength, which is reasonable assumption for samples of biological origin. The interaction between various polarizable points can then be assumed to be negligible, after which the local field equals the incident field. Although the approach is only approximate, it provides a good starting point for understanding and predicting nonlinear optical signals in microscopy. Also, a more thorough discrete-dipole approximation (DDA) implementation has been recently formulated, which takes into account the interparticle interactions and would thus be more suitable method for modelling nonlinear responses inside strongly scattering media[114,115]. Another interesting approach has

been to combine the simplified DDA approach with Monte Carlo simulations, facilitating modelling of nonlinear signals from turbid (i.e., highly scattering) media [116,117].

The main advantage of our simplistic approach is its simple and flexible implementation. Unlike in some approaches (such as in FDTD), the implementation of excitation using a focused vector field is straightforward. In other words, the approach is well suited for microscopy. Also, modelling of nonlinear signals as a function of the input parameters, such as polarization and apodization function, is straightforward and, more importantly, computationally efficient. Currently, most of the calculations are performed using normal tabletop computers, and the computation times for a single measurement point take only a few seconds facilitating even modelling of entire images recorded by scanning.

But although the formalism introduced in this Thesis might be suitable for treating the nonlinearities of biological and molecular media, one must be cautious in applying it to metal nanoparticle systems, where the optical responses can be strongly modified by the presence of effects such as particle plasmon resonances, local-field effects or nonlocality of the responses. In addition, the nonlinear optical responses of nanoparticles are not yet very well understood and are an interesting research topic in itself. For those systems, for example BEM formalism is more appropriate, since it can take into account several of the mentioned complicating factors [111]. Nevertheless, often a qualitative understanding of the responses of nanoparticles can already be formed by properly considering the vectorial nature of excitation and the symmetry of the nanoparticle system, as was done in the study reported in **Paper 3**. These considerations were later combined with the more accurate modelling based on BEM approach, to provide a more rigorous approach to understand and study nanoparticle systems. This appoach was introduced in **Paper 4** and further work is currently on the way.

4.3 Experimental Arrangements

Next, we briefly explain the practical details of the experimental setup and the samples used in this work. In a nutshell, the setup in all the experiments was a stage-scanning confocal microscope. Both biological and fabricated samples were measured in order to demonstrate the predicted nonlinear effects.

Stage-scanning Confocal Microscope

For the experiments, a custom-built stage-scanning microscope was constructed and is schematically shown in Fig. 4.2. A mode-locked Nd:glass laser (Time-Bandwidth Products) was used as a source of fundamental light. The center wavelength was 1060 nm and pulse width ~200 fs. The repetition rate of the laser was 82 MHz and maximum average output power 300 mW. A beam expander assembly in conjuction with a pinhole (PH, L1, L2) was used to spatially filter and expand the laser beam. The beam was then positioned and aligned for the focusing objective by using three mirrors. In order to maximize the polarization purity of the excitation beam, the optics to control the polarization was implemented after the steering optics. The resulting polarized and collimated beam was finally directed to the back-aperture of an infinity-corrected microscope objective (O1; Nikon LU PLAN Fluor 50 × NA = 0.80), which focused the beam onto the sample. The objective was chosen to be strain-free in order to maintain the desired polarization. The resulting focal spot had a waist diameter of ~800 nm. Also a white light imaging arm was implemented to provide wide-field images of the samples and to ease sample positioning. For the molecular thin film samples the average laser powers were kept below 20 mW to avoid sample damage. For metal nanostructure samples, considerably lower average powers of 1-5 mW were used.

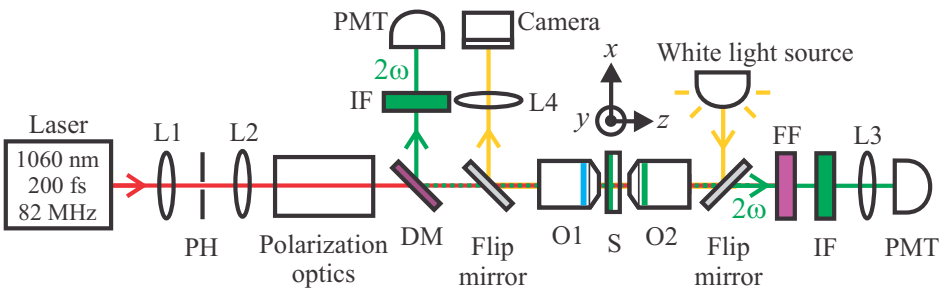

Figure 4.2 Schematic of the SHG microscope used in this work. The optical setup consisted of lenses (L1,L2,L3,L4), pinhole (PH), microscope objectives (O1,O2), 3-axis motorized piezo stage (S), dichroic mirror (DM), flip mirrors, fundamental wavelength-blocking filter (FF), interference filters (IFs), photomultiplier tubes (PMTs) and a wide-field white light imaging arm (yellow ray).

The transmitted/reflected SHG signals were collected by either the focusing objective (O1) or a second objective (O2), which was identical to the first one if not otherwise mentioned.

In the very beginning of the work (**Paper 2**) the focusing and collimation of the beams was achieved by using aspheric lenses (NA = 0.65), and we did not have the capability to scan the sample. Only later, proper focusing elements and stage scanning was implemented to perform imaging (**Papers 3-5**). In **Paper 3**, an objective (Olympus PLAN N 20 × NA = 0.40) was used to collect the transmitted SHG.

Polarization Control

Circular polarizations (CPs) are commonly utilized in techniques to study chiral materials. In such techniques, polarization purity is very important, since even small polarization impurities can drastically decrease the accuracy and sensitivity of the techniques. Considerable effort was thus done to achieve pure CP. This was achieved by first cleaning up the linear polarization of the fundamental beam with a calcite polarizer (P) and then passing the beam through a high quality true zero-order quarter-wave plate (QWP). The orientation of the QWP was controlled by a motorized rotation stage.

RP and AP beams were generated by using a liquid-crystal device (ArcOptix). In order to keep the polarization and the mode quality as good as possible, we first formed an AP beam with the liquid-crystal device. This beam was further purified by using a spatial filter, acting also as a beam expander in order to properly fill the back aperture of the focusing objective. RP was formed by passing the good quality AP beam through two half-wave plates, whose relative orientation was adjusted to 45°. This way the intensity profile of the RP and AP beams could be kept more uniform than using simply the liquid crystal device for polarization control.

4.4 Chiral Imaging

Chiral materials interact differently with CP light giving rise optical activity (OA) effects[53]. The differences in the real part of the susceptibility give rise to optical rotatory dispersion (ORD), and the differences in the imaginary part give rise to circular dichroism (CD). Linear OA effects are nonlocal effects since they require magnetic contributions to the light-matter interaction, and are thus relatively weak effects. This

limits the sensitivity of the linear chiroptical techniques, due to which several approaches have recently been proposed based on the concept of increasing the chirality of the optical field[118–120]. Even further enhancement of the chiral light-matter interaction has been proposed by utilizing plasmonic structures and their related near-field distributions[121–123].

Another approach to increase the sensitivity of the chiroptical techniques is to utilize nonlinear OA effects, which approach was also pursued in this Thesis. In the past, several such chiroptical techniques have been developed based on nonlinear phenomena analogous to linear ORD and CD, such as second-harmonic generation circular dichroism (SHG-CD) or second-harmonic generation linear difference (SHG-LD)[124–131]. The techniques have traditionally been based on surface SHG measurement geometry, where the fundamental beam at an oblique angle of incidence is used. When light is treated using paraxial approximation, the oblique angles of incidence are needed in order to couple light into the surface nonlinearity, since often the tensor components of the nonlinear susceptibility depend on the surface normal [see for example Eq. (2.27)].

But the situation gets complicated if the sample has also in-plane anisotropy. The whole experimental setup can then become chiral, depending on the mutual orientations of the surface normal, the in-plane anisotropy axis and the direction of the incident beam[132]. The problem can be overcome by increasing the overall symmetry of the experimental setup, but leads to complicated measurements where the azimuthal orientation of the sample is varied[133,134].

To overcome the limitations of the traditional techniques, in **Paper 1** we proposed three SHG techniques based on tightly focused laser beams. A nonparaxial treatment was formulated, which predicted coupling of light into the surface nonlinearities even at normal angles of incidence. This ensured that high overall symmetry for the setup could be maintained making the techniques insensitive to the possible in-plane anisotropy. The handedness of the input beams was obtained either by using CP beams or handed superpositions RP and AP beams. Although more complicated to realize experimentally, the handed superpositions of RP and AP beams were predicted to have an almost 10-fold more efficient overall SHG compared to the CP beams and could thus be used to increase the signal-to-noise ratios of experiments.[‡] Differences

[‡]In addition, RP and AP beams and their superpositions possess full rotational symmetry with respect to the propagation axis. For handed CP beams, only the amplitude (and not the phase) distribution has full rotational symmetry.

in SHG responses for chiral samples were then expected when the handedness of the input beam was changed. The normalized change in SHG powers was quantified as [128]

$$\mathrm{SHG-PD} = \frac{\Delta P_{\mathrm{SHG-PD}}}{P_{\mathrm{ave}}} = \frac{P_+ - P_-}{(P_+ + P_-)/2}\,, \tag{4.10}$$

where P corresponded to the measured SHG signal and $(\pm)$ represented the fundamental beams with different handedness.

This was an important result, since the artifacts due to the sample anisotropy are a common hindrance in linear as well as in nonlinear CD spectroscopies [132,135]. In addition to spectroscopic applications, the proposed technique could also facilitate nonlinear chiral or CD imaging, a new tool to study chirality in microscopic scale. Potential applications for the chiroptical imaging tool are numerous, since linear and nonlinear CD measurements are commonly utilized to study for example protein folding and dynamics [136–138]. To the best of the author's knowledge, the very first demonstration of performing SHG-CD *microscopy* on a biologically relevant system was very recently presented by Chen et al. [139]. Also other similar nonlinear chiral imaging modalities have lately been demonstrated, utilizing nonlinear processes of SFG and TPL [140–144]. In addition to traditional normal incidence microscopy setups, also oblique angle of incidence arrangements were earlier demonstrated to possess imaging capabilities, but were unfortunately limited in applicability only to isotropic surfaces [129,141,145].

Unambiguous Probes of Surface Chirality

We performed our first SHG-CD experiments on two molecular samples, which were fabricated in the department of Chemistry and Bioengineering of our university (**Paper 2**). The samples were Langmuir-Blodgett (LB) thin films, consisting of 16 molecular layers deposited on glass. The first LB-film sample consisted of 2-docosylamino-5-nitropyridine (DCANP) molecules, which were synthesized according to literature procedures [146–148]. The DCANP films are known to form anisotropic and achiral molecular layers acting thus as an achiral reference sample. The second sample consisted of chiral tetradodecyloxy-helicenebisquinone (THBQ) molecules, which form anisotropic and chiral thin films [134,149,150].

SHG responses as a function of the rotating QWP were measured from both samples

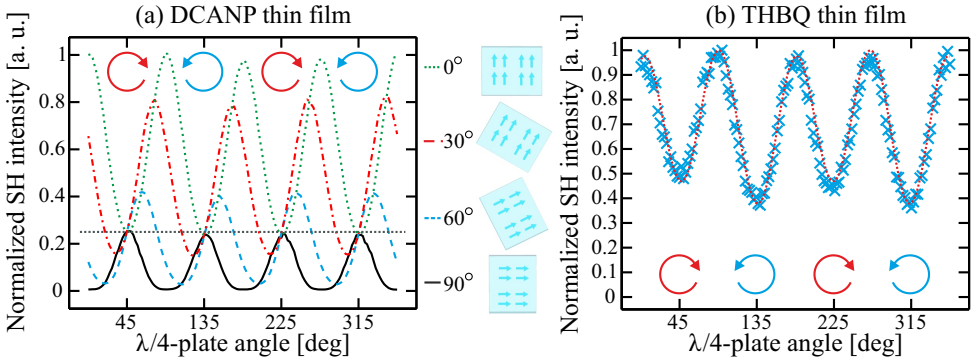

Figure 4.3 SHG responses from (a) DCANP and (b) THBQ thin films were measured as a function of the rotation angle of the QWP. The angles 45° (225°), and 135° (315°) correspond to oppositely handed CP input beam. The calculated SHG-CD responses from the achiral DCANP reference sample were practically zero, irrespectively of the relative sample orientation (0°, 30°, 60° and 90°). But chiral THBQ sample exhibited non-zero SHG-CD responses, confirming the theoretical prediction that the non-zero SHG-CD responses indicate chirality.

and some example measurements are shown in Fig. 4.3. In order to verify the unambiguity of the technique for separating the contributions due to possible in-plane anisotropy from the contributions due to chirality of the sample, we repeated the measurements for various relative orientations for the samples. The relative orientation of the samples did not affect the SHG-CD responses, which for the achiral DCANP sample were measured to be less than 0.03 [shown in Fig. 4.3(a)]. The maximum measurement error for the SHG-CD responses was estimated to be less than 0.05 for the achieved SHG count levels of at least 2000 counts/s. On the other hand, the measured SHG-CD responses of the chiral THBQ thin film were above 0.24 for all the orientations, demonstrating the capability of the technique.

Chiral Imaging of Twisted-cross Nanodimers

The third step was to apply the developed technique to study chiral responses of invidual nano-objects. Altough the nonlinear optical responses of such systems are not yet very well understood, we were interested to study if a qualitative understanding of the effective responses could be formed based on properly considering the overall symmetry of the nano-objects and the vector nature of excitation. For this, a sample consisting of chiral metal nanodimers was utilized, which were known to give rise to

strong linear OA effects[151]. In **Paper 3** we performed chiral imaging of these twisted-cross nanodimers, scanning electron microscopy (SEM) images of which are shown in Fig. 4.4.

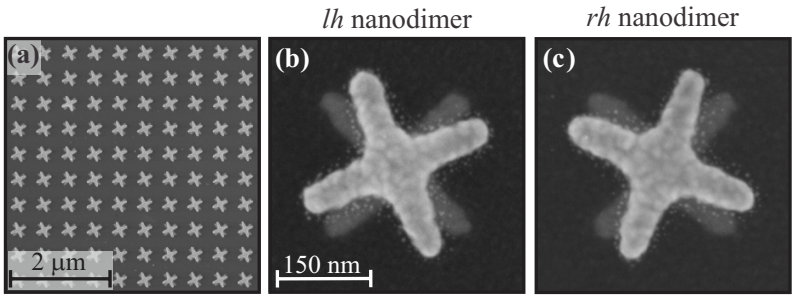

Figure 4.4 SEM images of the (a) fabricated nanodimer array and individual (b) left-handed and (c) right-handed enantiomers. From the close-ups one can see the twisted-cross nanodimers consisting of two achiral crosses on top of each other.

As previously demonstrated, nonlinear microscopy techniques can be very sensitive towards small-scale defects and features of the fabricated nanostructures[152–154]. We achieved similar results by measuring strong variation of total measured SHG signals from individual nanodimers as is shown in Fig. 4.5. The SHG images were then further analyzed by calculating the normalized SHG-CD responses for each pixel. The results are shown in Fig. 4.5(i)-(l), and present more uniform images than the SHG scans. This result suggested, that the overall chiral responses of the nanostructures were not compromized by the defects introduced into the structures during the fabrication. The result also showed the feasibility of using polarized SHG microscopy and especially SHG-CD microscopy to study the optical properties of individual nano-objects.

Finally we note that since the total measured SHG signals were now considerably smaller than for the previous study (~50-300 counts/pixel compared to the minimum of 2000 counts/pixel in **Paper 2**), the measurement error for the SHG-CD responses was consequently larger. This can be seen in the calculated standard deviations for the SHG-CD responses shown in Fig. 4.5(k) and 4.5(l). Although the achieved measurement precision was adequate for the reported study, the accuracy and precision of the SHG-CD measuresments could naturally be increased, if needed, for example by increasing the averaging and the pixel dwell times.

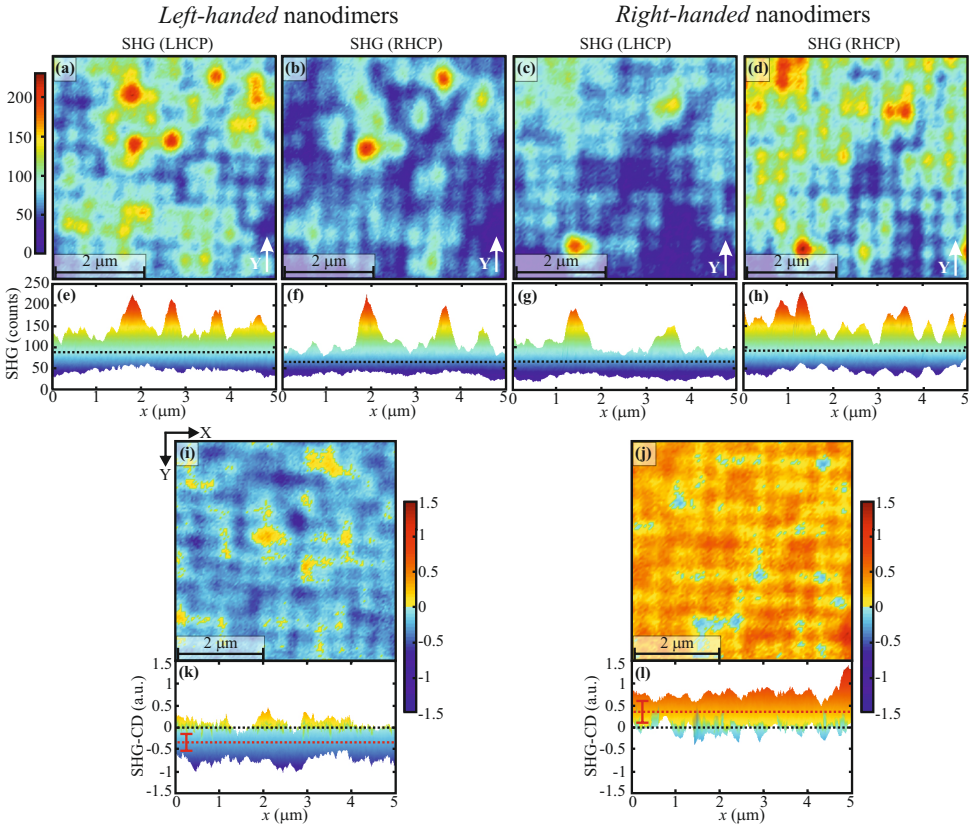

Figure 4.5 SHG microscopy images (a-d) of arrays of twisted-cross nanodimers. Both left- and right-handed enantiomers were measured using either LHCP [(a) and (c)] and RHCP [(b) and (d)] input beams. The line profiles (e-h) illustrate the signal variation. SHG-CD images of (i) left-handed and (j) right-handed enantiomers were calculated. The average SHG-CD values (red dotted lines) from arrays left-handed and right-handed nanodimers were calculated to be -0.32 and 0.35, respectively. Stacked composite line profiles are also shown [(k) and (l)], which illustrate the homogeneity of the measured SHG-CD responses. Calculated standard deviation bars, average signal levels (black dotted lines) and the standard deviation error bars are also shown.

4.5 Vector Beams in Imaging

Although various vector diffraction theories have been formulated several decades ago[155–157], implementation of those treatments to nonlinear optical phenomena has been sparse[98,99,158,159]. Although light is in some applications, such as in confocal mi-

croscopy, strongly focused it is still usually treated as a scalar field*. In the latter part of this work, we studied how vector beams and VPSF engineering could be utilized in SHG microscopy.

Cylindrical Vector Beams

Our laboratory is interested in studying optical properties of metal nanostructures. But optical characterization of individual nano-objects is not trivial, due to their nanoscale dimensions. Additional difficulties arise if one wants to study the tensorial responses of 3D structures with an optical microscope, since one must resort to VPSF engineering.

Nanocones are intriguing 3D nanostructures[84,160–162], which can be used for enhancing optical interactions at the nanoscale due to high local-field enhancements near their tips[28,54,97,163]. The high field enhancements are due to both the lightning-rod effect and the occurrence of plasmon resonances[54,164]. The lightning-rod effect arises from the fact that the electric charges accumulate at the geometrically sharp and pointed features of metal objects. The field enhancement at the nanoscale is relevant for example in sensing, lab-on-chip, photovoltaics and near-field microscopy applications[28,54,165–167].

Although nanocones show promise as near-field probes, several obstacles still remain. First, the coupling of far-field radiation into the localized near-field requires an oscillating field component along the cone[161]. Second, in most applications, the field enhancements near the tips for different individual cones should be as uniform as possible. This is important for example in developing tip-enhanced Raman scattering (TERS) spectroscopy into a commercially feasible technique, where tip degradation and inhomogeneity are the limiting problems. But recent advances show promise that in the near future near-field probes could be truly commercialized[168].

In **Paper 4** we demonstrated how CVBs could be utilized to study optical responses of individual 3D nanostructures. For the study, arrays of gold nanobump and nanocone samples were fabricated using nano-imprint lithography[161,169]. First the samples

*By this the author means that the full vector nature of light is neglected, and paraxial approximation is used to simplify the mathematics. A good example of this is the far-field Green's function, which in general is a tensor [see Eq. (4.6)], but which is often approximated as a scalar.

were characterized by SEM and atomic force microscopy (AFM) [Fig. 4.6(a)]. After this, polarized SHG microscopy using RP and AP input beams was performed [Fig. 4.6(b),(c)]. The SHG, SEM and AFM data were correlated between each other to study how the optical responses of individual objects depended on small-scale sample deformations. From the SEM images we identified deformed nanocones [e.g. bent cones C1 and C6 in Fig. 4.6(a),(d),(e)], which had considerably larger SHG responses than ideal cones [Fig. 4.6(b),(c)]. In addition, the polarization dependence of the deformed cones deviated from the ideal cones, which was readily visible in the SHG images using RP input beam.

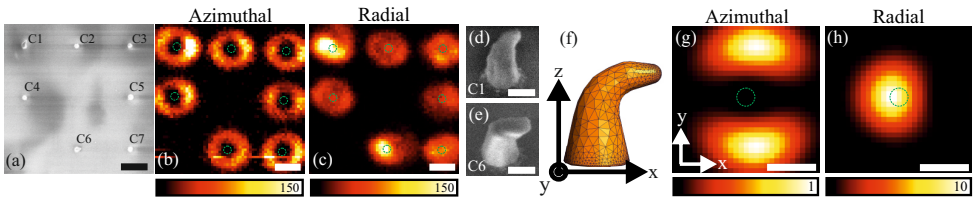

Figure 4.6 Nanocone arrays were imaged by (a) SEM and (b),(c) SHG microscopy. Both (b) AP and (c) RP were used in the SHG experiments to study the coupling of light into the nanocones. Measured SHG signals from bent nanocones (d),(e) were considerably larger than from ideal cones. This effect was further studied by calculating corresponding SHG images of (f) bent structures using (g) AP and (h) RP focused input beam excitation. Scale bars correspond to (a)-(c) 1 μm, (d),(e) 150 nm and (g),(h) 500 nm.

To study the effects of the defects to the nonlinear optical responses of 3D nanostructures in more detail, we modelled the SHG responses of defective nanobumps and nanocones using recently developed BEM approach for solving nonlinear scattering problems[111]. The calculations showed that asymmetry in the scanned images obtained by using CVBs could be related to bent nanocones [4.6(f)-(h)], agreeing well with the experimental results. In overall, the results demonstrated that combining the high sensitivity of SHG microscopy with CVBs, we could only in two scans provide accurate information of the nature of the defects occurring in the 3D nanostructures. The result also demonstrated that modelling of nonlinear responses of more realistic, defective 3D nanostructures and input field distributions is not only possible, but also feasible.

Vector Gaussian beams

In the last part of this work, we studied how the full consideration of vector Gaussian beams could lead to strong deviations in nonlinear light-matter interactions compared to approaches based on scalar diffraction. As is always the case, a spatially finite propagating coherent light distribution is never purely transverse[†]. Thus for example the electric field distribution of a vector Gaussian beam consists of both transverse and longitudinal field components. Term 'longitudinal' now refers to the overall direction where the beam is propagating. Interestingly, the transverse and longitudinal field distributions of Gaussian beams also behave differently under symmetry transformations, and could thus lead to interference effects in coherent optical phenomena, unaccountable by scalar treatments of light[§].

In order to demonstrate the existence of the proposed interference effects, we measured asymmetric SHG emission in forward and backward directions from thin samples, where symmetric emission is predicted using traditional treatments[41]. Two isotropic surface samples were used. The first sample was a LB thin film consisting of a single molecular layer of bacteriorhodopsin molecules. The second sample was a silicon nitride (SiN) film with a thickness of 50 nm. The results for the SiN film are presented in **Paper 5**, where a Gaussian beam (HG_{00}) was used to highlight the general occurrence of the interference effects. The results are shown in Fig. 4.7(a),(b), where additional proof of the interference effects can be seen from the different polarization dependences of the measured SHG signals, which agreed well with the calculations.

In order to understand the situation better, we calculated the nonlinear source distribution in the thin sample limit. Since any vector field can be written as a sum of irrotational and solenoidal terms, we could write the source polarization as[170]

$$\mathbf{P} = \mathbf{P}_i + \mathbf{P}_s = \mathbf{P}_i + \nabla \times \mathbf{P}_p \,, \tag{4.11}$$

where $\mathbf{P}_i$ and $\mathbf{P}_s$ are the irrotational and solenoidal terms, respectively. The latter form emphasizes the fact that the solenoidal term $\mathbf{P}_s$ is divergence-free. The calculations showed, that the even (transverse) and odd (longitudinal) parts of the field

[†]In ASR of a finite spatial profile of some laser beam, some of the plane wave components are propagating in slightly different directions than the overall beam giving rise to longitudinal field.

[§]In fact the author did not come up with any mode where this symmetry breaking would *not* happen! This seems to imply that the phenomenon might be quite general.

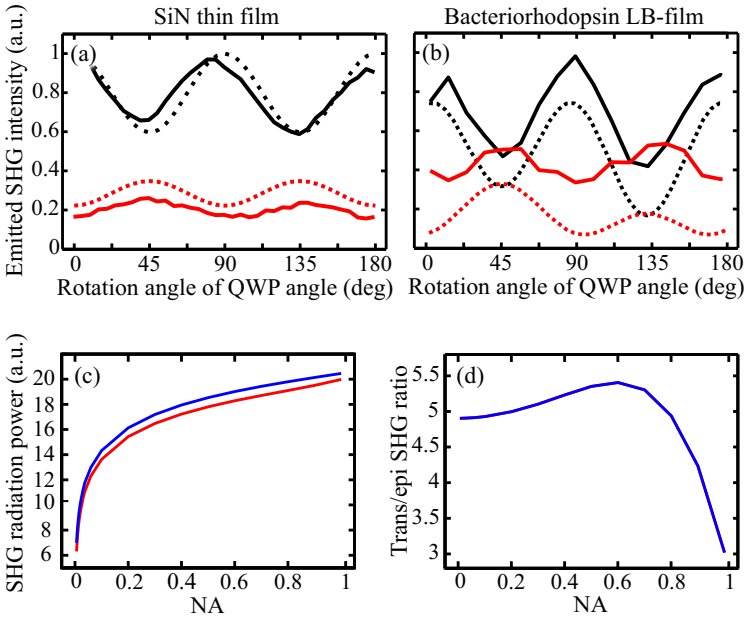

Figure 4.7 Measured and normalized SHG responses from (a) SiN thin film and (b) bacteriorhodopsin LB film as a function of rotating QWP. Solid and dotted lines represent the measured and calculated SHG responses, respectively. Black (red) lines represent transmitted (reflected) responses. Scalar theory predicts the transmitted and reflected signals to behave identically, which clearly is not the case in the measurements. Interestingly, although the (c) overall radiated SHG power decreases as the NA of the focusing element decreases, the (d) calculated transmission ratio do not tend to unity. In other words, similar behaviour is predicted also with weaker focusing conditions.

distribution of focused HG_{00} lead to nonlinear source polarization where the solenoidal term is non-vanishing. This solenoidal term has different radiating properties than the irrotational term. The next step was to express the radiating SH field as a sum of various Mie electric and magnetic terms[170]. The results showed that for the thin samples in general a non-zero solenoidal source polarization is required to obtain a magnetic response, and such response is intrinsically present if vector Gaussian beams instead of scalar ones are considered.

Finally, we make a remark on the range of applicability where the introduced and similar effects could play a considerable role. Although we demonstrated the effect in tight focusing regime (NA=0.8), theoretically the same effect arises also in weaker focusing regime. This fact is illustrated in Fig. 4.7(c),(d) where calculated radiated SHG power and the asymmetric SHG emission ratios are shown for isotropic surface

sample at normal incidence with respect to the input beam. Although the overall SHG radiation power tends to zero while decreasing the strength of the focusing, the SHG emission ratio does not converge to unity. The relative strength of the effect thus remains. In addition, analogous behaviour has been proposed to occur in light-matter interactions inside silicon nanowire waveguides [171–173], where light is confined to spatial dimensions comparable to wavelength[§]. For future nanoscale applications and devices these effects could thus prove to be non-negligible and in principle also be utilized.

[§] In ASR a confined field distribution leads to a broad distribution of plane waves. Thus the relative strength of longitudinal field is expected to be fairly large inside waveguides.

Chapter 5

Conclusions

In this work, nonlinear light-matter interactions occurring at the focal volume of a tightly focused coherent vector light beams were studied. Two new microscopy techniques based on second-harmonic generation were developed. A mathematical treatment based on vector diffraction and Green's functions was applied to model the nonlinear phenomena occurring at the focus, where special emphasis was on second-harmonic generation. Work is under way to generalize the treatment to include modelling of third-order effects, such as third-harmonic generation or coherent anti-Stokes Raman scattering.

First, a microscopy technique to study chiral materials was developed. A theory was formulated and proof-of-principle experiments were performed to demonstrate that the technique is sensitive to the chirality of surfaces but insensitive to the in-plane anisotropy. The result is important, since artifacts due to sample anisotropy are a common hindrance in chiroptical techniques. Currently, we are applying the technique to image biological tissues, where chiroptical signals could be utilized as new morphological constrast mechanisms[139]. We have achieved preliminary results of performing second-harmonic generation circular dichroism (SHG-CD) microscopy on collagenous tissues. The study of collagens is highly relevant, since they are the most abundant protein family of mammalian tissues, and the morphological changes can be linked to severe diseases[139,174,175]. The future efforts are thus directed in developing polarized second-harmonic generation and SHG-CD microscopy further

towards a biomedical diagnostic tool, since in some cases they might provide significant advantages compared to linear techniques.

The second microscopy technique was developed to characterize the optical responses of individual three-dimensional nano-objects. The technique was based on utilizing cylindrical vector beams, and was demonstrated to be potentially a very fast and sensitive tool to study these individual nano-objects and the effects of fabrication defects on their performance. For the fabricated three-dimensional nanocone structures, the defects were seen to sometimes play a substantial role in the optical response. As nanotechnology and consequent utilization of nano-objects are increasingly important for the emergence of new technologies and applications, a fast and sensitive technique capable of characterizing the optical responses of complex nano-objects is expected to become very useful.

Finally, we studied how full treatment of light as a vector quantity can lead to situations that considerably deviate from predictions made by treatments based on scalar diffraction theory. Surprisingly, a new mechanism for multipole effects was discovered, where the multipolar nature of the excitation field itself could be understood as a mechanism for multipolar light-matter interactions. These new effects and deviations from standard scalar theory can start playing a considerable role when light is confined into dimensions comparable to wavelength, which was demonstrated by experiments performed using a high numerical aperture microscope. But strong confinement of light can also occur inside waveguides or near optical antennas, suggesting that the vector treatment will not be only of academic interest. In the future, it would be interesting to study if similar effects could occur and be enhanced inside waveguides as has been recently proposed[171–173].

References

[1] M. Fernández-Suárez and A. Ting. Fluorescent probes for super-resolution imaging in living cells. Nature Reviews Molecular Cell Biology, **9**, 929 (2008).

[2] N. Olivier, M. Luengo-Oroz, L. Duloquin, E. Faure, T. Savy, I. Veilleux, X. Solinas, D. Débarre, P. Bourgine, A. Santos, N. Peyriras, and E. Beaurepaire. Cell lineage reconstruction of early zebrafish embryos using label-free nonlinear microscopy. Science, **329**, 967 (2010).

[3] B. G. Saar, C. W. Freudiger, J. Reichman, C. M. Stanley, G. R. Holtom, and X. S. Xie. Video-rate molecular imaging in vivo with stimulated Raman scattering. Science, **330**, 1368 (2010).

[4] S. Linden, C. Enkrich, M. Wegener, J. Zhou, T. Koschny, and C. Soukoulis. Magnetic response of metamaterials at 100 terahertz. Science, **306**, 1351 (2004).

[5] C. Soukoulis and M. Wegener. Past achievements and future challenges in the development of three-dimensional photonic metamaterials. Nature Photonics, **5**, 523 (2011).

[6] P. Mühlschlegel, H. Eisler, O. Martin, B. Hecht, and D. Pohl. Resonant optical antennas. Science, **308**, 1607 (2005).

[7] L. Novotny and N. van Hulst. Antennas for light. Nature Photonics, **5**, 83 (2011).

[8] M. Minsky. Microscopy apparatus (1961).

[9] T. Maiman. Stimulated optical radiation in ruby. Nature, **187**, 493 (1960).

[10] P. A. Franken, A. E. Hill, C. W. Peters, and G. Weinreich. Generation of Optical Harmonics. Physical Review Letters, **7**, 118 (1961).

[11] R. Hellwarth and P. Christensen. Nonlinear optical microscopic examination of structure in polycrystalline ZnSe. Optics Communications, **12**, 318 (1974).

[12] C. J. R. Sheppard, J. Gannaway, R. Kompfner, and D. Walsh. The scanning harmonic optical microscope. IEEE Journal of Quantum Electronics, **13**, 912 (1977).

[13] W. Denk, J. Strickler, and W. Webb. Two-photon laser scanning fluorescence microscopy. Science, **248**, 73 (1990).

[14] J. Squier and M. Müller. High resolution nonlinear microscopy: A review of sources

and methods for achieving optimal imaging. Review of Scientific Instruments, **72**, 2855 (2001).

[15] W. R. Zipfel, R. M. Williams, and W. Webb. Nonlinear magic: multiphoton microscopy in the biosciences. Nature Biotechnology, **21**, 1369 (2003).

[16] P. J. Campagnola and M. L. Leslie. Second-harmonic imaging microscopy for visualizing biomolecular array, tissues and organisms. Nature Biotechnology, **21**, 1356 (2003).

[17] L. Moreaux, O. Sandre, and J. Mertz. Membrane imaging by second-harmonic generation microscopy. Journal of the Optical Society of America B, **17**, 1685 (2000).

[18] R. M. Williams, W. R. Zipfel, and W. W. Webb. Interpreting Second-Harmonic Generation Images of Collagen I Fibrils. Biophysical Journal, **88**, 1377 (2005).

[19] P. J. Campagnola. Second harmonic generation imaging microscopy: applications to diseases diagnostics. Analytical Chemistry, **83**, 3224 (2011).

[20] X. Chen, O. Nadiarynkh, S. Plotnikov, and P. J. Campagnola. Second harmonic generation microscopy for quantitative analysis of collagen fibrillar structure. Nature Protocols, **7**, 654 (2012).

[21] A. Zumbusch, G. R. Holtom, and X. S. Xie. Three-dimensional vibrational imaging by coherent anti-Stokes Raman scattering. Physical Review Letters, **82**, 4142 (1999).

[22] M. Hashimoto, T. Araki, and S. Kawata. Molecular vibration imaging in the fingerprint region by use of coherent anti-Stokes Raman scattering microscopy with a collinear configuration. Optics Letters, **25**, 1768 (2000).

[23] E. Potma, W. de Boeij, and D. Wiersma. Nonlinear coherent four-wave mixing in optical microscopy. Journal of the Optical Society of America B, **17**, 1678 (2000).

[24] M. Müller, J. Squier, C. A. De Lange, and G. J. Brakenhoff. CARS microscopy with folded BoxCARS phasematching. Journal of Microscopy, **197**, 150 (2000).

[25] C. L. Evans and X. S. Xie. Coherent anti-Stokes Raman scattering microscopy: chemical imaging for biology and medicine. Annual Review of Analytical Chemistry, **1**, 883 (2008).

[26] X. Zhang and Z. Liu. Superlenses to overcome the diffraction limit. Nature Materials, **7**, 435 (2008).

[27] E. Betzig and J. Trautman. Near-field optics: microscopy, spectroscopy, and surface modification beyond the diffraction limit. Science, **257**, 189 (1992).

[28] L. Novotny and S. J. Stranick. Near-field optical microscopy and spectroscopy with pointed probes. Annual Review of Physical Chemisty, **57**, 303 (2006).

[29] M. Gustafsson. Surpassing the lateral resolution limit by a factor of two using structured illumination microscopy. Journal of Microscopy, **198**, 82 (2001).

[30] S. Hell. Toward fluorescence nanoscopy. Nature Biotechnology, **21**, 1347 (2003).

[31] B. Huang, M. Bates, and X. Zhuang. Super resolution fluorescence microscopy. Annual Review of Biochemistry, **78**, 993 (2009).

[32] V. Westphal, S. Rizzoli, M. Lauterbach, D. Kamin, R. Jahn, and S. Hell. Video-rate far-field optical nanoscopy dissects synaptic vesicle movement. Science, **320**, 246 (2008).

[33] S. Jones, S. Shim, J. He, and X. Zhuang. Fast, three-dimensional super-resolution imaging of live cells. Nature Methods, **8**, 499 (2011).

[34] M. Kolobov and C. Fabre. Quantum limits on optical resolution. Physical Review Letters, **85**, 3789 (2000).

[35] C. J. R. Sheppard and A. Choudhury. Annular pupils, radial polarization, and super-resolution. Applied Optics, **43**, 4322 (2004).

[36] V. Giovannetti, S. Lloyd, L. Maccone, and J. H. Shapiro. Sub-Rayleigh-diffraction-bound quantum imaging. Physical Review A, **79**, 013827 (2009).

[37] O. Masihzadeh, P. Schlup, and R. Bartels. Enhanced spatial resolution in third-harmonic microscopy through polarization switching. Optics Letters, **34**, 1240 (2009).

[38] F. Guerrieri, L. Maccone, F. N. C. Wong, J. H. Shapiro, S. Tisa, and F. Zappa. Sub-Rayleigh Imaging via N-Photon Detection. Physical Review Letters, **105**, 163602 (2010).

[39] V. Raghunathan and E. Potma. Multiplicative and subtractive focal volume engineering in coherent Raman microscopy. Journal of the Optical Society of America A, **27**, 2365 (2010).

[40] K. Piché, J. Leach, A. Johnson, J. Salvail, M. Kolobov, and R. Boyd. Experimental realization of optical eigenmode super-resolution. Optics Express, **20**, 26424 (2012).

[41] R. W. Boyd. *Nonlinear Optics* (Academic Press, San Diego, 2003), 2. edition.

[42] H. Kogelnik and T. Li. Laser beams and resonators. Applied Optics, **5**, 1550 (1966).

[43] S. C. Tidwell, D. H. Ford, and W. D. Kimura. Generating radially polarized beams interferometrically. Applied Optics, **29**, 2234 (1990).

[44] S. Quabis, R. Dorn, M. Eberler, O. Glöckl, and G. Leuchs. Focusing light to a tighter spot. Optics Communications, **179** (2000).

[45] K. Youngworth and T. Brown. Focusing of high numerical aperture cylindrical-vector beams. Optics Express, **7**, 77 (2000).

[46] L. Novotny, M. R. Beversluis, K. S. Youngworth, and T. G. Brown. Longitudinal Field Modes Probed by Single Molecules. Physical Review Letters, **86**, 5251 (2001).

[47] Y. R. Shen. *The Principles of Nonlinear Optics* (John Wiley & Sons, Inc., 1984).

[48] P. N. Butcher and D. Cotter. *The Elements of Nonlinear Optics* (Cambridge University Press, 1990).

[49] R. W. Terhune, P. D. Maker, and C. M. Savage. Optical Harmonic Generation in Calcite. Physical Review Letters, **8**, 404 (1962).

[50] N. Bloembergen and P. S. Pershan. Light Waves at the Boundary of Nonlinear Media. Physical Review, **128**, 606 (1962).

[51] C. K. Chen, T. F. Heinz, D. Ricard, and Y. R. Shen. Detection of Molecular Monolayers by Optical Second-Harmonic Generation. Physical Review Letters, **46**, 1010 (1981).

[52] J. M. Brown and S. G. Davies. Chemical asymmetric synthesis. Nature, **342**, 631 (1989).

[53] L. D. Barron. *Molecular light scattering and optical activity* (Cambridge University Press, 1982), 2. edition.

[54] L. Novotny and B. Hecht. *Principles of Nano-optics* (Cambridge University Press, 2007).

[55] A. Zee. *Quantum field theory in a nutshell* (Princeton University Press, 2010), 2. edition edition.

[56] M. R. Beversluis, L. Novotny, and S. Stranick. Programmable vector point-spread function engineering. Optics Express, **14**, 2650 (2006).

[57] C. Maurer, A. Jesacher, S. Fürhapter, S. Bernet, and M. Ritsch-Marte. Tailoring of arbitrary optical vector beams. New Journal of Physics, **9**, 78 (2007).

[58] G. Volpe, S. Cherukulappurath, R. Juanola Parramon, G. Molina-Terriza, and R. Quidant. Controlling the optical near field of nanoantennas with spatial phase-shaped beams. Nano Letters, **9**, 3608 (2009).

[59] Q. Zhan and J. Leger. Focus shaping using cylindrical vector beams. Optics Express, **10**, 324 (2002).

[60] Q. Zhan. Cylindrical vector beams: from mathematical concepts to applications. Advances in Optics and Photonics, **1**, 1 (2009).

[61] T. Brown and Q. Zhan. Introduction: unconventional polarization States of light focus issue. Optics Express, **18**, 10775 (2010).

[62] Y. Kozawa and S. Sato. Focusing property of a double-ring-shaped radially polarized beam. Optics Letters, **31**, 820 (2006).

[63] W. D. Kimura, G. H. Kim, R. D. Romea, L. C. Steinhauer, I. V. Pogorelsky, K. P. Kusche, R. C. Fernow, X. Wang, and Y. Liu. Laser Acceleration of Relativistic Electrons Using the Inverse Cherenkov Effect. Physical Review Letters, **74**, 546 (1995).

[64] A. Nesterov, V. Niziev, and V. Yakunin. Generation of high-power radially polarized beam. Journal of Physics D: Applied Physics, **32**, 2871 (1999).

[65] V. G. Niziev and A. V. Nesterov. Influence of beam polarization on laser cutting efficiency. Journal of Physics D: Applied Physics, **32**, 1455 (1999).

[66] M. Meier, V. Romano, and T. Feurer. Material processing with pulsed radially and azimuthally polarized laser radiation. Applied Physics A: Materials Science & Processing, **86**, 329 (2007).

[67] A. V. Zayats and V. Sandoghdar. Apertureless scanning near-field second-harmonic microscopy. Optics Communications, **178**, 245 (2000).

[68] R. Dorn, S. Quabis, and G. Leuchs. Sharper Focus for a Radially Polarized Light Beam.

Physical Review Letters, **91**, 233901 (2003).

[69] T. Ichimura, N. Hayazawa, M. Hashimoto, Y. Inouye, and S. Kawata. Application of tip-enhanced microscopy for nonlinear Raman spectroscopy. Applied Physics Letters, **84**, 1768 (2004).

[70] E. Y. S. Yew and C. J. R. Sheppard. Tight focusing of radially polarized Gaussian and Bessel-Gauss beams. Optics Letters, **32**, 3417 (2007).

[71] F. Lu, W. Zheng, and Z. Huang. Coherent anti-Stokes Raman scattering microscopy using tightly focused radially polarized light. Optics Letters, **34**, 1870 (2009).

[72] T. Kuga, Y. Torii, N. Shiokawa, T. Hirano, Y. Shimizu, and H. Sasada. Novel optical trap of atoms with a doughnut beam. Physical Review Letters, **78**, 4713 (1997).

[73] Q. Zhan. Trapping metallic Rayleigh particles with radial polarization. Optics Express, **12**, 3377 (2004).

[74] B. Sick, B. Hecht, and L. Novotny. Orientational imaging of single molecules by annular illumination. Physical Review Letters, **85**, 4482 (2000).

[75] A. V. Failla, H. Qian, H. Qian, A. Hartschuh, and A. J. Meixner. Orientational imaging of subwavelength Au particles with higher order laser modes. Nano Letters, **6**, 1374 (2006).

[76] Y. Saito, M. Kobayashi, D. Hiraga, K. Fujita, S. Kawano, N. I. Smith, Y. Inouye, and S. Kawata. z-Polarization sensitive detection in micro-Raman spectroscopy by radially polarized incident light. Journal of Raman Spectroscopy, **39**, 1643 (2008).

[77] A. F. Abouraddy and K. C. Toussaint. Three-Dimensional Polarization Control in Microscopy. Physical Review Letters, **96**, 153901 (2006).

[78] W. Chen and Q. Zhan. Three dimensional polarization control in 4Pi microscopy. Optics Communications, **284**, 52 (2011).

[79] X. Li, T. Lan, C. Tien, and M. Gu. Three-dimensional orientation-unlimited polarization encryption by a single optically configured vectorial beam. Nature Communications, **3**, 998 (2012).

[80] J. Sancho-Parramon and S. Bosch. Dark Modes and Fano Resonances in Plasmonic Clusters Excited by Cylindrical Vector Beams. ACS Nano (2012).

[81] C. Debus, M. A. Lieb, A. Drechsler, and A. J. Meixner. Probing highly confined optical fields in the focal region of a high NA parabolic mirror with subwavelength spatial resolution. Journal of Microscopy, **210**, 203 (2003).

[82] Y. Kozawa and S. Sato. Observation of the longitudinal field of a focused laser beam by second-harmonic generation. Journal of the Optical Society of America B, **25**, 175 (2008).

[83] J. Stadler, C. Stanciu, C. Stupperich, and A. J. Meixner. Tighter focusing with a parabolic mirror. Optics Letters, **33**, 681 (2008).

[84] M. Fleischer, C. Stanciu, F. Stade, J. Stadler, K. Braun, A. Heeren, M. Häffner, D. P.

Kern, and A. J. Meixner. Three-dimensional optical antennas: Nanocones in an apertureless scanning near-field microscope. Applied Physics Letters, **93**, 111114 (2008).

[85] J. S. Ahn, H. W. Kihm, J. E. Kihm, D. S. Kim, and K. G. Lee. 3-dimensional local field polarization vector mapping of a focused radially polarized beam using gold nanoparticle functionalized tips. Optics Express, **17**, 2280 (2009).

[86] S. Winnerl, R. Hubrich, M. Mittendorff, H. Schneider, and M. Helm. Universal phase relation between longitudinal and transverse fields observed in focused terahertz beams. arXiv preprint arXiv:1208.4482 (2012).

[87] T. Grosjean, D. Courjon, and M. Spajer. An all-fiber device for generating radially and other polarized light beams. Optics Communications, **203**, 1 (2002).

[88] G. Volpe and D. Petrov. Generation of cylindrical vector beams with few-mode fibers excited by Laguerre–Gaussian beams. Optics Communications, **237**, 89 (2004).

[89] R. Oron, S. Blit, N. Davidson, A. A. Friesem, Z. Bomzon, and E. Hasman. The formation of laser beams with pure azimuthal or radial polarization. Applied Physics Letters, **77**, 3322 (2000).

[90] J.-F. Bisson, J. Li, K. Ueda, and Y. Senatsky. Radially polarized ring and arc beams of a neodymium laser with an intra-cavity axicon. Optics Express, **14**, 3304 (2006).

[91] Z. Bomzon, V. Kleiner, and E. Hasman. Formation of radially and azimuthally polarized light using space-variant subwavelength metal stripe gratings. Applied Physics Letters, **79**, 1587 (2001).

[92] T. Moser, H. Glur, V. Romano, F. Pigeon, O. Parriaux, M. A. Ahmed, and T. Graf. Polarization-selective grating mirrors used in the generation of radial polarization. Applied Physics B: Lasers and Optics, **80**, 707 (2005).

[93] K. Yoshiki, K. Ryosuke, M. Hashimoto, T. Araki, and N. Hashimoto. Second-harmonic generation microscope using eight-segment polarization-mode converter to observe three dimensional molecular orientation. Optics Letters, **32** (2007).

[94] W. J. Lai, B. C. Lim, P. B. Phua, K. S. Tiaw, H. H. Teo, and M. H. Hong. Generation of radially polarized beam with a segmented spiral varying retarder. Optics Express, **16**, 15694 (2008).

[95] M. Stalder and M. Schadt. Linearly polarized light with axial symmetry generated by liquid-crystal polarization converters. Optics Letters, **21**, 1948 (1996).

[96] H. Ren, Y. Lin, and S. Wu. Linear to axial or radial polarization conversion using a liquid crystal gel. Applied Physics Letters, **89**, 051114 (2006).

[97] L. Novotny. Allowed and forbidden light in near-field optics. II. Interacting dipolar particles. Journal of the Optical Society of America A, **14**, 105 (1997).

[98] J.-X. Cheng and X. S. Xie. Green's function formulation for third-harmonic generation microscopy. Journal of the Optical Society of America B, **19**, 1604 (2002).

[99] E. Y. S. Yew and C. J. R. Sheppard. Effects of axial field components on second harmonic generation microscopy. Optics Express, **14**, 1167 (2006).

[100] J. Dewitz, W. Hübner, and K. Bennemann. Theory for nonlinear Mie-scattering from spherical metal clusters. Zeitschrift für Physik D Atoms, Molecules and Clusters, **37**, 75 (1996).

[101] J. I. Dadap, J. Shan, and T. F. Heinz. Theory of optical second-harmonic generation from a sphere of centrosymmetric material: small-particle limit. Journal of the Optical Society of America B, **21**, 1328 (2004).

[102] A. de Beer and S. Roke. Nonlinear Mie theory for second-harmonic and sum-frequency scattering. Physical Review B, **79**, 155420 (2009).

[103] W. Schaich. Second harmonic generation by periodically-structured metal surfaces. Physical Review B, **78**, 195416 (2008).

[104] Y. Zeng, W. Hoyer, J. Liu, S. Koch, and J. Moloney. Classical theory for second-harmonic generation from metallic nanoparticles. Physical Review B, **79**, 235109 (2009).

[105] J. Lin, H. Wang, W. Zheng, F. Lu, C. J. R. Sheppard, and Z. Huang. Numerical study of effects of light polarization, scatterer sizes and orientations on near-field coherent anti-Stokes Raman scattering microscopy. Optics Express, **17**, 2423 (2009).

[106] W. Nakagawa, R. Tyan, and Y. Fainman. Analysis of enhanced second-harmonic generation in periodic nanostructures using modified rigorous coupled-wave analysis in the undepleted-pump approximation. Journal of the Optical Society of America A, **19**, 1919 (2002).

[107] B. Bai and J. Turunen. Fourier modal method for the analysis of second-harmonic generation in two-dimensionally periodic structures containing anisotropic materials. Journal of the Optical Society of America B, **24**, 1105 (2007).

[108] G. Bachelier, I. Russier-Antoine, E. Benichou, C. Jonin, and P. Brevet. Multipolar second-harmonic generation in noble metal nanoparticles. Journal of the Optical Society of America B, **25**, 955 (2008).

[109] A. Benedetti, M. Centini, C. Sibilia, and M. Bertolotti. Engineering the second harmonic generation pattern from coupled gold nanowires. Journal of the Optical Society of America B, **27**, 408 (2010).

[110] M. Centini, A. Benedetti, C. Sibilia, and M. Bertolotti. Coupled 2D Ag nano-resonator chains for enhanced and spatially tailored second harmonic generation. Optics Express, **19**, 8218 (2011).

[111] J. Mäkitalo, S. Suuriniemi, and M. Kauranen. Boundary element method for surface nonlinear optics of nanoparticles. Optics Express, **19**, 23386 (2011).

[112] V. Krishnamachari and E. Potma. Focus-engineered coherent anti-Stokes Raman scattering microscopy: a numerical investigation. Journal of the Optical Society of America A, **24**, 1138 (2007).

[113] N. Olivier and E. Beaurepaire. Third-harmonic generation microscopy with focus-engineered beams: a numerical study. Optics Express, **16**, 14703 (2008).

[114] N. K. Balla, P. T. C. So, and C. J. R. Sheppard. Second harmonic scattering from small particles using Discrete Dipole Approximation. Optics Express, **18**, 21603 (2010).

[115] N. Balla, E. Y. S. Yew, C. J. R. Sheppard, and P. T. C. So. Coupled and uncoupled dipole models of nonlinear scattering. Optics Express, **20**, 25834 (2012).

[116] C. Hayakawa, V. Venugopalan, V. Krishnamachari, and E. Potma. Amplitude and phase of tightly focused laser beams in turbid media. Physical Review Letters, **103**, 43903 (2009).

[117] C. Hayakawa, E. Potma, and V. Venugopalan. Electric field Monte Carlo simulations of focal field distributions produced by tightly focused laser beams in tissues. Biomedical Optics Express, **2**, 278 (2011).

[118] D. Lipkin. Existence of a new conservation law in electromagnetic theory. Journal of Mathematical Physics, **5**, 696 (1964).

[119] Y. Tang and A. E. Cohen. Optical Chirality and Its Interaction with Matter. Physical Review Letters, **104**, 163901 (2010).

[120] Y. Tang and A. Cohen. Enhanced enantioselectivity in excitation of chiral molecules by superchiral light. Science, **332**, 333 (2011).

[121] E. Hendry, T. Carpy, J. Johnston, M. Popland, R. Mikhaylovskiy, A. Lapthorn, S. Kelly, L. Barron, N. Gadegaard, and M. Kadodwala. Ultrasensitive detection and characterization of biomolecules using superchiral fields. Nature Nanotechnology, **5**, 783 (2010).

[122] M. Schäferling, X. Yin, and H. Giessen. Formation of chiral fields in a symmetric environment. Optics Express, **20**, 26326 (2012).

[123] A. Garcia-Etxarri and J. Dionne. A framework for surface enhanced circular dichroism spectroscopy mediated by non-chiral nanoantennas. arXiv preprint arXiv:1209.0288 (2012).

[124] T. Petralli-Mallow, T. M. Wong, J. D. Byers, H. I. Yee, and J. M. Hicks. Circular dichroism spectroscopy at interfaces: a surface second harmonic generation study. Journal of Physical Chemistry, **97**, 1383 (1993).

[125] J. D. Byers, H. I. Yee, and J. M. Hicks. A second harmonic generation analog of optical rotatory dispersion for the study of chiral monolayers. Journal of Chemical Physics, **101**, 6233 (1994).

[126] J. D. Byers, H. I. Yee, T. Petralli-Mallow, and J. M. Hicks. Second-harmonic generation circular-dichroism spectroscopy from chiral monolayers. Physical Review B, **49**, 14643 (1994).

[127] M. Kauranen, T. Verbiest, J. J. Maki, and A. Persoons. Second-harmonic generation from chiral surfaces. Journal of Chemical Physics, **101**, 8193 (1994).

[128] J. J. Maki, T. Verbiest, M. Kauranen, S. V. Elshocht, and A. Persoons. Comparison of linearly and circularly polarized probes of second-order optical activity of chiral surfaces. Journal of Chemical Physics, **105**, 767 (1996).

[129] M. A. Kriech and J. C. Conboy. Counterpropagating second-harmonic generation: a new technique for the investigation of molecular chirality at surfaces. Journal of the Optical Society of America B, **21**, 1013 (2004).

[130] M. A. Belkin and Y. R. Shen. Non-linear optical spectroscopy as a novel probe for molecular chirality. International Reviews in Physical Chemistry, **24**, 257 (2005).

[131] P. Fischer and F. Hache. Nonlinear optical spectroscopy of chiral molecules. Chirality, **17**, 421 (2005).

[132] T. Verbiest, M. Kauranen, Y. Van Rompaey, and A. Persoons. Optical Activity of Anisotropic Achiral Surfaces. Physical Review Letters, **77**, 1456 (1996).

[133] M. Siltanen, S. Cattaneo, E. Vuorimaa, H. Lemmetyinen, T. J. Katz, K. E. S. Phillips, and M. Kauranen. A regression technique to analyze the second-order nonlinear optical response of thin films. Journal of Chemical Physics, **121**, 1 (2004).

[134] M. Siltanen, E. Vuorimaa, H. Lemmetyinen, P. Ihalainen, J. Peltonen, and M. Kauranen. Nonlinear Optical and Structural Properties of Langmuir-Blodgett Films of Thiohelicenebisquinones. Journal of Physical Chemistry B, **112**, 1940 (2008).

[135] C. Provenzano, P. Pagliusi, A. Mazzulla, and G. Cipparrone. Method for artifact-free circular dichroism measurements based on polarization grating. Optics Letters, **35**, 1822 (2010).

[136] F. Boman, J. Gibbs-Davis, L. Heckman, B. Stepp, S. Nguyen, and F. Geiger. DNA at aqueous/solid interfaces: chirality-based detection via second harmonic generation activity. Journal of the American Chemical Society, **131**, 844 (2008).

[137] S. Ye, K. Nguyen, S. Clair, and Z. Chen. In situ molecular level studies on membrane related peptides and proteins in real time using sum frequency generation vibrational spectroscopy. Journal of Structural Biology, **168**, 61 (2009).

[138] L. Fu, J. Liu, and E. Yan. Chiral sum frequency generation spectroscopy for characterizing protein secondary structures at interfaces. Journal of the American Chemical Society, **133**, 8094 (2011).

[139] X. Chen, C. Raggio, and P. J. Campagnola. Second-harmonic generation circular dichroism studies of osteogenesis imperfecta. Optics Letters, **37**, 3837 (2012).

[140] S. H. Han, N. Ji, M. A. Belkin, and Y. R. Shen. Sum-frequency spectroscopy of electronic resonances on a chiral surface monolayer of bi-naphthol. Physical Review B, **66**, 165415 (2002).

[141] M. A. Kriech and J. C. Conboy. Label-Free Chiral Detection of Melittin Binding to a Membrane. Journal of the American Chemical Society, **125**, 1148 (2003).

[142] M. Oh-e, H. Yokoyama, S. Yorozuya, K. Akagi, M. A. Belkin, and Y. R. Shen. Sum-Frequency Vibrational Spectroscopy of a Helically Structured Conjugated Polymer. Physical Review Letters, **93**, 267402 (2004).

[143] M. Savoini, P. Biagioni, S. Meskers, L. Duo, B. Hecht, and M. Finazzi. Spontaneous Formation of Left- and Right-Handed Cholesterically Ordered Domains in an Enantiopure Chiral Polyfluorene Film. The Journal of Physical Chemistry Letters, **2**, 1359 (2011).

[144] M. Savoini, X. Wu, M. Celebrano, J. Ziegler, P. Biagioni, S. C. J. Meskers, L. Du, B. Hecht, and F. Marco. Circular Dichroism Probed by Two-Photon Fluorescence

Microscopy in Enantiopure Chiral Polyfluorene Thin Films. Journal of the American Chemical Society, **134**, 5832 (2012).

[145] M. A. Kriech and J. C. Conboy. Imaging Chirality with Surface Second Harmonic Generation Microscopy. Journal of the American Chemical Society, **127**, 2834 (2005).

[146] J. C. Sheehan and W. A. Bolhofer. An Improved Procedure for the Condensation of Potassium Phthalimide with Organic Halides. Journal of the American Chemical Society, **72**, 2786 (1950).

[147] G. Decher, B. Tieke, C. Bosshard, and P. Günter. Optical second-harmonic generation in Langmuir-Blodgett films of 2-docosylamino-5-nitropyridine. Journal of the Chemical Society, Chemical Communications, **14**, 933 (1988).

[148] T. Takemoto, M. Eda, M. Hihara, T. Okada, H. Sakashita, M. Eiraku, S. Matzno, M. Gohda, and H. Ebisu. Novel potassium channel openers: synthesis and pharmacological evaluation of new N-(substituted-3-pyridyl)-N'-alkylthioureas and related compounds. Journal of Medicinal Chemistry, **37**, 18 (1994).

[149] T. Verbiest, S. V. Elshocht, M. Kauranen, L. Hellemans, J. Snauwaert, C. Nuckolls, T. J. Katz, and A. Persoons. Strong Enhancement of Nonlinear Optical Properties Through Supramolecular Chirality. Science, **282**, 913 (1998).

[150] K. Phillips, T. Katz, S. Jockusch, A. Lovinger, and N. Turro. Synthesis and Properties of an Aggregating Heterocyclic Helicene. Journal of the American Chemical Society, **123**, 11899 (2001).

[151] M. Decker, M. Ruther, C. Kriegler, J. Zhou, C. Soukoulis, S. Linden, and M. Wegener. Strong optical activity from twisted-cross photonic metamaterials. Optics Letters, **34**, 2501 (2009).

[152] C. Anceau, S. Brasselet, J. Zyss, and P. Gadenne. Local second-harmonic generation enhancement on gold nanostructures probed by two-photon microscopy. Optics Letters, **28**, 713 (2003).

[153] J. Beermann, A. Evlyukhin, A. Boltasseva, and S. I. Bozhevolnyi. Nonlinear microscopy of localized field enhancements in fractal shaped periodic metal nanostructures. Journal of the Optical Society of America B, **25**, 1585 (2008).

[154] B. K. Canfield, H. Husu, J. M. Kontio, J. Viheriälä, T. Rytkönen, T. Niemi, E. Chandler, A. Hrin, J. A. Squier, and M. Kauranen. Inhomogeneities in the nonlinear tensorial responses of arrays of gold nanodots. New Journal of Physics, **10**, 013001 (2008).

[155] J. A. Stratton and L. J. Chu. Diffraction Theory of Electromagnetic Waves. Physical Review, **56**, 99 (1939).

[156] E. Wolf. Electromagnetic Diffraction in Optical Systems. I. An Integral Representation of the Image Field. Proceedings of the Royal Society of London. Series A, Mathematical and Physical Sciences, **253**, 349 (1959).

[157] B. Richards and E. Wolf. Electromagnetic Diffraction in Optical Systems. II. Structure of the Image Field in an Aplanatic System. Proceedings of the Royal Society of London. Series A, Mathematical and Physical Sciences, **253**, 358 (1959).

[158] D. A. Kleinman, A. Ashkin, and G. D. Boyd. Second-Harmonic Generation of Light by Focused Laser Beams. Physical Review, **145**, 338 (1966).

[159] S. Carrasco, B. E. A. Saleh, M. C. Teich, and J. T. Fourkas. Second- and third-harmonic generation with vector Gaussian beams. Journal of the Optical Society of America B, **23**, 2134 (2006).

[160] F. Stade, A. Heeren, M. Fleischer, and D. Kern. Fabrication of metallic nanostructures for investigating plasmon-induced field enhancement. Microelectronic Engineering, **84**, 1589 (2007).

[161] J. M. Kontio, H. Husu, J. Simonen, M. J. Huttunen, J. Tommila, M. Pessa, and M. Kauranen. Nanoimprint fabrication of gold nanocones with 10 nm tips for enhanced optical interactions. Optics Letters, **34**, 1979 (2009).

[162] S. Rao, M. J. Huttunen, J. M. Kontio, J. Mäkitalo, M. R. Viljanen, J. Simonen, M. Kauranen, and D. Petrov. Tip-enhanced Raman scattering from bridged nanocones. Optics Express, **18**, 23790 (2010).

[163] E. J. Sánchez, L. Novotny, and X. S. Xie. Near-Field Fluorescence Microscopy Based on Two-Photon Excitation with Metal Tips. Physical Review Letters, **82**, 4014 (1999).

[164] M. J. Huttunen, J. Mäkitalo, and M. Kauranen. Polarization-controllable winged nanocone tip antenna. Journal of Nonlinear Optical Physics & Materials, **20**, 415 (2011).

[165] S. Berweger, C. C. Neacsu, Y. Mao, H. Zhou, S. S. Wong, and M. B. Raschke. Optical nanocrystallography with tip-enhanced phonon Raman spectroscopy. Nature Nanotechnology, **4**, 496 (2009).

[166] J. Stadler, T. Schmid, and R. Zenobi. Nanoscale chemical imaging using top-illumination tip-enhanced Raman spectroscopy. Nano Letters, **10**, 4514 (2010).

[167] V. Ferry, J. Munday, and H. Atwater. Design considerations for plasmonic photovoltaics. Advanced Materials, **22**, 4794 (2010).

[168] T. Johnson, Z. Lapin, R. Beams, N. Lindquist, S. Rodrigo, L. Novotny, and S. Oh. Highly Reproducible Near-Field Optical Imaging with Sub-20-nm Resolution Based on Template-Stripped Gold Pyramids. ACS Nano, **6**, 9168 (2012).

[169] J. M. Kontio, J. Simonen, J. Tommila, and M. Pessa. Arrays of metallic nanocones fabricated by UV-nanoimprint lithography. Microelectronic Engineering, **87**, 1711 (2010).

[170] J. D. Jackson. *Classical Electrodynamics* (John Wiley & Sons, Inc., 1999), 3. edition edition.

[171] J. B. Driscoll, X. Liu, S. Yasseri, I. Hsieh, J. I. Dadap, and R. M. Osgood Jr. Large longitudinal electric fields (E_z) in silicon nanowire waveguides. Optics Express, **17**, 2797 (2009).

[172] R. M. Osgood Jr, N. C. Panoiu, J. I. Dadap, X. Liu, X. Chen, I. W. Hsieh, E. Dulkeith, W. M. Green, and Y. A. Vlasov. Engineering nonlinearities in nanoscale optical systems: physics and applications in dispersion-engineered silicon nanophotonic wires. Advances in Optics and Photonics, **1**, 162 (2009).

[173] B. Daniel and G. Agrawal. Vectorial nonlinear propagation in silicon nanowire waveguides: polarization effects. Journal of the Optical Society of America B, **27**, 956 (2010).

[174] J. Baum and B. Brodsky. Folding of peptide models of collagen and misfolding in disease. Current Opinion in Structural Biology, **9**, 122 (1999).

[175] P. J. Campagnola and C. Dong. Second harmonic generation microscopy: principles and applications to disease diagnosis. Laser & Photonics Reviews, **5**, 13 (2009).

Appendices

Paper 1

Mikko J. Huttunen, Miro Erkintalo, and Martti Kauranen.

Absolute nonlinear optical probes of surface chirality

Journal of Optics A: Pure and Applied Optics **11**, 034006 (2009).

doi: 10.1088/1464-4258/11/3/034006

Absolute nonlinear optical probes of surface chirality

Mikko J Huttunen, Miro Erkintalo and Martti Kauranen

Department of Physics, Tampere University of Technology, FIN-33101 Tampere, Finland

E-mail: mikko.j.huttunen@tut.fi

Abstract. We propose new nonlinear optical techniques as probes of chirality of surfaces and thin films. The techniques are based on surface second-harmonic generation using focused laser beams. To avoid coupling to the possible anisotropy of the sample, which can also lead to chiral signals and is therefore a problem of traditional second-harmonic probes of surface chirality, the optical beams are applied at normal incidence and possess azimuthal symmetry about the direction of propagation. The handedness is obtained by using incident beams that are circularly-polarized or appropriate superpositions of radially and azimuthally polarized higher-order modes. We model numerically four cases of different sample symmetries and demonstrate that the techniques are only sensitive to chirality but not to anisotropy. The techniques are therefore absolute probes of surface chirality and are naturally applicable to the microscopy of chiral properties of thin fims.

PACS numbers: 42.65.-k, 42.65.Ky, 78.20.-e, 78.20.Bh, 78.68.+m

Keywords: Second-harmonic generation, chirality, radial polarization, vector diffraction theory. Submitted to: *J. Opt. A: Pure Appl. Opt.*

1. Introduction

Chiral molecules lack reflection symmetry and occur in two different enantiomers, which are mirror images of each other. Such molecules interact differently with circularly-polarized (CP) light, which gives rise to optical-activity effects [1]. The differences in the real part of the index of refraction for the two circular polarizations give rise to the rotation of the plane of polarization as linearly polarized light traverses the chiral medium. The differences in the imaginary parts, on the other hand, lead to different absorption coefficients for the circular polarizations (circular dichroism). In isotropic bulk materials, such optical activity effects arise from the lowest-order magnetic contributions to the linear optical response of the chiral medium. Consequently, the effects are rather weak with a typical relative magnitude on the order of $\Delta n/n \sim 10^{-3}$

or less for the index of refraction. Over the past 10-15 years, several nonlinear optical probes of chirality have been developed [2–13]. In particular, second-harmonic generation (SHG) has been shown to be a sensitive probe of chiral surfaces and thin films [2–10, 14, 15]. More specifically, chirality can lead to different efficiency of SHG for the two circular polarizations of fundamental light. In addition, the circular-difference effects can be much stronger than in linear optics, in fact, their relative strength can be on the order of unity. One reason for this is that the optical activity effects in second-order processes can occur within the electric-dipole approximation of the light-matter interaction [3]. However, evidence of magnetic contributions to the nonlinear response has also been provided [7, 14, 16].

The second-harmonic (SH) probes of chirality have traditionally been based on the traditional geometry of surface SHG, where the fundamental beam is applied at a non-normal angle of incidence on the sample and transmitted and/or reflected SH signals are detected. In the plane wave approximation the non-normal angle of incidence is needed so that the polarization of the fundamental light can couple to the surface nonlinearity, where the tensor components of the second-order susceptibility depending on the surface normal are usually important. The chirality of the sample introduces additional non-vanishing tensor components, whose interference with those not arising from chirality (achiral) then gives rise to the circular-difference response. A new treatment beyond the plane wave approximation for normally incident focused Gaussian beams has also been formulated for surfaces of chiral isotropic media [17]. The proposed new techniques as well as the traditional techniques work well for samples with full rotational symmetry about the surface normal (in-plane isotropy). Recently also a new counterpropagating SHG technique has been developed and used [10]. The techniques have also been applied to nonlinear microscopy under the assumption that the sample is isotropic [18, 19].

In-plane anisotropy of the sample can significantly complicate the use of the known and traditional techniques. This is because the azimuthal orientation of an anisotropic sample can give rise to handedness of the whole experimental setup, as determined by the mutual orientations of the surface normal, the in-plane sample axis, and the direction of propagation of the optical beams [20]. Due to the fact that anisotropic samples have more independent tensor components than the isotropic ones, they can also give rise to a different SH response for the two circular polarizations when the setup is chiral. Separation of anisotropy and chirality is an important problem, which can be resolved by complicated measurement techniques, where the azimuthal orientation of the sample is varied [21–24]. Such techniques are clearly not suited to nonlinear microscopy, because it is essentially impossible to guarantee interaction with the same microscopic sample location as the azimuthal orientation is varied. It is evident that for future applications, it is important to develop simplified measurement techniques that are absolute nonlinear probes of chirality and also allow microscopy.

It is intuitively evident that CP light applied at normal incidence on a surface sample cannot be sensitive to in-plane anisotropy, but should possess sensitivity to chirality. However, in the plane wave limit, normal incidence does not allow polarization

components in the direction of the surface normal. This is also a severe limitation, because a general measurement technique should be applicable to samples of arbitrary structure. There are only a few exceptional symmetry groups (e.g., C_1, C_3 and their achiral counterparts) whose susceptibility tensor allows SHG without requiring coupling to the direction of the surface normal.

In this Paper, we introduce novel SHG techniques that can be used as absolute nonlinear probes of surface chirality in the sense that they are not sensitive to in-plane anisotropy. The techniques are based on tightly focused laser beams. The first technique is based on focused CP fundamental beams. Although the circular polarization is well maintained in the focal spot, the full vectorial properties of the process give rise to SH signals where the normal direction plays a role. The second and third techniques are based on superpositions of radially polarized (RP) and azimuthally polarized (AP) beams. Proper combinations of such beams also possess a handedness and are shown to couple to the chirality of the sample. An additional advantage is that focused radial polarization gives rise to a strong polarization component along the surface normal in the focus [25, 26]. As the techniques are based on focused beams, they are naturally applicable to microscopy of chiral properties of surfaces and thin films, thereby extending the capabilities of nonlinear microscopies [27–29].

We note that our proposed techniques have similarities and differences to the technique proposed in [17]. Similarly to our techniques, [17] shows that a normally incident Gaussian beams with waist much larger than wavelength can also be used to probe surface nonlinearity and chirality. But due to the larger beam size the proposed technique is not applicable to nonlinear microscopy as such. In addition, [17] only considers samples with in-plane isotropy, whereas our techniques give rise to chiral signatures independent of possible anisotropy.

2. Theory

We consider a situation where a laser beam is focused to a surface or a thin film using an aplanatic lens, as illustrated in figure 1. For simplicity, we assume that the linear index of refraction of all materials is unity. The fundamental field at frequency ω induces a nonlinear polarization in the sample at the second-harmonic frequency 2ω. In the present work, we only consider electric-dipole interactions between the fields and the sample. The second-order polarization at point $\boldsymbol{r}$ at the SH frequency is thus given by

$$P_i^{(2\omega)}(\boldsymbol{r}) = \sum_{jk} \chi_{ijk}^{(2)}(\boldsymbol{r}) E_j(\boldsymbol{r}) E_k(\boldsymbol{r}) \tag{1}$$

where i,j,k refer to Cartesian components (x,y,z), which is the most convenient frame to describe the sample. $\chi^{(2)}$ is the second-order susceptibility tensor of the surface and $\boldsymbol{E}(\boldsymbol{r})$ is the local electric field vector. When the local polarization is known, the far-field SH radiation pattern can be calculated using a well-known Green's function approach [30–32]. Note that figure 1 also includes additional coordinate systems to describe the focused fundamental field (ρ,φ,z) and the emitted SH (θ,ϕ,R) field.

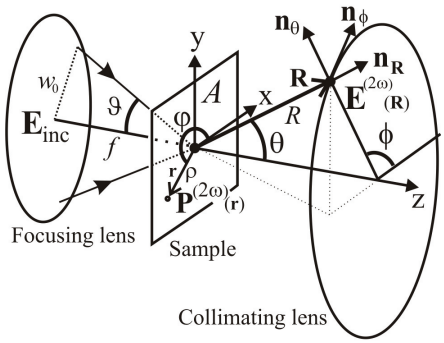

Figure 1. Geometry of second-harmonic generation with focused fundamental field applied at normal incidence on a surface or thin film. The SH field is generated from a surface in the focal plane A and collected by a collecting lens. The sample is most conveniently described using the Cartesian x, y, z coordinate system, wheras the focused fundamental beam and collected second harmonic light are best described using respective spherical coordinates.

As already mentioned, several common sample symmetries require a coupling of the fields to the direction of the surface normal. At the desired normal incidence, significant non-zero normal components can only be achieved through tight focusing and therefore the vectorial nature of the focused electric field must be considered in full. We calculate the local electric field vector $\boldsymbol{E}(\boldsymbol{r})$ in the focal plane A of the lens using vector diffraction theory [26, 33, 34]. Once the vectorial field is known, the nonlinear source polarization of the sample at the SH frequency can be calculated using (1). Finally, the SH power collected by the collecting lens is calculated. By comparing the calculated SH powers for polarized beams of different handednesses, the chirality of a sample can be analyzed.

We first consider the case where the beam before the focusing lens is CP TEM_{00} beam. The Cartesian components of the electric field vector at point $\boldsymbol{r}$ near the focus can be expressed using [26] as

$$\boldsymbol{E}^{00}_{\pm}(\boldsymbol{r}) = \frac{\mathrm{i}kf}{2} E_0 \exp(-\mathrm{i}kf) \times \begin{bmatrix} I_{00} + I_{02}\cos 2\varphi \pm \mathrm{i} I_{02}\sin 2\varphi \\ I_{02}\sin 2\varphi \pm \mathrm{i}(I_{00} - I_{02}\cos 2\varphi) \\ -2\mathrm{i} I_{01}(\cos\varphi \pm \mathrm{i}\sin\varphi) \end{bmatrix} \tag{2}$$

where $k = \lambda/2\pi$ is the wavenumber of the focused beam, f is the focal length of the lens and E_0 is the amplitude of the fundamental beam. The factors I_{00}, I_{01} and I_{02} correspond to integrals over the aperture of the focusing lens [26]

$$I_{00} = \int_0^{\vartheta_{\max}} f_w(\vartheta)\sqrt{\cos\vartheta}\sin\vartheta(1+\cos\vartheta) J_0(k\rho\sin\vartheta)\exp(\mathrm{i}kz\cos\vartheta)\,\mathrm{d}\vartheta \tag{3}$$

$$I_{01} = \int_0^{\vartheta_{\max}} f_w(\vartheta)\sqrt{\cos\vartheta}\sin^2\vartheta \; J_1(k\rho\sin\vartheta)\exp(\mathrm{i}kz\cos\vartheta)\,\mathrm{d}\vartheta \tag{4}$$

$$I_{02} = \int_0^{\vartheta_{\max}} f_w(\vartheta)\sqrt{\cos\vartheta}\sin\vartheta(1-\cos\vartheta) \; J_2(k\rho\sin\vartheta)\exp(\mathrm{i}kz\cos\vartheta)\,\mathrm{d}\vartheta \tag{5}$$

where the angle $\vartheta_{\max}$ is related to the numerical aperture (NA) by relation $\vartheta_{\max} = \sin^{-1}\mathrm{NA}$. The factor $f_w(\vartheta) = \exp(-f^2\sin^2\vartheta/w_0^2)$ is the apodization function [26], $J_n(\cdot)$ is a nth order Bessel function of the first kind and the signs + and − represents right- and left-handed CP beams, respectively. The other parameters are defined in figure 1. From (2) we see that the time average of the electric field has azimuthal symmetry about the direction of propagation. Therefore possible anisotropy of the sample should not give rise to optical-activity effects.

The other techniques are based on the superposition of RP and AP doughnut modes. We consider two different situations schematically illustrated in figure 2. The first situation is based on the superposition of RP and AP modes with no phase difference. The local polarization of the superposition mode is then linear but varies with the azimuthal angle [35]. In the second case we introduce a $\pm\pi/2$ phase difference between the RP and AP modes. Now the local polarization of the superposition is nearly circular. However, the circular polarizations oscillate at different phases at different locations. From here on, we will refer to these superpositions as hybrid radial polarization (HR) and as CP hybrid radial (CPHR), respectively. The electric field vector of HR and CPHR at the point $\boldsymbol{r}$ at the focus of an aplanatic lens can now be expressed using [26] as

$$\boldsymbol{E}_{\pm}^{(\mathrm{CP})\mathrm{HR}}(\boldsymbol{r}) = \frac{-kf^2}{2w_0}E_0\exp(-\mathrm{i}kf) \times \begin{bmatrix} (I_{11}-I_{12})\cos\varphi \pm (\mathrm{i})(I_{11}+3I_{12})\sin\varphi \\ (I_{11}-I_{12})\sin\varphi \mp (\mathrm{i})(I_{11}+3I_{12})\cos\varphi \\ \mathrm{i}4I_{01} \end{bmatrix} \tag{6}$$

where w_0 is the waist of the input beam. The signs ($\pm$ and $\mp$) correspond to different handednesses of the fundamental beam and the imaginary unit in the brackets (i) is used only for CPHR. The factors I_{11} and I_{12} correspond to integrals [26]

$$I_{11} = \int_0^{\vartheta_{\max}} f_w(\vartheta)\sqrt{\cos\vartheta}\sin^2\vartheta(1+3\cos\vartheta) \; J_1(k\rho\sin\vartheta)\exp(\mathrm{i}kz\cos\vartheta)\,\mathrm{d}\vartheta \tag{7}$$

$$I_{12} = \int_0^{\vartheta_{\max}} f_w(\vartheta)\sqrt{\cos\vartheta}\sin^2\vartheta(1-\cos\vartheta) \; J_1(k\rho\sin\vartheta)\exp(\mathrm{i}kz\cos\vartheta)\,\mathrm{d}\vartheta. \tag{8}$$

From (6) it can be seen, that both HR and CPHR beams are radially symmetric but possess intrinsic handedness depending on the sign of the summation.

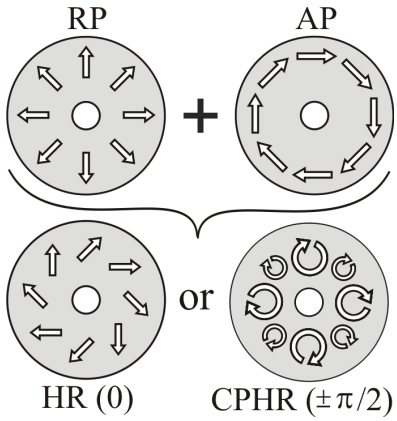

Figure 2. The superposition of RP and AP modes form HR mode when the phase difference between the modes is zero. When the phase difference is $\pm\pi/2$, CPHR mode is created.

Once the local polarization at the SH frequency is known, the radiation pattern of SHG in the far-field can be calculated. Using a Green's function approach, the SH field at point $\boldsymbol{R}$ in spherical coordinates (figure 1) can be shown to be [30–32]

$$\boldsymbol{E}^{(2\omega)}(\boldsymbol{R}) = -\frac{4\omega^2\,\exp(\mathrm{i}2kR)}{c^2R}\iiint_V \exp\left(\frac{-\mathrm{i}2k\boldsymbol{r}\cdot\boldsymbol{R}}{R}\right) \begin{bmatrix} 0 & 0 & 0 \\ \cos\theta\cos\phi & \cos\theta\sin\phi & -\sin\theta \\ -\sin\phi & \cos\phi & 0 \end{bmatrix} \boldsymbol{P}^{(2\omega)}(\boldsymbol{r})\mathrm{d}V \tag{9}$$

where c is the speed of light in vacuum and $\boldsymbol{P}^{(2\omega)}(\boldsymbol{r})$ is calculated using (1)-(8). For surfaces and sufficiently thin films the nonlinear interaction is localized to a thickness Δz, which is much less than optical wavelengths. Then the integration in (9) does not depend on z and becomes

$$\boldsymbol{E}^{(2\omega)}(\boldsymbol{R}) = -\frac{4\Delta z\omega^2\,\exp(\mathrm{i}2kR)}{c^2R}\iint_A \exp\left(\frac{-\mathrm{i}2k\boldsymbol{r}_0\cdot\boldsymbol{R}}{R}\right) \begin{bmatrix} 0 & 0 & 0 \\ \cos\theta\cos\phi & \cos\theta\sin\phi & -\sin\theta \\ -\sin\phi & \cos\phi & 0 \end{bmatrix} \boldsymbol{P}^{(2\omega)}(\boldsymbol{r}_0)\mathrm{d}A \tag{10}$$

where $\boldsymbol{r}_0$ emphasizes the integration over the focal plane A (at $z = 0$). We continue by assuming that the generated SH radiation is collected by a collecting lens. The total collected SH power is then proportional to the integral over a spherical surface of radius

R restricted by the cone angle $\theta_{\max}$ of the collecting lens:

$$P^{\mathrm{SHG}} \propto \int_0^{2\pi} \int_0^{\theta_{\max}} |\boldsymbol{E}^{(2\omega)}(\boldsymbol{R})|^2 R^2 \sin\theta \, \mathrm{d}\theta \mathrm{d}\varphi \tag{11}$$

where $\theta_{\max}$ is related to the NA of the collecting lens by the relation $\theta_{\max} = \sin^{-1}\mathrm{NA}$.

3. Sample symmetries

To demonstrate the potential of the proposed techniques, we consider four cases of thin films with different symmetries. All samples were assumed to be homogeneous and placed in the focal plane A of the focusing lens. The fundamental beams were assumed to be applied at normal incidence with respect to the surface. The cases included combinations where the symmetry of an achiral and isotropic sample was broken by either chirality or anisotropy or both. To be more specific, a surface is achiral if reflection with respect to a plane containing the surface normal is its symmetry operation. As the goal was to demonstrate the sensitivity of the techniques to chirality, the achiral samples thus provided references for the respective chiral cases. For the chiral cases both enantiomers were modeled. The handedness of the enantiomers was changed by changing the signs of the chiral susceptibility components. However, in the present Paper we limit ourselves to cases where SHG requires coupling to the direction of the surface normal. Such sample symmetries have played an important role in the development of the existing nonlinear probes of surface chirality [4–9, 21–24].

In the first case (I), the surface was assumed to belong to the $C_{\infty v}$ symmetry group, i.e., to be isotropic and achiral. The relative values of its tensor components (table 1) were chosen to correspond approximately to the very common case of a poled film of rod-like molecules. In the second case (II), the surface belonged to the C_{∞} symmetry group, and was therefore isotropic but chiral. The chirality of such samples can be investigated even with the traditional techniques based on oblique angles of incidence. The chiral tensor components were assumed to be somewhat smaller than the achiral ones. The third and fourth cases (III and IV) corresponded to the symmetry groups C_{2v} and C_2, respectively. Both surfaces were thus anisotropic, the fourth being also chiral. The anisotropy was introduced by perturbing the values of the tensor components from what is expected for isotropic samples. For the chiral cases II and IV, the calculations were done separately for the real and the imaginary parts of the chiral components. This way we were able to address the chiral signatures arising from different parts of the susceptibility components.

4. Results and discussion

We calculated the total SH powers collected by the second lens for all the four symmetry groups and the incident polarizations corresponding to CP TEM_{00}, HR and CPHR. The NA of both lenses was 0.6 and both lenses were assumed to be at distance $f = 2500\lambda$

Table 1. Relative magnitudes of the non-vanishing susceptibility components of the model cases.

Case	Symmetry	Achiral	Chiral
I	$C_{\infty v}$	zzz=3 zxx=zyy=1 xxz=xzx=yyz=yzy=1	–
II	C_{∞}	zzz=3 zxx=zyy=1 xxz=xzx=yyz=yzy=1	xyz=xzy=$-yxz$=$-yzx$=0.3+0.3i
III	C_{2v}	zzz=3 zxx=1.1 zyy=0.9 xxz=xzx=1.05 yyz=yzy=0.95	–
IV	C_2	zzz=3 zxx=1.1 zyy=0.9 xxz=xzx=1.05 yyz=yzy=0.95	xyz=xzy=0.3+0.3i yxz=yzx=$-$0.15$-$0.15i zxy=zyx=0.1+0.1i

from the surface A. For simplicity λ was normalized to unity. The fundamental beam was assumed to fill the focusing lens, i.e., condition $w_0 = f \sin\vartheta_{\max}$ was assumed to hold. For each mode, the calculations were done for the two polarization states of opposite handedness.

A chiral sample is expected to give rise to different SH responses for the two handednesses of the input polarization. Polarized TEM_{00} beams and SHG circular- and linear-difference (SHG-CD and SHG-LD, respectively) effects have previously been used to probe chirality [2–8, 37]. For the HR and CPHR beams, SH power differences (SHG-PD) can be used as similar probes. For a general quantitative measure of chirality we introduce SHG-PD as

$$\frac{\Delta P^{\mathrm{SHG-PD}}}{P^{\mathrm{ave}}} = \frac{P_+ - P_-}{(P_+ + P_-)/2} \tag{12}$$

where the subscripts $(\pm)$ represent fundamental beams with different handedness. Equation (11) is also applicable for a quantitative measure of traditional SHG-CD and SHG-LD.

The calculated results of the SHG-PD responses are presented in figures 3a-c for CP TEM_{00}, HR and CPHR beams, respectively. For chiral cases the responses were calculated for both enantiomers and the SHG-PD is seen to change sign between the enantiomers, as expected. For CP and CPHR beams, the SHG-PD responses were found to arise from the imaginary parts of the chiral components and no SHG-PD responses were observed when the components were real. This is in agreement with the

earlier results for traditional SHG-CD, which is known to arise from the phase difference between the achiral and chiral tensor components. For the HR beam, the non-zero SHG-PD responses were found to arise from the real parts of the chiral components and no SHG-PD was observed with the imaginary components. No SHG-PD effects were found for the achiral reference cases.

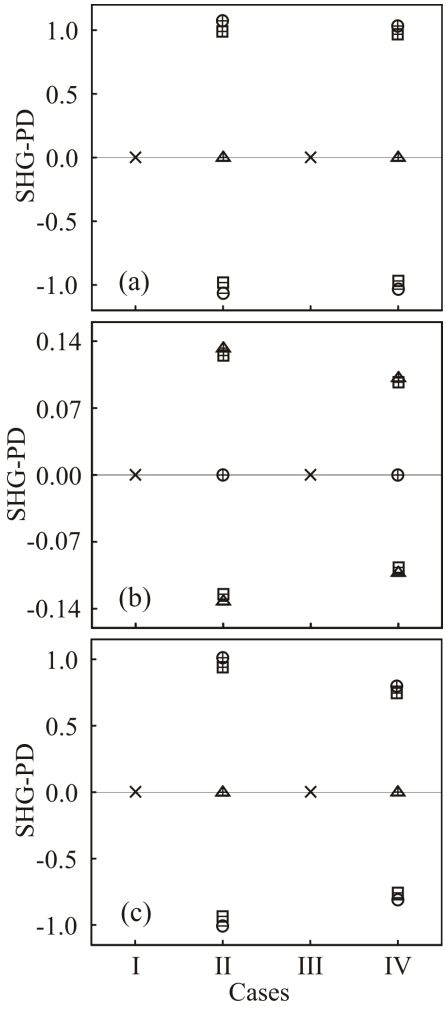

Figure 3. SHG-PD responses of the model cases for (a) CP TEM_{00}, (b) HR and (c) CPHR beams. For chiral cases (II and IV) the responses were calculated using complex chiral susceptibility components (□). In order to address the chiral signatures arising from different parts of the components, calculations were also done using separately the real (△) and the imaginary (O) parts. The signs + and − inside the symbols correspond to different enantiomers of chiral molecules. No SHG-PD responses were found for achiral cases (I and III).

Note that the SHG-PD values are of the order of unity for the circular polarization and for the CPHR beam. However, the value is significantly smaller for the HR beam. The reason for this is that the magnitudes of the nonlinear polarizations for the HR beam, but not for the other two cases, were found to depend strongly on the azimuthal angle of the collecting lens. This dependence leads to the smaller values of SHG-PD responses for the HR beam.

It is important to note that the NA of the system affects the relative strength of the polarization components in the focal regime. Therefore, the coupling between the incident field and the different tensor components depends on the NA used. The chiral signatures arise from the interference between the chiral and achiral tensor components, and therefore depend both on the sample used and the choice of NA. Hence, it is likely that the detection of the chiral signatures for a given sample could be optimized by choosing NA properly. However, for the case of an unknown sample, there is no a priori way to make the proper choice.

5. Conclusions

We have proposed new nonlinear optical techniques, based on SHG, as probes of chirality of surfaces and thin films. The techniques rely on focused laser beams with azimuthal symmetry around the direction of propagation. To avoid the possibility of false chiral signatures arising from the in-plane anisotropy of the samples, the focused beam must be applied at normal incidence on the sample.

To verify the potential of the techniques, we considered four different cases of surface symmetries and calculated the differences in the collected SH power for the two opposite handednesses of the incident beam. According to the results, the techniques are sensitive only to the chirality of the samples but not to their anisotropy. The techniques could therefore be used as simple and absolute probes of chirality of surfaces and, e.g., thin films. Because of the use of focused beams the techniques naturally lend themselves to chiral microscopy of thin films. Experimental work is underway to confirm the theoretical predictions.

Acknowledgments

This work was financially supported by the Academy of Finland (107009, 113245, 114913, 121953) and by the Nanophotonics Research and Development Program funded by the Ministry of Education of Finland. Fruitful discussions with J. A. Squier are greatly appreciated.

References

[1] Barron L D 1982 *Molecular light scattering and optical activity* Cambridge University Press

[2] Petralli-Mallow T, Wong T M, Byers J D, Yee H I and Hicks J M 1993 Circular dichroism spectroscopy at interfaces: a surface second harmonic generation study *J. Phys. Chem.* **97** 1383–8

[3] Byers J D, Yee H I and Hicks J M 1994 A second harmonic generation analog of optical rotatory dispersion for the study of chiral monolayers *J. Chem. Phys.* **101** 6233–41

[4] Byers J D, Yee H I, Petralli-Mallow T and Hicks J M 1994 Second-harmonic generation circular-dichroism spectroscopy from chiral monolayers *Phys. Rev.* B **49** 14643–7

[5] Kauranen M, Verbiest T, Maki J J and Persoons A 1994 Second-harmonic generation from chiral surfaces *J. Chem. Phys.* **101** 8193–9

[6] Verbiest T, Kauranen M, Maki J J, Teerenstra M N, Schouten A J, Nolte R J M and Persoons A 1995 Linearly polarized probes of surface chirality *J. Chem. Phys.* **103** 8296–8

[7] Maki J J, Kauranen M and Persoons A 1995 Surface second-harmonic generation from chiral materials *Phys. Rev.* B **51** 1425–34

[8] Kauranen M, Verbiest T and Persoons A 1998 Second-order nonlinear optical signatures of surface chirality *Journal of Modern Optics* **45** 403–24

[9] Hicks J M (ed) 2002 *Chirality: Physical Chemistry* (*ACS Symposium Series* vol 810, Washington, DC: American Chemical Society)

[10] Kriech M A and Conboy J C 2004 Counterpropagating second-harmonic generation: a new technique for the investigation of molecular chirality at surfaces *J. Opt. Soc. Am.* B **21** 1013–22

[11] Sioncke S, Verbiest T and Persoons A 2003 Second-order nonlinear optical properties of chiral materials *Materials science and engineering* **42** 115–55

[12] Belkin M A and Shen Y R 2005 Non-linear optical spectroscopy as a novel probe for molecular chirality *International Reviews in Physical Chemistry* **24** 257–99

[13] Fischer P and Hache F 2005 Nonlinear optical spectroscopy of chiral molecules *Chirality* **17** 421–37

[14] Schanne-Klein M C, Hache F, Roy A and Flytzanis C 1998 Off resonance second order optical activity of isotropic layers of chiral molecules: Observation of electric and magnetic contributions *J. Chem. Phys.* **108** 9436–43

[15] Mitchell S A and McAloney R A 2004 Second harmonic optical activity of tryptophan derivatives adsorbed at the air/water interface *J. Phys. Chem.* B **108** 1020–9

[16] Kauranen M, Maki J J, Verbiest T, Van Elshocht S and Persoons A 1997 Quantitative determination of electric and magnetic second-order susceptibility tensors of chiral surfaces *Phys. Rev.* B **55** R1985–8

[17] Makarov V A and Perezhogin I A 2008 Generation of reflected second-harmonic light beam with inhomogeneous transversal distribution of polarization from the surface of chiral medium by normally incident Gaussian beam *Optics Communications* **281** 3906–12

[18] Ji N, Zhang K, Yang H and Shen Y R 2006 Three-dimensional chiral imaging by sum-frequency generation *J. Am. Chem. Soc.* **128** 3482–3

[19] Kriech M A and Conboy J C 2005 Imaging chirality with surface second harmonic generation microscopy *J. Am. Chem. Soc.* **127** 2834–5

[20] Verbiest T, Kauranen M, Van Rompaey Y and Persoons A 1996 Optical activity of anisotropic achiral surfaces *Phys. Rev. Lett.* **77** 1456–9

[21] Verbiest T, Van Elshocht S, Kauranen M, Hellemans L, Snauwaert J, Nuckolls C, Katz T J and Persoons A 1998 Strong enhancement of nonlinear optical properties through supramolecular chirality *Science* **282** 913–5

[22] Kauranen M, Van Elshocht S, Verbiest T and Persoons A 2000 Tensor analysis of the second-order nonlinear optical susceptibility of chiral anisotropic thin films *J. Chem. Phys.* **112** 1497–502

[23] Siltanen M, Cattaneo S, Vuorimaa E, Lemmetyinen H, Katz T J, Phillips K E S and Kauranen M 2004 A regression technique to analyze the second-order nonlinear optical response of thin films *J. Chem. Phys.* **121** 1–4

[24] Siltanen M, Vuorimaa E, Lemmetyinen H, Ihalainen P, Peltonen J and Kauranen M 2008 Nonlinear

optical and structural properties of langmuir-blodgett films of thiohelicenebisquinones. *J. Phys. Chem.* B **112** 1940–5

[25] Youngworth K and Brown T 2000 Focusing of high numerical aperture cylindrical-vector beams *Optics Express* **7** 77–87

[26] Novotny L and Hecht B 2007 *Principles of Nano-optics* (Cambridge: Cambridge University Press)

[27] Gannaway J N and Sheppard C J R 1978 Second-harmonic imaging in the scanning optical microscope. *Optical and Quantum Electronics* **10** 435–9

[28] Flörsheimer M, Radüge C, Salmen H, Bösch M, Terbrack R and Fuchs H 1996 In-situ imaging of langmuir monolayers by second-harmonic microscopy *Thin solid films* **284-285** 659–62

[29] LeFloc'h V, Brasselet S, Roch J-F and Zyss J 2003 Monitoring of Orientation in Molecular Ensembles by Polarization Sensitive Nonlinear Microscopy *J. Phys. Chem.* B **107** 12403–10

[30] Novotny L 1997 Allowed and forbidden light in near-field optics. II. interacting dipolar particles *J. Opt. Soc. Am.* A **14** 105–13

[31] Cheng J and Xie X S 2002 Green's function formulation for third-harmonic generation microscopy *J. Opt. Soc. Am.* B **19** 1604–10

[32] Yew E and Sheppard C J R 2006 Effects of axial field components on second harmonic generation microscopy *Opt. Express* **14** 1167–74

[33] Richards B and Wolf E 1959 Electromagnetic diffraction in optical systems. II. structure of the image field in an aplanatic system *Proceedings of the Royal Society of London. Series A, Mathematical and Physical Sciences* **253** 358–79

[34] Quabis S, Dorn R, Eberler M, Glöckl O and Leuchs G 2001 The focus of light - theoretical calculation and experimental tomographic reconstruction *Appl. Phys.* B **72** 109–13

[35] Nesterov A V and Niziev V G 2000 Laser beams with axially symmetric polarization *J. Phys. D: Appl. Phys.* **33** 1817–22

[36] Asatryan A A, Sheppard C J R and de Sterke C M 2004 Vector treatment of second-harmonic generation produced by tightly focused vignetted gaussian beams *J. Opt. Soc. Am.* B **21** 2206–12

[37] Maki J J, Verbiest T, Kauranen M, Van Elshocht S and Persoons A 1996 Comparison of linearly and circularly polarized probes of second-order optical activity of chiral surfaces *J. Chem. Phys.* **105** 767–72

Paper 2

Mikko J. Huttunen, Matti Virkki, Miro Erkintalo, Elina Vuorimaa, Alexander Efimov, Helge Lemmetyinen, and Martti Kauranen.

Absolute probe of surface chirality based on focused circularly polarized light

The Journal of Physical Chemistry Letters **1**, 1826–1829 (2010).

doi: 10.1021/jz100572s

THE JOURNAL OF PHYSICAL CHEMISTRY Letters

pubs.acs.org/JPCL

Absolute Probe of Surface Chirality Based on Focused Circularly Polarized Light

Mikko J. Huttunen,*,† Matti Virkki,† Miro Erkintalo,† Elina Vuorimaa,‡ Alexander Efimov,‡ Helge Lemmetyinen,‡ and Martti Kauranen†

†Department of Physics, Tampere University of Technology, FI-33101 Tampere, Finland, and ‡Department of Chemistry and Bioengineering, Tampere University of Technology, FI-33101 Tampere, Finland

ABSTRACT We present a new nonlinear optical technique to probe chirality, i.e., lack of reflection symmetry, of surfaces and thin molecular films. The technique is based on second-harmonic generation and focusing of circularly polarized light at normal incidence on the sample. Because of the high symmetry of the experimental arrangement, the technique provides an unambiguous probe of chirality in the sense that it avoids false chiral signatures arising from possible in-plane anisotropy of the sample. The technique is verified by using two Langmuir–Blodgett thin films, one chiral and anisotropic, the other achiral and anisotropic, where the latter acted as a reference. Due to the focusing condition, the technique is also naturally applicable to nonlinear chiral microscopy of surfaces and interfaces.

SECTION Surfaces, Interfaces, Catalysis

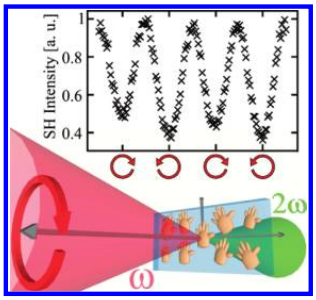

Chiral molecules possess no reflection symmetry and occur in two different enantiomers, which are mirror images of each other. Chiral molecules are optically active (OA), i.e., they have a different response to the two circularly polarized (CP) components of light, which gives rise to the phenomena of optical rotation and circular dichroism.[1] Nonlinear optical phenomena have been found to be sensitive to the chirality of molecules, solutions, surfaces, and thin films.[2−13] Many of the developed techniques are based on second-harmonic generation (SHG),[2−11,14,15] and some are applicable also to nonlinear microscopy.[16,17] Unlike linear OA effects, which usually occur through magnetic contributions to the optical response, nonlinear OA effects are also allowed within the electric-dipole approximation of the light−matter interaction.[3] Due to this, nonlinear OA effects are usually orders of magnitude stronger than linear ones, making nonlinear techniques very sensitive to chirality.

Many of the second-harmonic (SH) chiral probes rely on different efficiency of SHG when the handedness of the incident fundamental light is reversed. For CP light the effect is called second-harmonic generation circular-difference (SHG-CD). In typical SHG-CD experiments on surfaces and thin films, collimated beams and oblique incident angles are used and transmitted, and/or reflected surface SHG is measured.[2−10,14,15] For surface SHG, the components of the second-order susceptibility tensor depending on the surface normal are usually important. Because of this, non-normal angle of incidence is required to couple light with the surface nonlinearity in the plane-wave approximation. For beams of finite transverse size, a treatment of SHG chiral probes beyond paraxial approximation has also been presented.[18] In addition, a technique based on counter-propagating beams has been developed to probe chirality.[10] All the developed techniques work well under the assumption of samples with full rotational symmetry about the surface normal, i.e., for samples with in-plane isotropy.

Unfortunately, in-plane anisotropy of the sample can give rise to SHG-CD effects even for achiral surfaces, thereby significantly complicating the use of traditional techniques on unknown samples.[19] The false chiral signatures arise from the fact that azimuthal orientation of the sample can impose chirality to the whole experimental setup, as determined by the mutual orientations of the surface normal, in-plane anisotropy axis, and the propagation direction of the fundamental beam, as shown in Figure 1. Discrimination of chirality from anisotropy is an important issue, and has previously been solved by tedious measurement techniques, which involve azimuthal rotation of the sample.[20−23] This, however, excludes the applicability of these techniques in nonlinear microscopy, because interaction with the same microscopic area cannot, clearly, be guaranteed as the sample is rotated. For future applications, it is important that new and simple microscopic nonlinear techniques are developed that are unambiguous probes of chirality. This will be of interest in biology and organic chemistry, where the majority of molecular structures are chiral.

In this letter, we demonstrate a new and simple technique based on SHG to detect the chirality of surfaces and thin films, which is not restricted to samples with in-plane isotropy. The technique relies on focusing oppositely handed CP fundamental light at normal incidence on the sample. Due to this

Received Date: May 5, 2010
Accepted Date: May 11, 2010
Published on Web Date: May 27, 2010

DOI: 10.1021/jz100572s | J. Phys. Chem. Lett. 2010, 1, 1826–1829

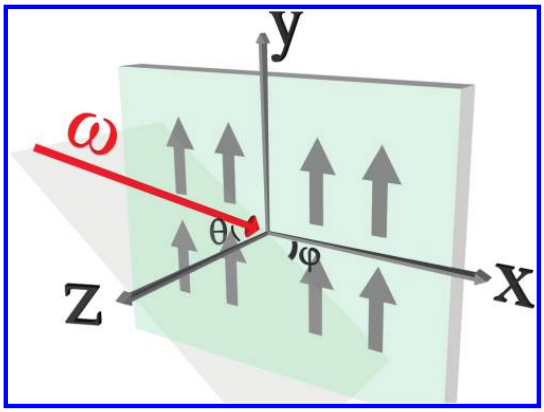

Figure 1. Traditional surface SHG geometry, where a collimated beam at the fundamental frequency ω is incident at angle θ to the sample surface. The in-plane anisotropy axis is shown as up arrows and makes the whole setup chiral when the azimuthal angle φ is other than 0° or ±180°.

geometry, the inherent tendency of surface SHG setups to possess handedness is avoided. The imposed rotational symmetry makes the whole setup achiral, excluding the possibility of false chiral signatures arising from the possible sample anisotropy. The focusing condition and vectorial treatment of polarization is required in order to couple light to the surface nonlinearity, which often depends on the field components along the surface normal. Focusing also makes the technique applicable to chiral nonlinear microscopy of surfaces and thin films.[16,24−27]

In our new technique, second-harmonic generation power difference (SHG-PD) for oppositely handed CP beams acts as the signature of chirality. This SHG-PD response is analogous to the traditional SHG-CD response, but is named differently to emphasize their differences in the range of possible experimental arrangements and theoretical formulation.[28] The SHG-PD response is defined as[33]

$$\frac{\Delta P^{\text{SHG-PD}}}{P^{\text{ave}}} = \frac{P_+ - P_-}{(P_+ + P_-)/2} \qquad (1)$$

where P is the total collected SH power, and the subscripts (±) represent fundamental beams with opposite handedness. A nonzero value of the SHG-PD response therefore acts as a signature of chirality.

We demonstrated our new technique by using two anisotropic Langmuir−Blodgett (LB) thin films. Although the technique is sufficiently sensitive for monolayer detection, the samples used consisted of 16 molecular layers to improve the signal-to-noise ratio. The first LB film consisted of 2-docosylamino-5-nitropyridine (DCANP) molecules, which are known to form anisotropic but achiral molecular layers belonging to symmetry group C_{1h}.[19] DCANP was synthesized according to literature procedures.[29−31] The second LB film was made from a nonracemic mixture of chiral molecules called tetradodecyloxy-helicenebisquinones (THBQs), which form anisotropic and chiral thin films.[20,23,32] The THBQ films belong

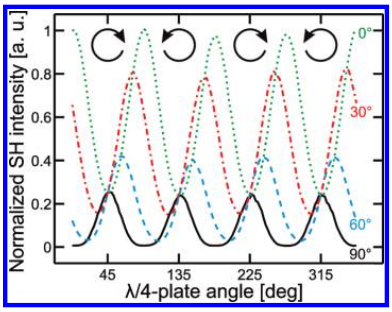

Figure 2. SHG responses of achiral DCANP thin films as a function of the rotation angle of the QWP for different relative angles (0°, 30°, 60°, and 90°) between the input linear polarization and the anisotropy axis of the sample. The angles 45° (225°) and 135° (315°) correspond to oppositely handed CP, and all measured lineshapes overlap at these points.

to symmetry group C_2, which forbids SHG at normal incidence.[23] The achiral DCANP sample was used as a reference to prove that the technique is not sensitive to anisotropy. The previously characterized chiral THBQ sample was used to test the sensitivity to chirality and to compare results with simulations based on a theory of SHG for tightly focused polarized beams.[28]

We measured SHG responses from the THBQ and DCANP samples as a function of the rotation angle of a quarter-wave plate (QWP), which allows us to access the two CP states during the measurements. In order to verify that the orientation of the anisotropic sample does not give rise to false chiral signatures, we used the achiral DCANP reference sample and repeated the measurements for different relative orientations (0°, 30°, 60° and 90°) of the sample anisotropy axis and the initial linear polarization. The results are shown in Figure 2, where the polarization lineshapes for different orientations are very different. The SHG-PD response, however, did not depend on the orientation of the sample and was measured on average as 0.03, which is within the limit of the measurement accuracy and thus effectively zero.

For the THBQ sample, some photobleaching of the signal occurred. To overcome this, smaller average powers (5 mW) and shorter measurement times (0.5 s) were used, which lead to decreased count rates and signal-to-noise ratio compared to the DCANP sample. Simulations of the SHG responses were also performed based on literature values of its SH susceptibility components.[23] The details of the simulations can be found from ref 28. An example of the experimental results is shown in Figure 3. The sample orientation for the shown result was chosen to correspond to the measurements where the SHG signal is at minimum for CP. The measured values of SHG-PD for both samples at different relative angles between the sample and the initial linear polarization are shown in Table 1. The results agree reasonably well with the simulations, although a small positive bias in the SHG-PD responses was visible. This is probably due to small deviations in positioning the samples at normal incidence. The values of Table 1 for both DCANP and THBQ suggest that the SHG-PD has an error limit of about 0.05.

DOI: 10.1021/jz100572s | J. Phys. Chem. Lett. 2010, 1, 1826–1829

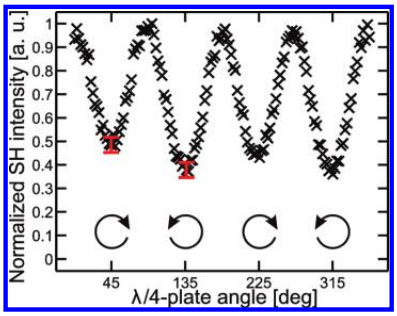

Figure 3. Measured SHG response from a chiral thin film of THBQ as a function of the rotation angle of the QWP. The angles 45°, 135°, 225°, and 315° correspond to CP with varying handedness. The measured SHG-PD response was 0.24.

Table 1. Measured and Calculated SHG-PD Responses at Different Relative Sample Orientations

	SHG-PD response	
orientation of the sample	DCANP	THBQ
0°	0.03	0.24
30°	0.03	0.24
60°	0.03	0.29
90°	0.01	0.28
simulation[a]	0.00	0.19

[a] Orientation did not affect the SHG-PD in calculations.

In conclusion, we have demonstrated a new technique to probe the chirality of thin molecular films with in-plane anisotropy. The technique is based on focusing of CP of opposite handedness at normal incidence onto the sample and measuring intensity differences in SHG when the handedness of the incident laser beam is reversed. The technique was shown to be sensitive only to chirality, but not to anisotropy of the sample. In this sense, the technique is an unambiguous probe of surface chirality. Due to the focusing condition, the technique is directly applicable for SHG microscopy and could prove to be a useful contrast mechanism in imaging of biological samples, where the majority of studied systems are chiral (e.g., DNA, natural lipids, and amino acids).

EXPERIMENTAL METHODS

The experimental setup is similar to a regular nonlinear microscopy configuration (Figure 4). A pulsed laser is focused with an aspheric lens (NA = 0.65) onto the sample, and SHG from the sample is collected in transmission using a collimating lens. No analyzer was used after the collimating lens to avoid introducing chirality to the setup due to the measurement geometry. For thin samples or interfaces, SHG could also be collected in the reflected direction. A mode-locked laser with a short pulse width (~200 fs) is used to enhance the nonlinear response, while minimizing the risk of damaging the sample with high average power. The operating wavelength was centered at 1060 nm. The average laser power at the sample was approximately 20 mW, which for the used

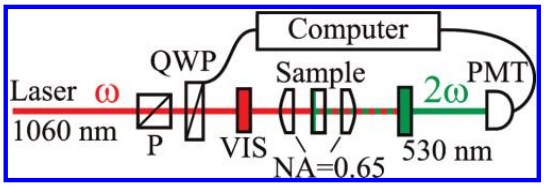

Figure 4. Experimental setup. Polarizer (P) and motorized QWP are used to control the polarization of the fundamental beam. A long-pass filter (VIS) is used to block visible light, and an interference filter is used to pass the frequency doubled signal into the PMT connected to the photon counting unit.

focusing condition is below the known damage thresholds for typical organic or biological materials. The polarization of the fundamental beam was continuously varied from linear to circular by rotating the QWP through 360°. The QWP rotation angles of 45° and 225° corresponded to CP of one handedness, and 135° and 315° corresponded to the opposite handedness. SHG from the samples was collected in the transmitted direction with a lens identical to the focusing lens. The fundamental frequency was filtered out, and the frequency doubled light was passed into the photomultiplier tube (PMT) by a narrowband (10 nm) interference filter centered at 532 nm. The PMT was used with time-correlated photon counting for improved sensitivity and signal-to-noise ratio. Typical noise levels of the used photon counting scheme were less than one count per second, and the measured SHG levels were around a few thousand counts per second. The minimum count rate for the THBQ sample was a little under 2000 counts per second.

AUTHOR INFORMATION

Corresponding Author:

*To whom correspondence should be addressed. E-mail: mikko.j.huttunen@tut.fi.

ACKNOWLEDGMENT This work was financially supported by the Nanophotonics Research and Development Program of the Ministry of Education of Finland and by the Academy of Finland (114913 and 134973). M.J.H. acknowledges support from the Vilho, Yrjö and Kalle Väisälä Foundation. M.E. acknowledges support from the graduate school of Tampere University of Technology. We also thank the research group of T. J. Katz from Columbia University, New York, for providing the sample material.

REFERENCES

(1) Barron, L. D. *Molecular Light Scattering and Optical Activity*; Cambridge University Press: Cambridge, U.K., 1982.
(2) Petralli-Mallow, T.; Wong, T. M.; Byers, J. D.; Yee, H. I.; Hicks, J. M. Circular Dichroism Spectroscopy at Interfaces: A Surface Second Harmonic Generation Study. *J. Phys. Chem.* **1993,** *97*, 1383–1388.
(3) Byers, J. D.; Yee, H. I.; Hicks, J. M. A Second Harmonic Generation Analog of Optical Rotator Dispersion for the Study of Chiral Monolayers. *J. Chem. Phys.* **1994,** *101*, 6233–6241.
(4) Byers, J. D.; Yee, H. I.; Petralli-Mallow, T.; Hicks, J. M. Second-Harmonic Generation Circular-Dichroism Spectroscopy from Chiral Monolayers. *Phys. Rev. B* **1994,** *49*, 14643–14647.

DOI: 10.1021/jz100572s | *J. Phys. Chem. Lett.* **2010,** *1*, 1826–1829

(5) Kauranen, M.; Verbiest, T.; Maki, J. J.; Persoons, A. Second-Harmonic Generation from Chiral Surfaces. *J. Chem. Phys.* **1994,** *101*, 8193–8199.
(6) Verbiest, T.; Kauranen, M.; Maki, J. J.; Teerenstra, M. N.; Schouten, A. J.; Nolte, R. J. M.; Persoons, A. Linearly Polarized Probes of Surface Chirality. *J. Chem. Phys.* **1995,** *103*, 8296–8298.
(7) Maki, J. J.; Kauranen, M.; Persoons, A. Surface Second-Harmonic Generation from Chiral Materials. *Phys. Rev. B* **1995,** *51*, 1425–1434.
(8) Kauranen, M.; Verbiest, T.; Persoons, A. Second-Order Nonlinear Optical Signatures of Surface Chirality. *J. Mod. Opt.* **1998,** *45*, 403–424.
(9) Hicks, J. M., Ed. *Chirality: Physical Chemistry*; ACS Symposium Series; American Chemical Society: Washington, DC, 2002; Vol. 810.
(10) Kriech, M. A.; Conboy, J. C. Counterpropagating Second-Harmonic Generation: A New Technique for the Investigation of Molecular Chirality at Surfaces. *J. Opt. Soc. Am. B* **2004,** *21*, 1013–1022.
(11) Sioncke, S.; Verbiest, T.; Persoons, A. Second-Order Nonlinear Optical Properties of Chiral Materials. *Mater. Sci. Eng., R* **2003,** *42*, 115–155.
(12) Belkin, M. A.; Shen, Y. R. Non-linear Optical Spectroscopy as a Novel Probe for Molecular Chirality. *Int. Rev. Phys. Chem.* **2005,** *24*, 257–299.
(13) Fischer, P.; Hache, F. Nonlinear Optical Spectroscopy of Chiral Molecules. *Chirality* **2005,** *17*, 421–437.
(14) Schanne-Klein, M. C.; Hache, F.; Roy, A.; Flytzanis, C. Off Resonance Second Order Optical Activity of Isotropic Layers of Chiral Molecules: Observation of Electric and Magnetic Contributions. *J. Chem. Phys.* **1998,** *108*, 9436–9443.
(15) Mitchell, S. A.; McAloney, R. A. Second Harmonic Optical Activity of Tryptophan Derivatives Adsorbed at the Air/Water Interface. *J. Phys. Chem. B* **2004,** *108*, 1020–1029.
(16) Ji, N.; Zhang, K.; Yang, H.; Shen, Y. R. Three-Dimensional Chiral Imaging by Sum-Frequency Generation. *J. Am. Chem. Soc.* **2006,** *128*, 3482–3483.
(17) Kriech, M. A.; Conboy, J. C. Imaging Chirality With Surface Second Harmonic Generation Microscopy. *J. Am. Chem. Soc.* **2005,** *127*, 2834–2835.
(18) Makarov, V. A.; Perezhogin, I. A. Generation of Reflected Second-Harmonic Light Beam with Inhomogeneous Transversal Distribution of Polarization from the Surface of Chiral Medium by Normally Incident Gaussian Beam. *Opt. Commun.* **2008,** *281*, 3906–3912.
(19) Verbiest, T.; Kauranen, M.; Van Rompaey, Y.; Persoons, A. Optical Activity of Anisotropic Achiral Surfaces. *Phys. Rev. Lett.* **1996,** *77*, 1456–1459.
(20) Verbiest, T.; Van Elshocht, S.; Kauranen, M.; Hellemans, L.; Snauwaert, J.; Nuckolls, C.; Katz, T. J.; Persoons, A. Strong Enhancement of Nonlinear Optical Properties Through Supramolecular Chirality. *Science* **1998,** *282*, 913–915.
(21) Kauranen, M.; Van Elshocht, S.; Verbiest, T.; Persoons, A. Tensor Analysis of the Second-Order Nonlinear Optical Susceptibility of Chiral Anisotropic Thin Films. *J. Chem. Phys.* **2000,** *112*, 1497–1502.
(22) Siltanen, M.; Cattaneo, S.; Vuorimaa, E.; Lemmetyinen, H.; Katz, T. J.; Phillips, K. E. S.; Kauranen, M. A Regression Technique to Analyze the Second-Order Nonlinear Optical Response of Thin Films. *J. Chem. Phys.* **2004,** *121*, 1–4.
(23) Siltanen, M.; Vuorimaa, E.; Lemmetyinen, H.; Ihalainen, P.; Peltonen, J.; Kauranen, M. Nonlinear Optical and Structural Properties of Langmuir–Blodgett Films of Thiohelicenebisquinones. *J. Phys. Chem. B* **2008,** *112*, 1940–1945.
(24) Gannaway, J. N.; Sheppard, C. J. R. Second-Harmonic Imaging in the Scanning Optical Microscope. *Opt. Quantum Electron.* **1978,** *10*, 435–439.
(25) Flörsheimer, M.; Radüge, C.; Salmen, H.; Bösch, M.; Terbrack, R.; Fuchs, H. In-Situ Imaging of Langmuir Monolayers by Second-Harmonic Microscopy. *Thin Solid Films* **1996,** *284–285*, 659–662.
(26) LeFloc'h, V.; Brasselet, S.; Roch, J.-F.; Zyss, J. Monitoring of Orientation in Molecular Ensembles by Polarization Sensitive Nonlinear Microscopy. *J. Phys. Chem. B* **2003,** *107*, 12403–12410.
(27) Zipfel, W. R.; Williams, R. M.; Webb, W. Nonlinear Magic: Multiphoton Microscopy in the Biosciences. *Nat. Biotechnol.* **2003,** *21*, 1369–1377.
(28) Huttunen, M. J.; Erkintalo, M.; Kauranen, M. Absolute Nonlinear Probes of Surface Chirality. *J. Opt. A: Pure Appl. Opt.* **2009,** *11*, 034006.
(29) Sheehan, J. C.; Bolhofer, W. A. An Improved Procedure for the Condensation of Potassium Phthalimide with Organic Halides. *J. Am. Chem. Soc.* **1950,** *72* (6), 2786–2788.
(30) Takemoto, T.; Eda, M.; Hihara, M.; Okada, T.; Sakashita, H.; Eiraku, M.; Matzno, S.; Gohda, M.; Ebisu, H. Novel Potassium Channel Openers: Synthesis and Pharmacological Evaluation of New *N*-(Substituted-3-pyridyl)-*N*′-alkylthioureas and Related Compounds. *J. Med. Chem.* **1994,** *37* (1), 18–25.
(31) Decher, G.; Tieke, B.; Bosshard, C.; Gunter, P. Optical Second-Harmonic Generation in Langmuir–Blodgett Films of 2-Docosylamino-5-nitropyridine. *J. Chem. Soc., Chem. Commun.* **1988,** 933–934.
(32) Phillips, K. E. S.; Katz, T. J.; Jockusch, S.; Lovinger, A.; Turro, N. Synthesis and Properties of an Aggregating Heterocyclic Helicene. *J. Am. Chem. Soc.* **2001,** *123*, 11899–11907.
(33) Maki, J. J.; Verbiest, T.; Kauranen, M.; Van Elshocht, S.; Persoons, A. Comparison of Linearly and Circularly Polarized Probes of Second-Order Optical Activity of Chiral Surfaces. *J. Chem. Phys.* **1996,** *105*, 767–772.

DOI: 10.1021/jz100572s | *J. Phys. Chem. Lett.* **2010,** *1*, 1826–1829

Paper 3

Mikko J. Huttunen, Godofredo Bautista, Manuel Decker, Stefan Linden, Martin Wegener, and Martti Kauranen.

Nonlinear chiral imaging of subwavelength-sized twisted-cross gold nanodimers

Optical Materials Express **1**, 48–56 (2011).

doi: 10.1364/OME.1.000046

Nonlinear chiral imaging of subwavelength-sized twisted-cross gold nanodimers

Mikko J. Huttunen,[1,*] Godofredo Bautista,[1] Manuel Decker,[2,3] Stefan Linden,[2,3,4] Martin Wegener,[2,3] and Martti Kauranen[1]

[1]*Department of Physics, Tampere University of Technology, FI-33101 Tampere, Finland*
[2]*Institut für Nanotechnologie, Karlsruhe Institute of Technology (KIT), Postfach 3640, D-76021 Karlsruhe, Germany*
[3]*Institut für Angewandte Physik and DFG-Center for Functional Nanostructures (CFN), Karlsruhe Institute of Technology (KIT), D-76128 Karlsruhe, Germany*
[4]*Physikalisches Institut, Universität Bonn, Nußallee 12, 53115 Bonn, Germany*
**mikko.j.huttunen@tut.fi*

Abstract: We perform second-harmonic generation (SHG) microscopy with circularly polarized (CP) light to measure chirality of individual twisted-cross gold nanodimers. The chiral signatures, based on different SHG response for the two CP components of incident light, are clearly visible even with off-resonance excitation. The SHG responses of individual nanodimers are found to vary by about a factor of five. The technique thus has very high sensitivity to the nanoscale deformations of the structure. The chiral signatures of the dimers, however, are found to be more uniform, and the technique is thus able to recognize the handedness of the twisted nanodimers with high reliability.

OCIS codes: (180.4315) Nonlinear microscopy; (190.4350) Nonlinear optics at surfaces; (160.1585) Chiral media; (160.3918) Metamaterials.

References and links

1. L. D. Barron, *Molecular Light Scattering and Optical Activity* (Cambridge University Press, 1982).
2. V. M. Shalaev, "Optical negative-index metamaterials," Nat. Photonics **1**(1), 41–48 (2007).
3. C. M. Soukoulis, S. Linden, and M. Wegener, "Negative refractive index at optical wavelengths," Science **315**(5808), 47–49 (2007).
4. A. S. Schwanecke, A. Krasavin, D. M. Bagnall, A. Potts, A. V. Zayats, and N. I. Zheludev, "Broken time reversal of light interaction with planar chiral nanostructures," Phys. Rev. Lett. **91**(24), 247404 (2003).
5. S. Tretyakov, I. Nefedov, A. Sihvola, S. Maslovski, and C. Simovski, "Waves and energy in chiral nihility," J. Electromagn. Waves Appl. **17**(5), 695–706 (2003).
6. J. B. Pendry, "A chiral route to negative refraction," Science **306**(5700), 1353–1355 (2004).
7. E. Plum, J. Zhou, J. Dong, V. A. Fedotov, T. Koschny, C. M. Soukoulis, and N. I. Zheludev, "Metamaterial with negative index due to chirality," Phys. Rev. B **79**(3), 035407 (2009).
8. S. Zhang, Y.-S. Park, J. Li, X. Lu, W. Zhang, and X. Zhang, "Negative refractive index in chiral metamaterials," Phys. Rev. Lett. **102**(2), 023901 (2009).
9. M. Kuwata-Gonokami, N. Saito, Y. Ino, M. Kauranen, K. Jefimovs, T. Vallius, J. Turunen, and Y. Svirko, "Giant optical activity in quasi-two-dimensional planar nanostructures," Phys. Rev. Lett. **95**(22), 227401 (2005).
10. M. Decker, M. W. Klein, M. Wegener, and S. Linden, "Circular dichroism of planar chiral magnetic metamaterials," Opt. Lett. **32**(7), 856–858 (2007).
11. A. V. Rogacheva, V. A. Fedotov, A. S. Schwanecke, and N. I. Zheludev, "Giant gyrotropy due to electromagnetic-field coupling in a bilayered chiral structure," Phys. Rev. Lett. **97**(17), 177401 (2006).
12. E. Plum, V. A. Fedotov, A. S. Schwanecke, N. I. Zheludev, and Y. Chen, "Giant optical gyrotropy due to electromagnetic coupling," Appl. Phys. Lett. **90**(22), 223113 (2007).
13. J. K. Gansel, M. Thiel, M. S. Rill, M. Decker, K. Bade, V. Saile, G. von Freymann, S. Linden, and M. Wegener, "Gold helix photonic metamaterial as broadband circular polarizer," Science **325**(5947), 1513–1515 (2009).
14. M. Thiel, M. S. Rill, G. von Freymann, and M. Wegener, "Three-dimensional bi-chiral photonic crystals," Adv. Mater. (Deerfield Beach Fla.) **21**(46), 4680–4682 (2009).
15. M. Decker, M. Ruther, C. E. Kriegler, J. Zhou, C. M. Soukoulis, S. Linden, and M. Wegener, "Strong optical activity from twisted-cross photonic metamaterials," Opt. Lett. **34**(16), 2501–2503 (2009).
16. M. Decker, R. Zhao, C. M. Soukoulis, S. Linden, and M. Wegener, "Twisted split-ring-resonator photonic metamaterial with huge optical activity," Opt. Lett. **35**(10), 1593–1595 (2010).

#142344 - $15.00 USD Received 7 Feb 2011; revised 4 Mar 2011; accepted 4 Mar 2011; published 22 Apr 2011

17. M. I. Stockman, D. J. Bergman, C. Anceau, S. Brasselet, and J. Zyss, "Enhanced second-harmonic generation by metal surfaces with nanoscale roughness: nanoscale dephasing, depolarization, and correlations," Phys. Rev. Lett. **92**(5), 057402 (2004).
18. M. W. Klein, C. Enkrich, M. Wegener, and S. Linden, "Second-harmonic generation from magnetic metamaterials," Science **313**(5786), 502–504 (2006).
19. M. W. Klein, M. Wegener, N. Feth, and S. Linden, "Experiments on second- and third-harmonic generation from magnetic metamaterials," Opt. Express **15**(8), 5238–5247 (2007).
20. N. Feth, S. Linden, M. W. Klein, M. Decker, F. B. P. Niesler, Y. Zeng, W. Hoyer, J. Liu, S. W. Koch, J. V. Moloney, and M. Wegener, "Second-harmonic generation from complementary split-ring resonators," Opt. Lett. **33**(17), 1975–1977 (2008).
21. F. B. P. Niesler, N. Feth, S. Linden, J. Niegemann, J. Gieseler, K. Busch, and M. Wegener, "Second-harmonic generation from split-ring resonators on a GaAs substrate," Opt. Lett. **34**(13), 1997–1999 (2009).
22. B. K. Canfield, H. Husu, J. Laukkanen, B. Bai, M. Kuittinen, J. Turunen, and M. Kauranen, "Local field asymmetry drives second-harmonic generation in non-centrosymmetric nanodimers," Nano Lett. **7**(5), 1251–1255 (2007).
23. H. Tuovinen, M. Kauranen, K. Jefimovs, P. Vahimaa, T. Vallius, J. Turunen, N. V. Tkachenko, and H. Lemmetyinen, "Linear and second-order nonlinear optical properties of arrays of noncentrosymmetric gold nanoparticles," J. Nonlinear Opt. Phys. Mater. **11**(4), 421–432 (2002).
24. B. K. Canfield, S. Kujala, K. Jefimovs, J. Turunen, and M. Kauranen, "Linear and nonlinear optical responses influenced by broken symmetry in an array of gold nanoparticles," Opt. Express **12**(22), 5418–5423 (2004).
25. B. K. Canfield, H. Husu, J. Kontio, J. Viheriala, T. Rytkonen, T. Niemi, E. Chandler, A. Hrin, J. A. Squier, and M. Kauranen, "Inhomogeneities in the nonlinear tensorial responses of arrays of gold nanodots," N. J. Phys. **10**(1), 013001 (2008).
26. B. K. Canfield, S. Kujala, K. Laiho, K. Jefimovs, J. Turunen, and M. Kauranen, "Chirality arising from small defects in gold nanoparticle arrays," Opt. Express **14**(2), 950–955 (2006).
27. S. Kujala, B. K. Canfield, M. Kauranen, Y. Svirko, and J. Turunen, "Multipole interference in the second-harmonic optical radiation from gold nanoparticles," Phys. Rev. Lett. **98**(16), 167403 (2007).
28. H. Husu, B. K. Canfield, J. Laukkanen, B. Bai, M. Kuittinen, J. Turunen, and M. Kauranen, "Chiral coupling in gold nanodimers," Appl. Phys. Lett. **93**(18), 183115 (2008).
29. P. M. Rentzepis, J. A. Giordmaine, and K. W. Wecht, "Coherent optical mixing in optically active liquids," Phys. Rev. Lett. **16**(18), 792–794 (1966).
30. A. P. Shkurinov, A. V. Dubrovskii, and N. I. Koroteev, "Second harmonic generation in an optically active liquid: Experimental observation of a fourth-order optical nonlinearity due to molecular chirality," Phys. Rev. Lett. **70**(8), 1085–1088 (1993).
31. P. Fischer, D. S. Wiersma, R. Righini, B. Champagne, and A. D. Buckingham, "Three-wave mixing in chiral liquids," Phys. Rev. Lett. **85**(20), 4253–4256 (2000).
32. M. A. Belkin, T. A. Kulakov, K.-H. Ernst, L. Yan, and Y. R. Shen, "Sum-frequency vibrational spectroscopy on chiral liquids: a novel technique to probe molecular chirality," Phys. Rev. Lett. **85**(21), 4474–4477 (2000).
33. M. Kauranen, T. Verbiest, and A. Persoons, "Second-order nonlinear optical signatures of surface chirality," J. Mod. Opt. **45**(2), 403–423 (1998).
34. J. Hicks, *Chirality: Physical Chemistry, ACS Symposium Series 810* (American Chemical Society, 2002).
35. S. Sioncke, T. Verbiest, and A. Persoons, "Second-order nonlinear optical properties of chiral materials," Mater. Sci. Eng. Rep. **42**(5-6), 115–155 (2003).
36. M. A. Belkin and Y. R. Shen, "Non-linear optical spectroscopy as a novel probe for molecular chirality," Int. Rev. Phys. Chem. **24**(2), 257–299 (2005).
37. T. Verbiest, M. Kauranen, Y. Van Rompaey, and A. Persoons, "Optical activity of anisotropic achiral surfaces," Phys. Rev. Lett. **77**(8), 1456–1459 (1996).
38. M. Siltanen, E. Vuorimaa, H. Lemmetyinen, P. Ihalainen, J. Peltonen, and M. Kauranen, "Nonlinear optical and structural properties of langmuir-blodgett films of thiohelicenebisquinones," J. Phys. Chem. B **112**(7), 1940–1945 (2008).
39. V. A. Makarov and I. A. Perezhogin, "Generation of reflected second-harmonic light beam with inhomogeneous transversal distribution of polarization from the surface of chiral medium by normally incident Gaussian beam," Opt. Commun. **281**(14), 3906–3912 (2008).
40. M. J. Huttunen, M. Erkintalo, and M. Kauranen, "Absolute nonlinear optical probes of surface chirality," J. Opt. A, Pure Appl. Opt. **11**(3), 034006 (2009).
41. M. J. Huttunen, M. Virkki, M. Erkintalo, E. Vuorimaa, A. Efimov, H. Lemmetyinen, and M. Kauranen, "Absolute probe of surface chirality based on focused circularly polarized light," J. Phys. Chem. Lett. **1**(12), 1826–1829 (2010).
42. T. Petralli-Mallow, T. M. Wong, J. D. Byers, H. I. Yee, and J. M. Hicks, "Circular dichroism spectroscopy at interfaces: A surface second harmonic generation study," J. Phys. Chem. **97**(7), 1383–1388 (1993).
43. J. D. Byers, H. I. Yee, and J. M. Hicks, "A second harmonic generation analog of optical rotator dispersion for the study of chiral monolayers," J. Chem. Phys. **101**(7), 6233–6241 (1994).
44. J. D. Byers, H. I. Yee, T. Petralli-Mallow, and J. M. Hicks, "Second-harmonic generation circular-dichroism spectroscopy from chiral monolayers," Phys. Rev. B Condens. Matter **49**(20), 14643–14647 (1994).

#142344 - $15.00 USD Received 7 Feb 2011; revised 4 Mar 2011; accepted 4 Mar 2011; published 22 Apr 2011

45. M. Kauranen, T. Verbiest, J. J. Maki, and A. Persoons, "Second-harmonic generation from chiral surfaces," J. Chem. Phys. **101**(9), 8193–8199 (1994).
46. T. Verbiest, M. Kauranen, J. J. Maki, M. N. Teerenstra, A. J. Schouten, R. J. M. Nolte, and A. Persoons, "Linearly polarized probes of surface chirality," J. Chem. Phys. **103**(18), 8296–8298 (1995).
47. J. J. Maki, T. Verbiest, M. Kauranen, S. V. Elshocht, and A. Persoons, "Comparison of linearly and circularly polarized probes of second-order optical activity of chiral surfaces," J. Chem. Phys. **105**(2), 767–772 (1996).
48. M. C. Schanne-Klein, F. Hache, A. Roy, C. Flytzanis, and C. Payrastre, "Off resonance second order optical activity of isotropic layers of chiral molecules: Observation of electric and magnetic contributions," J. Chem. Phys. **108**(22), 9436–9443 (1998).
49. G. J. Simpson, "Molecular origins of the remarkable chiral sensitivity of second-order nonlinear optics," ChemPhysChem **5**(9), 1301–1310 (2004).
50. S. A. Mitchell and R. A. McAloney, "Second harmonic optical activity of tryptophan derivatives adsorbed at the air/water interface," J. Phys. Chem. B **108**(3), 1020–1029 (2004).
51. M. A. Kriech and J. C. Conboy, "Counterpropagating second-harmonic generation: A new technique for the investigation of molecular chirality at surfaces," J. Opt. Soc. Am. B **21**(5), 1013–1022 (2004).
52. M. A. Kriech and J. C. Conboy, "Imaging chirality with surface second harmonic generation microscopy," J. Am. Chem. Soc. **127**(9), 2834–2835 (2005).
53. N. Ji, K. Zhang, H. Yang, and Y. R. Shen, "Three-dimensional chiral imaging by sum-frequency generation," J. Am. Chem. Soc. **128**(11), 3482–3483 (2006).
54. G. Subramania and S. Y. Lin, "Fabrication of three-dimensional photonic crystal with alignment based on electron beam lithography," Appl. Phys. Lett. **85**(21), 5037–5039 (2004).
55. N. Liu, H. Liu, S. Zhu, and H. Giessen, "Stereometamaterials," Nat. Photonics **3**(3), 157–162 (2009).
56. V. K. Valev, N. Smisdom, A. V. Silhanek, B. De Clercq, W. Gillijns, M. Ameloot, V. V. Moshchalkov, and T. Verbiest, "Plasmonic ratchet wheels: switching circular dichroism by arranging chiral nanostructures," Nano Lett. **9**(11), 3945–3948 (2009).
57. V. K. Valev, A. V. Silhanek, N. Smisdom, B. De Clercq, W. Gillijns, O. A. Aktsipetrov, M. Ameloot, V. V. Moshchalkov, and T. Verbiest, "Linearly polarized second harmonic generation microscopy reveals chirality," Opt. Express **18**(8), 8286–8293 (2010).
58. V. K. Valev, A. V. Silhanek, N. Verellen, W. Gillijns, P. Van Dorpe, O. A. Aktsipetrov, G. A. Vandenbosch, V. V. Moshchalkov, and T. Verbiest, "Asymmetric optical second-harmonic generation from chiral G-shaped gold nanostructures," Phys. Rev. Lett. **104**(12), 127401 (2010).

1. Introduction

Chirality is a fundamental symmetry property of materials, referring to lack of reflection/inversion symmetry in the material system [1]. Chiral molecules thus occur in two mirror-image forms (enantiomers), which cannot be superimposed on top of each other. Chiral materials interact differently with the two circularly polarized (CP) components of light, which give rise to optical activity (OA) effects, such as polarization rotation and circular dichroism [1]. The circular-difference (CD) effects reverse sign between the two enantiomers of a chiral molecule. For isotropic solutions of chiral molecules, the OA effects arise from lowest-order magnetic contributions to the optical response [1]. Due to its relation to broken inversion symmetry, chirality is inherently associated with three-dimensional (3D) molecular structures.

The development of advanced nanofabrication techniques has led to the new research field of metamaterials [2,3], where chirality is an important issue [4]. Chirality has been proposed as an interesting way to achieve negative index of refraction [5–8]. In addition, precise engineering of the structural properties of chiral metamaterials can lead to artificial sub-wavelength features that give rise to giant and broadband OA effects [9–16], which open intriguing possibilities in nanoscale polarization control. Such materials often consist of two-dimensional (2D) arrays of metal nanoparticles. Nevertheless, even then chiral effects arise from the 3D character of real samples [9,10]. In fact, strong polarization effects have been observed with structures that have been designed to be 3D, including double-layer structures, where the interaction in the vertical direction plays a key role [11–16].

Metal nanoparticles are interesting also for nonlinear optics. This is because their plasmonic and magnetic resonances support strong local fields, which can drive the nonlinear responses efficiently [17]. Second-harmonic generation (SHG), e.g., has been observed from split-ring resonators [18–21], T-shaped nanodimers [22], and L-shaped nanoparticles [23,24]. Second-order effects, however, are extremely sensitive to the structural symmetry of the

#142344 - $15.00 USD Received 7 Feb 2011; revised 4 Mar 2011; accepted 4 Mar 2011; published 22 Apr 2011

samples, with chirality and anisotropy having their unique signatures in the polarization-dependent nonlinear responses [23–25]. In fact, this sensitivity is so high that even effects arising from undesired symmetry breaking, including shape distortions and surface defects, affect the responses [26–28]. For metal nanostructures, the overall second-order response thus arises from a complicated interplay between the plasmonic resonances of the particles and their structural defects. This is in strong contrast with the linear optical responses, which can be well predicted by the overall features of the particles.

Another interesting aspect is that, by definition, chirality breaks the centrosymmetry of materials. Chiral materials therefore always have a nonvanishing second-order nonlinear optical response. This occurs even when the material is otherwise highly symmetric, including isotropic materials [29–32]. From the point of view of metamaterials research, chiral nanostructures could thus lead to an intriguing new class of nonlinear materials.

Chiral nanostructures and nonlinear optics thus have two complementary connections. First, nonlinear techniques can provide new probes of chirality to investigate the properties of nanostructures beyond what is possible by linear optical techniques. Second, chiral nanostructures could lead to new types of second-order materials with optimized nonlinear responses. For both aspects, it is essential to develop the basic understanding as to what types of nonlinear schemes couple significantly with the chiral properties of nanostructured materials in the presence of possible imperfections of state-of-the-art samples.

SHG has earlier been used to probe chiral properties of molecular films [33–36]. In the standard geometry of surface SHG, chirality leads to a different SHG response for the two CP components of fundamental light. Unfortunately, such techniques are compromised by possible in-plane anisotropy of the thin-film sample, which can also lead to such a second-harmonic generation circular-difference (SHG-CD) response [37]. This problem arises because the orientation of the anisotropic sample can make the experimental setup chiral. Separation of chirality and anisotropy is thus a significant problem [38] and a particular concern for metamaterials, where the unintended structural features may lead to anisotropy of chiral samples and vice versa. The separation problem can be overcome by increasing the symmetry of the experimental geometry. More specifically, SHG microscopy with a focused CP fundamental beam at normal incidence is only sensitive to chirality, but not to anisotropy [39–41].

In this paper, we demonstrate that SHG microscopy can be used to probe chirality of individual nano-objects, which consist of double-layer twisted-cross gold nanodimers [15]. In order to avoid the false chiral signatures, our technique is based on measuring the different SHG response of the objects for both handedness of CP fundamental light at normal incidence. We find that the SHG responses of individual twisted nanodimers vary. Nevertheless, a twisted-cross of a given handedness has strong preference for one CP and this preference is opposite for the two enantiomers. On the other hand, the normalized SHG-CD response is more uniform. Our results show that SHG microscopy provides a sensitive tool to investigate both the chiral properties of metamaterials and the quality of the samples.

2. Chiral probes based on second-harmonic generation

SHG has been found to be extremely sensitive and highly versatile probe to investigate the chirality of molecules, solutions and thin films [33–36,38–52], and more recently also in the study of metal nanostructures [18–28]. The sensitivity of SHG to chirality originates from its intrinsic sensitivity to symmetry properties. Another advantage of such nonlinear chiral probes is that, unlike linear OA effects, they are allowed within the electric-dipole approximation of the light-matter interaction. Because of this argument, the relative strength of SHG-CD can be on the order of unity and orders of magnitude greater than the relative strength of linear effects, which are typically on the order of $\Delta n / n \sim 10^{-3}$ or less for the index of refraction for the two circular polarizations [43].

#142344 - $15.00 USD Received 7 Feb 2011; revised 4 Mar 2011; accepted 4 Mar 2011; published 22 Apr 2011

SHG-based chiral probes usually rely on different efficiency of SHG for the two CP components of fundamental light. In addition to CP light, and the corresponding SHG-CD response, linearly-polarized light and the corresponding SHG linear-difference (SHG-LD) response have been shown to be chirality-sensitive [43,46]. For molecular thin films, the second-order susceptibility tensor components involving the surface normal are usually important. Typical experiments with collimated beams are therefore performed at oblique incidence [42–50] to generate polarization components along the normal.

The traditional techniques work well under the assumption that the sample has in-plane isotropy, i.e., full rotational symmetry about the surface normal. However, if the sample has in-plane anisotropy, these techniques are compromised because the orientation of the anisotropy axis can make the experiment chiral, which can also give rise to a SHG-CD response [37]. Discrimination between anisotropy and chirality can be achieved by a technique, which involves azimuthal rotation of the sample about its surface normal [38]. It is evident that this approach is not suitable for nonlinear microscopy. On the other hand, we have recently developed a simple SHG technique, which is capable of distinguishing chirality from anisotropy in an unambiguous manner [40,41]. The technique is based on strong focusing of CP light at normal incidence, making the experimental setup rotationally symmetric and thus insensitive to anisotropy. The technique is thus naturally applicable to SHG microscopy of chiral properties even for anisotropic samples, which is not the case in earlier second-order techniques for chiral microscopy, which have implicitly assumed that the sample has in-plane isotropy [51–53].

For molecular films, the technique can be understood on the basis of the nonvanishing components of the second-order susceptibility tensor for various chiral and/or anisotropic symmetry groups and their coupling to all three field components in the focal volume [39,40]. The SHG-CD response can then be shown to arise from interference between the achiral and chiral tensor components [33,43–45], where the latter change sign between the two enantiomers. The susceptibility tensor thus determines the SHG signals that can be measured and their relative strengths.

In the present work, however, we study metal nanodimers, which are known to modify the local-field distribution in the structure. Furthermore, the vectorial local field can contain components not present in the beam incident on the particles [22]. At this time, it is not feasible to track the local fields and their interaction with the local susceptibility tensors. This is not a problem in our measurement technique, however, because the possible SHG signals and their strengths are still determined by the overall symmetry of the nanodimers. In particular, we still expect different SHG response for the two CP components of fundamental light when the sample is chiral, independent of whether it has in-plane anisotropy or not.

The SHG-CD response is best described by the normalized quantity [47]

$$\text{SHG-CD} = \frac{\Delta P_{\text{SHG-CD}}}{P_{\text{AVE}}} = \frac{P_{\text{LHCP}} - P_{\text{RHCP}}}{(P_{\text{LHCP}} + P_{\text{RHCP}})/2}, \tag{1}$$

where P is the collected SHG power and the subscripts LHCP and RHCP indicate the left-hand and right-hand CP components of the fundamental beam. Note that this quantity is defined in such a way that it varies between −2 and 2.

3. Second-harmonic generation microscopy

To characterize the nonlinear response and chirality of the sample, we used a custom-built SHG microscope with CP light as depicted in Fig. 1. A mode-locked Nd:glass laser (Time Bandwidth, Switzerland; fundamental wavelength 1060 nm; pulse width 200 fs; repetition rate 82 MHz; maximum average output power 300 mW) is used as a source of fundamental light. A pinhole-expander assembly (PH, L1, L2) is then used to spatially filter and expand the laser beam. The resulting collimated beam with a diameter of 7 mm is directed to the back-aperture

#142344 - $15.00 USD Received 7 Feb 2011; revised 4 Mar 2011; accepted 4 Mar 2011; published 22 Apr 2011

of an infinity-corrected microscope objective (O1; Nikon LU PLAN Fluor 50 × /NA = 0.80), which then focuses the beam on the sample. This objective is strain-free and was chosen to minimize any undesired polarization deformations when focusing. The focal spot has a waist diameter of 800 nm.

The linear polarization of the fundamental beam is first cleaned up with a calcite polarizer (P) and then controlled with a motorized quarter-wave plate (QWP; Newport) to access the CP states. In particular, the QWP rotation angles of 0°/180° and 90°/270° correspond to right-hand CP (RHCP) and left-hand CP (LHCP) beams.

The transmitted SHG signals were collected by a second microscope objective (O2; Olympus PLAN N 20 × /NA = 0.40). We emphasize that no analyzer was used after O2 to avoid any false chiral effects from the measurement geometry. We used a fundamental wavelength-blocking filter (FF), a narrowband interference filter (IF; 530 nm) and a tube lens (L3) to discriminate and focus the SHG signal onto a cooled photomultiplier tube (PMT).

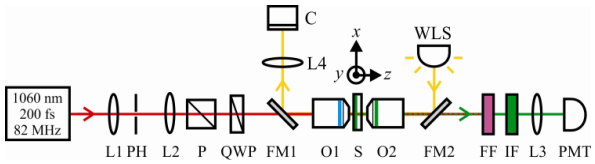

Fig. 1. Schematic diagram of the SHG microscope used for characterizing the nonlinear response and chirality of the twisted-cross nanodimers. The optical setup consists of lenses (L1,L2,L3,L4), pinhole (PH), polarizer (P), motorized quarter-wave plate (QWP), microscope objectives (O1,O2), 3-axis motorized stage (S), flip mirrors (FM1,FM2), fundamental wavelength-blocking filter (FF), interference filter (IF), photomultiplier tube (PMT), white light source (WLS) and camera (C). Ray path colors: fundamental excitation wavelength (red), frequency doubled SHG signal (green), white light (yellow).

The sample is mounted on a 3-axis motorized translation stage (S; Thorlabs MAX301/M) to allow sample scanning. In order to acquire SHG images as a function of sample location, the sample was scanned in the transverse directions across the focal spot in steps of 50 nm. The pixel acquisition time was 5 ms and every single pixel measurement was repeated 4 times and averaged to form the actual pixel value. Note that sample (instead of beam) scanning is preferable to maintain the polarization purity of the fundamental beam in the focal volume. The scanning was accomplished by using a custom program written in LabVIEW. The microscope also included a secondary imaging arm, which consists of a white light source (WLS), two flip mirrors (FM1, FM2), tube lens (L4) and camera (C) to view a specific area of the sample before nonlinear imaging.

4. Double-layer twisted-cross chiral gold nanodimers

Our samples consist of a double-layer structure where each layer itself consists of an array of achiral gold crosses [15]. The chirality arises from the mutual orientation of the crosses in the two layers (Fig. 2) and is therefore directly associated with the 3D character of the structure. A relative twist angle of 22.5° between the crosses in the two layers was chosen to make the unit cell of the double-layer array chiral. The samples were fabricated using a layer-by-layer approach involving electron-beam lithography and spin-on glass planarization [54,55]. Electron-beam lithography was used for the first layer of crosses, which were prepared on a glass substrate covered with a 5 nm thin film of indium-tin-oxide (ITO). In the next step, the surface was planarized with commercial spin-on dielectric (IC1-200, Futurex, Inc.). The dielectric layer was then made thinner by reactive ion etching (SF 6, Plasmalab80Plus, Oxford Instruments Plasma Technology). Finally, a second layer of crosses was fabricated using electron-beam lithography. Great care was taken to align the crosses in the second layer on top of those in the first layer, and maximum misalignment was smaller than 10 nm over the entire sample area. The resulting fabricated crosses are 25 nm thick and separated by a 35 nm

#142344 - $15.00 USD Received 7 Feb 2011; revised 4 Mar 2011; accepted 4 Mar 2011; published 22 Apr 2011

thick spacer. For the present work, where the goal is to address individual chiral nano-objects, the relevant entity is thus a twisted-cross nanodimer, which consists of the two achiral crosses on top of each other. Ideally, the nanodimers belong to the point group symmetry C_4, which for the linear and second-order responses is equivalent to in-plane isotropy.

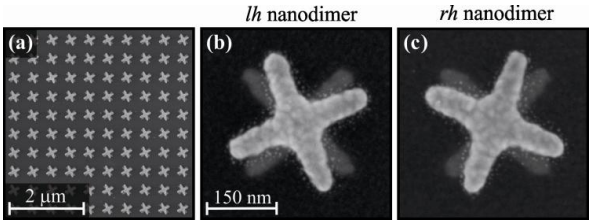

Fig. 2. Large-area electron micrograph of the fabricated twisted-cross nanodimers (a). Close-up views of the *lh* (b) and *rh* (c) twisted-cross nanodimers consisting of two achiral crosses on top of each other.

The twisted-cross nanodimers were ordered in a square array with a 500 nm period. These dimers covered an area of 100 μm x 100 μm. We emphasize that good overall sample quality was achieved as can be clearly seen from Fig. 2(a). Both left-handed (*lh*) and right-handed (*rh*) twisted-cross nanodimers [Figs. 2(b) and 2(c)] were fabricated on the same substrate.

The samples have earlier been characterized by linear transmittance spectroscopy and have been shown to exhibit two distinct resonances, which correspond to the effective oscillation modes of the two coupled crosses [15]. The two resonances occur at wavelengths of 1200 nm and 1550 nm, which are somewhat longer than the fundamental wavelength used in the SHG measurements. The samples have also been reported to exhibit pronounced circular dichroism at the resonance wavelengths and displayed significant optical activity between the two resonances. The linear optical properties are well described by the common approaches for electromagnetic modeling. In the present paper, however, we utilize SHG microscopy to investigate the nonlinear response of the twisted-cross dimers. This technique is expected to be sensitive to the overall chiral structure of the dimers. However, the response may also be modified by the nanoscale surface roughness evident in Figs. 2(a) and 2(b) as well as *in situ* laser-induced damage.

The samples were characterized microscopically by using an average laser power of 5 mW before the illuminating objective (O1) in our microscope (Fig. 1). This power setting provided reasonably detectable SHG signals from the dimers and was significantly smaller than the threshold power estimate of 20 mW from which photodamage at the focal region is observed. At this chosen power level, we obtained highly repeatable microscopy images of the dimers. It is also worth noting that the detected nonlinear responses from the nanodimers actually emanated from the focal region. This was evidenced by rapid attenuation of the measured SHG signals when the sample was moved in small axial displacements away from the focal region.

5. Results and discussions

Representative images acquired using the transmitted SHG signals are shown in Fig. 3 for the *lh* and *rh* twisted-cross samples excited by the LHCP and RHCP fundamental light. The first general observation is that the SHG signals exhibit variations with the 500-nm periodicity of the array. Even though this periodicity is sub-wavelength for the fundamental laser used, our microscope is able to address the overall response of the individual dimers. Another important observation is that the SHG responses of the individual dimers vary, which is better seen from Y-stacked composite SHG line profiles [Figs. 3(c), 3(d), 3(g) and 3(h)]. The peak-to-peak variation of the SHG intensity is about a factor of five. We believe that the strongest

#142344 - $15.00 USD Received 7 Feb 2011; revised 4 Mar 2011; accepted 4 Mar 2011; published 22 Apr 2011

individual hot spots in the images are due to localized defects in some of the dimers, which support particularly strong local fields at the wavelength of our laser and for the particular polarization used. On the other hand, the RMS variation in the SHG signals is on the order of 30%. The detected SHG intensity scales with the square of the effective nonlinear susceptibility of each dimer, which is the fundamental quantity associated with the structure. We may therefore argue that, on the average and in terms of their SHG response, the individual dimers differ from the average by about 15%.

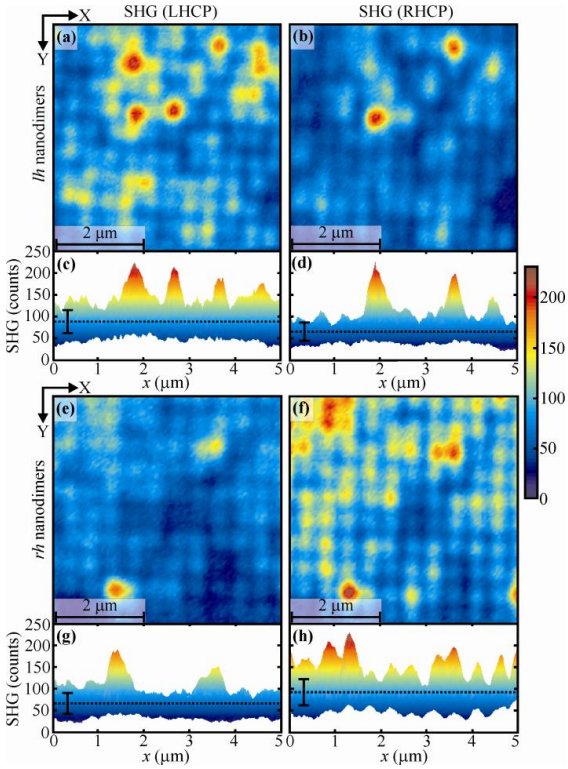

Fig. 3. SHG images of *lh* and *rh* twisted-cross nanodimers using LHCP [(a) and (e)] and RHCP [(b) and (f)] fundamental beam. Y-stacked composite SHG line profiles of the *lh* [(c) and (d)] and *rh* [(g) and (h)] nanodimers illustrate the signal variation. Average SHG values are shown as black dotted lines [(c), (d), (g) and (h)] together with the calculated standard deviation bars.

In spite of the local variations in the SHG responses of the individual dimers, our technique has very good sensitivity to the chirality of the dimers. The *lh* twisted dimers clearly give a stronger SHG signal for the LHCP fundamental light [Figs. 3(a) to 3(d)], whereas the *rh* dimers prefer the RHCP light [Figs. 3(e) to 3(h)]. Interestingly, such chiral signatures, based on different SHG response for the two CP components of incident light, are clearly visible even with off-resonance excitation.

In order to analyze this further, we present the normalized SHG-CD images and Y-stacked composite line profiles of the two samples in Fig. 4. The local CD responses are seen to be more uniform than the original SHG signals, which is evident especially by comparing the Y-stacked composite SHG line profiles [Figs. 3(c), 3(d), 3(g) and 3(h)] and SHG-CD [Figs. 4(c)

#142344 - $15.00 USD Received 7 Feb 2011; revised 4 Mar 2011; accepted 4 Mar 2011; published 22 Apr 2011

and 4(d)]. More importantly, the average SHG signals of Fig. 3 for the two polarizations are within each other's error bars, whereas those of the SHG-CD response of Fig. 4 are not. The SHG-CD responses averaged over the whole image area are found to be –0.32 for the *lh* and 0.35 for the *rh* structures. The almost equal magnitudes and opposite signs are in excellent agreement with the expected result. Regardless of the few individual dimers that give rise to a SHG-CD response of the wrong sign, the CD response is thus strongly correlated with the handedness of the dimer.

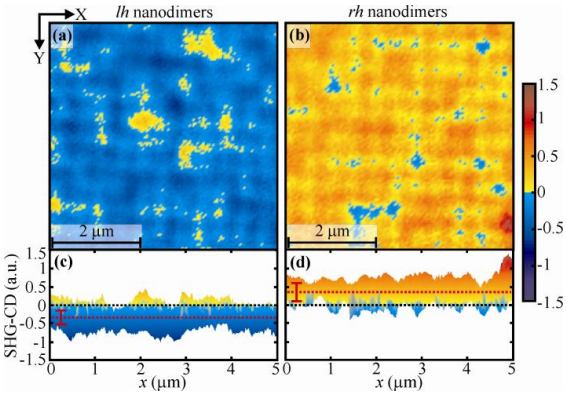

Fig. 4. SHG-CD images of *lh* (a) and *rh* (b) twisted-cross nanodimers derived using the images in Fig. 3. Y-stacked composite SHG-CD line profiles [(c) and (d)] illustrate the pixelwise SHG-CD values of (a) and (b). Coloring highlights the sign of the response and thus the chirality of the structures. Averaged SHG-CD responses of the scanned areas are –0.32 and 0.35 for the *lh* and *rh* structures, respectively. Those are shown as red dotted lines in (c) and (d) together with the calculated standard deviation bars. Zero reference levels are marked as black dotted lines in (c) and (d).

To estimate the reliability of the SHG-CD response in detecting the handedness of the individual dimers, we calculated the percentages of pixels with the proper sign of the CD response for the *lh* and *rh* twisted dimers, which were 93% and 95%, respectively. In addition, the CD responses with the wrong sign do not arise from the limitations of the technique but are related to the properties of the sample. Furthermore, the SHG-CD responses of the wrong sign are at least partly related to the presence of exceptionally strong SHG signals, e.g., the two very bright dimers in Fig. 3(b). As already mentioned, such very bright signals are most likely due to strongly favorable defects of the particular dimer for efficient SHG. These results imply that we are able to recognize the handedness of individual nanodimers quite reliably even though their overall SHG responses vary.

We next return to the possible role of defects in SHG from the present samples. Our twisted dimers belong ideally to the point group symmetry C_4, which is equivalent to in-plane isotropy of the sample for SHG. For this symmetry, SHG signals can only be generated in the presence of field components in the direction of the sample normal [39–41]. Our microscopic technique gives rise to such longitudinal field components even when the experiment is performed at normal incidence. Under our focusing conditions, however, the field amplitudes of the longitudinal components remain an order of magnitude weaker than the transverse components.

Any defects of an individual dimer, however, can break its ideal symmetry and give rise to in-plane anisotropy and in-plane chirality. This would allow SHG even with in-plane field components. If such symmetry breaking effects were strong, we would expect both the SHG signals and the SHG-CD responses to vary essentially randomly from one dimer to another.

#142344 - $15.00 USD Received 7 Feb 2011; revised 4 Mar 2011; accepted 4 Mar 2011; published 22 Apr 2011

This is particularly so because the transverse field components are significantly stronger than the longitudinal components. For the present samples, however, the SHG signals vary more than the SHG-CD responses. This suggests that the role of the defects is to influence mainly the coupling of the dimers to the longitudinal field components, but not to break the in-plane symmetry of the samples. Such effects would thus mainly affect the absolute SHG signals but be less important for the SHG-CD response. The results of the SHG measurements thus suggest that the overall quality of the samples is very good.

We finally note that other authors have also used SHG to address chiral nanostructures in a traditional surface SHG setup [56–58]. Their samples consisted of single-layer arrays of G-shaped metal structures. Both SHG-CD [56] and SHG-LD [57,58] effects were observed. The SHG-CD response was shown to arise from supraelement level in which the relative orientation of the adjacent particles was crucial, although even individual G's are chiral. Furthermore, the size of the G particles was about 1 μm wide. The particles were thus larger than the 800 nm wavelength of the laser used. Consequently, in the microscopic measurements, the authors were able to address parts of individual particles and attempted to correlate them to the possible hot spots of the local-field distribution. In contrast to this, our twisted-cross nanodimers have sub-wavelength size. We have therefore measured the overall response of the individual dimers, which is more directly associated with its structural symmetry independent of the details of the local-field distribution within the dimers.

6. Conclusion

In conclusion, we have demonstrated that second-harmonic generation microscopy with circularly polarized light can be utilized to probe chirality of individual subwavelength-sized objects. The technique is very sensitive to nanoscale structural features of metal nanoparticles, where the overall second-harmonic response arises from a complicated interplay of the plasmonic resonances of individual particles and their structural defects. For samples of low quality, the response could even be dominated by symmetry-breaking defects of the structure.

In the present paper, the technique was applied to double-layer twisted-cross chiral gold nanodimers organized in a two-dimensional array. Our microscope was able to resolve individual dimers, whose second-harmonic responses were found to vary significantly. Although the RMS variation in the responses was relatively small, some nanodimers were found to lead to significantly higher second-harmonic response. This behavior was explained by the nanoscale defects of the particular dimers that are favorable for efficient second-harmonic generation for the wavelength and circular polarization used.

In spite of the large variations in the second-harmonic responses of individual dimers, the general observation is that dimers of a given handedness lead to stronger second-harmonic generation for one circular polarization of fundamental light than the other. For the samples investigated, the average circular-difference response in the second-harmonic efficiency was on the order of 0.35. The circular-difference response was also found to vary between individual nanodimers. Importantly, however, the circular-difference response was significantly more uniform than the second-harmonic signals themselves. The technique thus provides a reliable way to address the handedness of chiral nano-objects.

Due to its superior sensitivity to the structural features of nano-objects and their chiral properties, we expect polarized second-harmonic generation microscopy to become a useful tool in the characterization of the quality and symmetry of nanostructures. In the future, it will also be interesting to extend the technique from circular-difference effects to a more complete tensor analysis of the nonlinear response of individual nanoparticles.

Acknowledgements

This work was funded by the ANIMOS Consortium project under the Research Program on Photonics and Modern Imaging Techniques of the Academy of Finland (project 134973). MJH acknowledges support from the Graduate School of Modern Optics and Photonics in

#142344 - $15.00 USD Received 7 Feb 2011; revised 4 Mar 2011; accepted 4 Mar 2011; published 22 Apr 2011

Finland. The Karlsruhe team acknowledges support by the Deutsche Forschungsgemeinschaft (DFG), the State of Baden-Württemberg, and the Karlsruhe Institute of Technology (KIT) through the DFG Center for Functional Nanostructures (CFN) within subproject A1.5. The project PHOME acknowledges the financial support of the Future and Emerging Technologies (FET) programme within the Seventh Framework Programme for Research of the European Commission, under FET-Open grant number 213390. The project METAMAT is supported by the Bundesministerium für Bildung und Forschung (BMBF).

#142344 - $15.00 USD Received 7 Feb 2011; revised 4 Mar 2011; accepted 4 Mar 2011; published 22 Apr 2011

Paper 4

Godofredo Bautista, Mikko J. Huttunen, Jouni Mäkitalo, Juha M. Kontio, Janne Simonen, and Martti Kauranen.

Second-harmonic generation imaging of metal nano-objects with cylindrical vector beams

Nano Letters **12**, 3207–3212 (2012).

doi: 10.1021/nl301190x

NANO LETTERS

Letter

pubs.acs.org/NanoLett

Second-Harmonic Generation Imaging of Metal Nano-Objects with Cylindrical Vector Beams

Godofredo Bautista,*[,†] Mikko J. Huttunen,[†] Jouni Mäkitalo,[†] Juha M. Kontio,[‡] Janne Simonen,[‡] and Martti Kauranen[†]

[†]Department of Physics and [‡]Optoelectronics Research Center, Tampere University of Technology, Tampere, Finland

Supporting Information

ABSTRACT: We introduce an imaging technique based on second-harmonic generation with cylindrical vector beams that is extremely sensitive to three-dimensional orientation and nanoscale morphology of metal nano-objects. Our experiments and second-harmonic field calculations based on frequency-domain boundary element method are in very good agreement. The technique provides contrast for structural features that cannot be resolved by linear techniques or conventional states of polarization and shows great potential for simple and cost-effective far-field optical imaging in plasmonics.

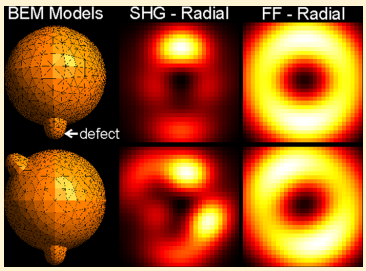

KEYWORDS: *Metal nano-object, second-harmonic generation, cylindrical vector beams, nonlinear microscopy, boundary element method, plasmonics*

The linear optical response of metal nano-objects is mostly governed by the lightning-rod effect and localized surface plasmon (LSP) resonances.[1] The lightning-rod effect arises from the fact that the electric charges accumulate at the geometrically sharp and pointed features of metal structures. Such accumulation is primarily driven by the electric field polarized along the tip axis.[2] On the other hand, the LSP resonances arise from collective oscillations of electrons in the nano-objects and are more sensitive to the excitation wavelength. Furthermore, they depend on the properties of the nano-objects, such as type of metal and geometry, and the properties of the surrounding medium.[1] In addition, they can be controlled by particle interactions, for example, the interparticle distance in an array,[3] by the relative particle orientation in dimers,[4] and by Fano resonances.[5−7]

Imaging metal nano-objects poses a demanding task due to their nanoscale dimensions. Scanning electron microscopy (SEM) and atomic force microscopy (AFM) have been typically used to directly inspect their morphology. Additionally, electron energy-loss spectroscopy,[8] cathodoluminescence,[9] near-field scanning optical microscopy,[10] photoemission electron microscopy,[11] tip-enhanced photoluminescence[12,13] and similar near-field modalities[14,15] have been applied to map the distribution of LSPs and the resulting local-field enhancements. Although such techniques provide high-resolution imaging, their implementation requires complicated instrumentation. Alternatively, far-field microscopy schemes exploiting linear and nonlinear optical processes have been demonstrated. The use of nonlinear optical processes has an advantage in terms of resolution and provides additional sources of contrast due to multiphoton interactions. Furthermore, these multiphoton processes may even be amplified by the strong local fields generated in the vicinity of metal nano-objects. Such techniques have been demonstrated using two-photon excited luminescence,[16] nonlinear four-wave mixing,[17] and harmonic generation.[18−23]

Of the far-field nonlinear techniques, second-harmonic generation (SHG), which is the conversion of the incident optical field at frequency ω to the second-harmonic field at frequency 2ω, is the simplest and most common. In recent years, SHG has been used to characterize various metal nano-objects such as nanodots,[24] L-shaped nanoparticles,[25,26] T-shaped nanodimers,[27] split-ring resonators,[28] G-shaped nanostructures,[29] twisted-cross nanodimers,[30] and sharp tips.[12,13,31] The main advantages of SHG lie in the added sensitivity toward local fundamental fields due to the nonlinear interaction and in its sensitivity to structural symmetry.[1] Moreover, it has been shown that subwavelength-sized deformations from ideal structures can lead to undesired symmetry breakings and thus affect the overall nonlinear responses.[19,32−37] This structural sensitivity is very hard to achieve using other optical techniques.

Simultaneously, there has been growing interest in polarization beam shaping particularly for doughnut-shaped cylindrical vector beams (CVBs) with azimuthal (AP) and radial polarizations (RP).[38] When these beams are focused, the intensity distributions of their transverse electric-field components preserve the doughnut-shaped intensity patterns and

Received: March 28, 2012
Revised: May 14, 2012
Published: May 15, 2012

corresponding polarizations.[1,39] However when all the electric-field components are considered, the RP beam focus exhibits a Gaussian-like intensity distribution due to the presence of a strong field component along the optical axis, usually referred to as longitudinal component.[40] Although AP and RP beams have been shown to be versatile orientation probes in far-field optical microscopy of single molecules,[41] nanocrystals[42,43] and metal nanoparticles,[44,45] these reports are mainly restricted to the use of linear optical processes. On the other hand, SHG microscopy using RP beams has been demonstrated for orientation imaging of biological structures.[46]

In this Letter, we show that SHG with focused CVBs is extremely sensitive to the three-dimensional (3D) orientation and morphology of metal nano-objects. To verify this technique, we image the SHG intensity distribution in individual subwavelength-sized gold nanobumps and nanocones using focused AP and RP beams. To understand the experimental SHG images, we provide SHG field calculations based on the frequency-domain boundary element method (BEM). The technique is shown to provide contrast for structural features that cannot be discriminated by linear techniques or conventional states of polarization.

Arrays of gold nanobumps and nanocones with different particle-to-particle distances were fabricated on glass substrates using ultraviolet-nanoimprint lithography (UV-NIL) combined with electron-beam evaporation.[31] The master template was fabricated on a silicon wafer using electron-beam lithography. The resulting patterns on the template were then transferred to polydimethylsiloxane stamp. Next, a glass substrate was coated with a 600 nm thick poly(methyl methacrylate) film, a germanium intermediate layer, and a UV-NIL resist layer (Amonil, AMO GmbH). A mask aligner (EVG 620) using the PDMS stamp was then used for nanoimprinting. Reactive ion etching was used to form cylindrical hole patterns in the resist exposing the substrate surface. Next, layers of titanium adhesion (20 nm) and gold (100−400 nm) were deposited using an electron-beam evaporator. Depending on the amount of the gold used in the evaporation, nanobumps (height ∼ 100 nm) or nanocones (height ∼ 300−400 nm) can be fabricated. Lastly, lift-off was performed in Microposit Remover 1165 resist stripper (Shipley Co.) with ultrasonic agitation. Shown in Figure 1a is a SEM image of a region in the fabricated array of gold nanobumps with a period of 2 μm. A SEM image of a nanobump with a base diameter of 160 nm and a height of 80 nm is depicted in Figure 1b. The residual in-plane anisotropy of the nanobump is used for sensitive 2D orientation imaging using SHG with CVBs. On the other hand, a SEM image of a nanocone with a base diameter of 150 nm, a height of 300 nm, and a tip diameter of 20 nm is shown in Figure 1c. The resulting conical geometry is used for 3D orientation imaging as well as field localization.

To characterize the nano-objects, we used a custom-built stage-scanning SHG microscope operating in reflection. A mode-locked femtosecond Nd:glass laser (wavelength 1060 nm, pulse length 200 fs, repetition rate 82 MHz) was used for excitation. Upon polarization cleaning, collimation and expansion, the output beam was directed to the back-aperture of an infinity-corrected (50×, 0.8 NA) and strain-free microscope objective. The objective was used to focus the beam onto the sample which is mounted on a three-axis motorized translation stage. The reflected fundamental and SHG signals were collected by the same objective and spectrally discriminated by a dichroic mirror. To extract the backscattered

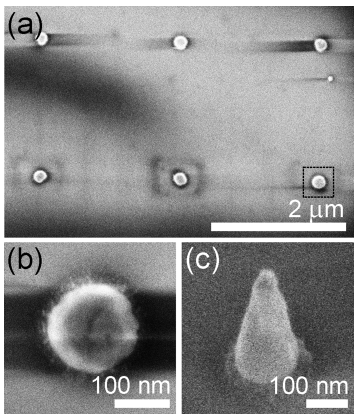

Figure 1. (a) SEM image of an array of gold nanobumps on glass in top view. Close-up SEM images of the (b) gold nanobump in the boxed region in panel a and (c) a gold nanocone in oblique view.

SHG signal, appropriate optical filters, a tube lens and a cooled photomultiplier tube were used. The SHG origin of the signal was verified before imaging by measuring the quadratic dependence of the signal on the laser intensity. A bright-field imaging arm was also implemented to view the sample area of interest. The 800 nm diameter of the beam focus permitted us to collect signals from individual nanoparticles that are free from coupling effects due to indirect excitation of neighboring particles.[47] Moreover, the spot size used was always smaller than the period of the imaged arrays. To achieve AP or RP laser beams with high polarization purity, a radial polarization converter (ARCoptix, S.A.) and a spatial filter in tandem before the dichroic filter were used. Throughout the imaging experiments, average power levels of less than 5 mW were used. The power levels were verified to be below the damage threshold of the samples by comparing the SEM images acquired before and after SHG imaging.

To address the origin of the SHG response from the nanobumps and nanocones, we performed surface SHG modeling based on the frequency-domain BEM.[48] Here, the electromagnetic scattering problem was formulated by using the Stratton−Chu integral operators and by enforcing the interface conditions on the particle surface. To obtain approximate solutions, the problem was discretized by using the Method of Moments with Galerkin's testing. The Rao−Wilton−Glisson basis functions were chosen meaning that the particle surface was described by a triangle mesh and the representation of the tangential components of the electric and magnetic fields on the surface was of first order.

BEM allows a focused beam to be used as an excitation source. Furthermore, the construction and factorization of the dense system matrix, which are the most time-consuming parts of the method, were done only once per beam scan image. When the beam location was shifted, only the source vector needed to be re-evaluated. Thus the measured beam scan images could be simulated within reasonable computation times. In the computations, the measured refractive index of gold reported by Johnson and Christy was used.[49] The surrounding medium was taken to be vacuum and for simplicity, the substrate was neglected. The far-field optical images for a nanobump and a nanocone with different

morphologies were calculated at the fundamental and second-harmonic frequencies. The signal was collected in reflection as the beam was scanned over a 1.5 × 1.5 μm^2 sized area centered on the particle. The NA was set to 0.8 and the filling factor was set to 1. To qualitatively represent an ideal particle, the dimensions of the nanobump and nanocone triangle meshes were deduced from the SEM and AFM measurements.

For comparison, we also acquired SHG images of the array depicted in Figure 1a using a linearly polarized (LP) beam (Figure 2a). At the location of the nanobumps, single bright

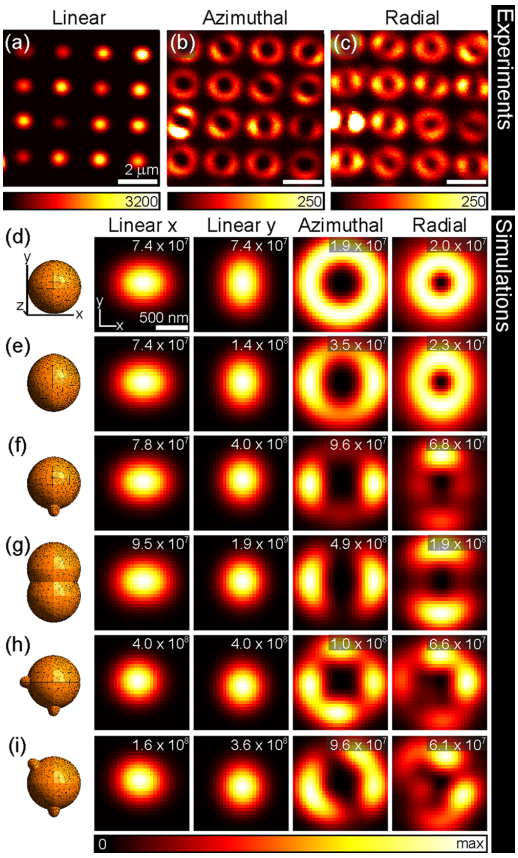

Figure 2. Experimental SHG images of gold nanobumps using focused (a) LP, (b) AP, and (c) RP beams. Calculated far-field SHG images of an (d) ideal nanobump, (e) nanobump with asymmetric base, and (f–i) nanobumps with a bump defect at different configurations using focused LP along *x*, LP along *y*, AP, and RP beams. The calculated images are normalized to the incident beam amplitude and their maximum intensity values (au) are shown. The different triangle meshes used in the calculations are also shown.

spots are seen, which are associated with the excitation of LSPs that oscillate at the plane of the nanobump base. These in-plane LSP oscillations are induced by the transverse field components of the focused LP beam, which is dominantly polarized along the polarization direction of the unfocused beam. Although the observed variations of the SHG intensity levels can indicate possible anisotropy due to the noncircular base, it is difficult to distinguish the direction of in-plane anisotropy of the individual nanobumps based on a single image using a LP beam. Conventionally, the in-plane orientation of an anisotropic nano-object, for example, a nanorod, can be inferred from several images acquired by varying the polarization direction of the LP beam with the additional costs in measurement time and image processing.

Shown in Figures 2b and 2c are the SHG images of the same region using focused AP and RP beams. At the exact location of the nanobumps, dark spots were observed due to the lack of exciting transverse field components of the focused beams. In addition, the absence of SHG intensities at the exact location of the nanobumps using the focused RP beam implied that the excited out-of-plane LSP oscillations did not lead to significant SHG at the chosen excitation wavelength, due to the bluntness of the tips of the nanobumps resulting in small and relatively weak local-field enhancements. This is in contrast with conical structures with sharp tips, where the longitudinal field component of the focused RP beam couples strongly with the tip axis.[2] Thus, doughnut-shaped intensity patterns which surround the dark spots are expected when an ideal nanobump is imaged by focused CVBs. However, for AP excitation, we also observed doughnut-shaped intensity patterns with two enhanced lobes that surround the dark spot. Similar patterns rotated by 90° were evident in the SHG images using the RP beam. We associated these patterns with possible in-plane anisotropy of the nanobump base.

We then calculated the SHG far-field images for an ideal nanobump and nanobumps with varied morphologies under focused LP, AP and RP beams (Figures 2d–i). For the ideal nanobump (Figure 2d), a height of 80 nm and a circular base with diameter of 160 nm was chosen corresponding to an average fabricated nanobump. For the defective nanobump cases, we considered nanobumps with an asymmetric base (Figure 2e) and nanobumps with a small defect at different configurations (Figures 2f–i). For the nanobump with asymmetric base, a height of 80 nm and an ellipsoidal base with a length ratio of 1.1 of the major (176 nm) and minor axes (160 nm) was selected. For the nanobump with a small defect, a small bump positioned at one side of the ideal nanobump was used (Figure 2f). To demonstrate the effect of defect size, an additional nanobump case with a large bump (Figure 2g) defect was used. To examine the role of multiple sources of anisotropy that contribute to symmetry breaking, two nanobumps with two small and same-sized defects that are locally positioned at the base of the nanobump were used. Both of these nanobumps exhibit a small bump positioned at one side of the ideal nanobump along the *y*-axis and differ only in the position of the second small bump. Here, we only considered the cases where the symmetry planes differ by 22.5° with respect to the *z*-axis (Figures 2h and 2i).

The different nanobump cases are distinguished poorly by a focused LP beam with strong polarizations along the *x*- and *y*-axes. Although the use of a focused LP beam with strong polarization along the *y*-axis changed slightly the maximum intensity values and Gaussian-like images, a single SHG image using a focused LP beam is not sufficient to discriminate ideal and defective nanobumps. Moreover with LP, the ellipticity of the image is in the range of 0–19%, where the actual value will be difficult to distinguish in practice.

Under focused CVBs however, the ideal and defective nanobumps are clearly discriminated. The SHG images of an

dx.doi.org/10.1021/nl301190x | *Nano Lett.* 2012, 12, 3207–3212

ideal nanobump resemble perfect doughnut-shaped patterns (Figure 2d) as expected from the radial symmetry of the CVBs and the highly symmetric nanobump. Moreover due to nonlinear effects, the SHG images appeared to have narrower line widths than the scattering images obtained at the fundamental wavelength (Supporting Information).[18] On the other hand, the SHG images of the defective nanobumps (Figures 2e–i) corresponded to asymmetric and distorted doughnut-shaped images, which can be correlated with the properties and location of the defect.

When a nanobump with asymmetric base with a major axis along the *y*-axis (Figure 2e) is considered, the AP and RP beams resulted in different images, which indicated the presence of in-plane anisotropy at the nanobump base along the *y*-axis. Furthermore due to the radial symmetry of the CVBs, it is expected that a nanobump with asymmetric base with a major axis along the *x*-axis results in similar SHG images that are perpendicular to the previous case (Supporting Information). For an asymmetric nanobump imaged by AP (RP) beam, the line segment connecting the two enhanced lobes in the doughnut-shaped SHG image was found to be oriented perpendicular (parallel) to its longer axis. Similar images were observed for a highly anisotropic structure as exemplified by a nanorod with an in-plane aspect ratio of 2 (Supporting Information). Analogously for a metal nanorod imaged by a focused AP (RP) beam under linear excitation, the line segment connecting the two intensity lobes was found to be oriented perpendicular (parallel) to its longer axis.[44,45] Although low degrees of in-plane asymmetry can be also seen under linear scattering with CVBs (Supporting Information), the inherent properties of SHG with CVBs can provide more sensitivity for microscopy as we will show in the following discussions.

When a nanobump with a small bump positioned at one side of the ideal nanobump along the *y*-axis was considered (Figure 2f), the AP and RP beams yielded very distinctive SHG images agreeing well with the SHG experiment. Similarly, due to the radial symmetry of the CVBs, a nanobump with a small bump positioned along the *x*-axis produced asymmetric doughnut-shaped SHG images rotated by 90° (Supporting Information). Again, the line segment connecting the two enhanced lobes in the doughnut-shaped SHG images using the AP (RP) beam indicated the shorter (longer) axis of the nanobump. Moreover, the unequal intensities of the enhanced lobes indicated the presence of a clear defect at the nanobump base, which modified the expected SHG signals. We further note that the asymmetries in the enhanced lobes are affected by the size of the bump defect. At the extreme case where the bump defect is as large as the original bump (Figure 2g), the SHG images would resemble the response of an asymmetric nanoparticle similar to a rod.

At this point, we emphasize that other kinds of shape variations and defects in the nanobumps can cause additional deviations from the expected SHG patterns due to the shifts in the LSP resonances (Figures 2h and 2i). However, based on these results, nanobumps with the considered morphologies can be well resolved by SHG microscopy with CVBs. Such capability will be essentially impossible to achieve without introducing nonlinearity in the excitation scheme with CVBs (Supporting Information).

Next, we imaged nanocones using SHG microscopy. The SHG images of the nanocone in Figure 1c using AP and RP beams are shown in Figures 3a and 3b, respectively. The SHG

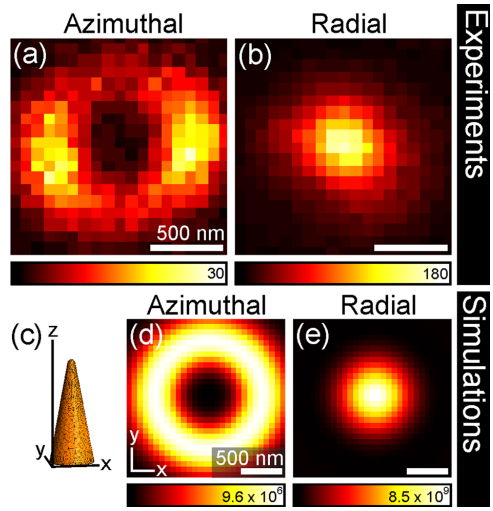

Figure 3. Experimental SHG images of a gold nanocone in Figure 1c using focused (a) AP and (b) RP beams. The triangle mesh used for the ideal nanocone is shown in (c). Calculated far-field SHG images of an ideal nanocone using focused (d) AP and (e) RP beams. The calculated images are separately normalized to the incident beam amplitude and their maximum intensity values (au) are shown.

image of the nanocone using the AP beam resulted in a doughnut-shaped intensity pattern. The slight asymmetry of the SHG pattern was attributed to anisotropy and defects at the nanocone base. On the other hand, the SHG image using the RP beam gave rise to a Gaussian-like image centered at the location of the nanocone. The SHG signals are associated with the excitation of LSPs along the cone axis further strengthened by the lightning-rod effect. The experimental SHG images agreed well with the calculated SHG images (Figures 3d and 3e). In the calculations, a triangle mesh for an ideal nanocone with a height of 300 nm, a tip diameter of 20 nm and a circular base with diameter of 150 nm was used. Additionally, we note that the cone functions as a probe of the fields polarized along the cone axis and the resulting image distribution arises from the SHG signal of an effective dipole oriented along the cone axis as verified previously.[21]

We then tested the sensitivity of the imaging technique to nanocones with different orientation and morphology (Supporting Information). Shown in Figure 4a is a SEM image of an array of nanocones with a period of 2 μm with labels that indicate representative cases of normal (C2, C3, C4, C5, and C7) and bent nanocones (C1 and C6). SHG microscopy images of the chosen region using AP and RP beams are depicted in Figures 4d and 4e, respectively. Focusing an AP beam led to doughnut-shaped intensity patterns surrounding the nanocones (Figure 4d). As noted earlier, the asymmetry in the doughnut-shaped patterns using an AP beam indicates in-plane anisotropy of the nanocone base. Furthermore, the variation in the collected signals suggests the influence of the SHG response that arises from the coupling of the transverse field components of the AP focus to other sources of in-plane anisotropy such as bent tips as seen in the SHG images of the bent nanocones.

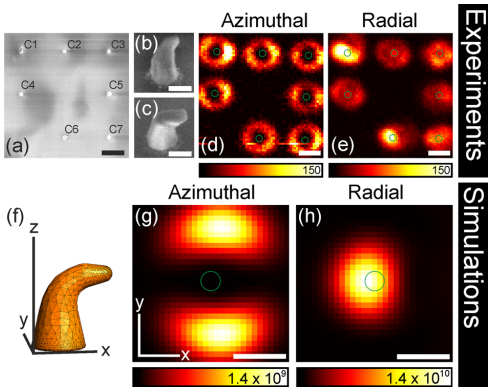

Figure 4. (a) Top view SEM image of a region in the fabricated array of gold nanocones. Oblique SEM images of bent nanocones (b) C1 and (c) C6. SHG images of the same region using focused (d) AP and (e) RP beams. The triangle mesh used for the bent nanocone is shown in (f). Calculated far-field SHG images of bent nanocone using focused (g) AP and (h) RP beams. The calculated images are separately normalized to the incident beam amplitude and their maximum intensity values (au) are shown. The length of the scale bars corresponds to (a,d,e) 1 μm, (b,c) 150 nm, and (g,h) 500 nm. For clarity, the locations of the nanocones are marked with green circles in (d,e,g,h).

On the other hand, focusing a RP beam resulted in varying SHG intensity patterns (Figure 4e). As discussed earlier, nonvanishing intensities at the exact location of the nanocones are observed due to the excitation of LSPs along the nanocone axis. However, the observed variation in the SHG intensities indicates possible shifts in the LSPs of the individual nanocones due to differences in height (Supporting Information). Upon verification using AFM, the heights of nanocones C1, C2, C3, C4, C5, C6, and C7 were found to be 206, 452, 302, 426, 360, 235, and 352 nm, respectively. Furthermore, the collected signals may be influenced by differences in tip sharpness, presence of defects near the tips, and in-plane anisotropy of the nanocones that distort the expected SHG images. In addition, the SHG signals from the bent nanocones under a RP focus were found to be stronger than the other cones (~1 order of magnitude), suggesting the excitation of polarization dependent resonances of the bent cones under inhomogeneous field distributions (Supporting Information).

In order to provide understanding of the results in Figures 4d and 4e, we simulated the SHG responses from a bent nanocone. We used the nanocone model with the height of 300 nm and a slightly larger tip diameter (~40 nm) that is deformed in the *x*-direction. By considering the case of such lowered symmetry, we predict the occurrence of polarization dependent resonances, not present in the ideal cone (Supporting Information). The calculated SHG image of the bent nanocone using the AP beam yielded two asymmetric lobes due to coupling of the transverse fields with the LSPs of the bent nanocone and agreed well with experiment (Figure 4g). The calculated SHG image using the RP beam, on the other hand, resulted in an asymmetric Gaussian-shaped image (Figure 4h) where the hotspot is locally shifted away from the bent tip and agreed well with the experiment. The inhomogeneous field distribution of a focused RP beam is expected to be more sensitive to the location and features of the bent nanocone than the transverse field distribution of a focused AP beam. Thus depending on the morphology and location of the bent nanocones under the RP beam focus, polarization-dependent LSP oscillations that contribute to the overall SHG response are excited (Supporting Information). Nevertheless, we emphasize that the imaging technique is very sensitive to the 3D orientation and morphology of the metal nano-objects. Generally, by comparing the simulated scattering images of the nanocone at the fundamental and second-harmonic wavelengths, we see that the latter ones have more contrast to them (Supporting Information). Therefore, the technique provides contrast for structural features that cannot be resolved by linear techniques or conventional states of polarization.

In conclusion, we have demonstrated an imaging technique that is extremely sensitive to the 3D orientation and morphology of individual metal nano-objects. Our method is based on SHG microscopy using CVBs. We correlated our SHG experiments with SEM images and performed second-harmonic field calculations based on frequency-domain BEM. The experimental results agree well with calculations. Our technique allows precise characterization of individual nano-objects in the far-field, which provides an alternative to complicated near-field approaches. In addition, we emphasize that independent of the quantitative analysis the real value of our experimental technique arises from the fact that its qualitative properties provide information that is not available from alternative techniques. Furthermore, the technique opens additional avenues for subwavelength field shaping in the vicinity of plasmonic nanostructures[50] and furthers optimization of fabrication models and nanoparticle architectures with distinct and tailorable plasmonic properties.[25]

■ ASSOCIATED CONTENT

Supporting Information

Additional discussions related to the experiments and SHG modeling based on BEM for the nanobumps and nanocones are provided. This material is available free of charge via the Internet at http://pubs.acs.org.

■ AUTHOR INFORMATION

Corresponding Author

*E-mail: godofredo.bautista@tut.fi.

Notes

The authors declare no competing financial interest.

■ ACKNOWLEDGMENTS

This work was supported by Grants 134973 and 135084 from the Academy of Finland. M.J.H. acknowledges support from the Graduate School of Modern Optics and Photonics in Finland and Emil Aaltonen Foundation. J.M. and J.M.K. acknowledge support from the Graduate School of the Tampere University of Technology.

■ REFERENCES

(1) Novotny, L.; Hecht, B. *Principles of Nano-Optics*; Cambridge University Press: New York, 2006.
(2) Novotny, L.; Bian, R. X.; Xie, X. S. *Phys. Rev. Lett.* **1997**, *79*, 645.
(3) Romero, I.; Aizpurua, J.; Bryant, G. W.; García De Abajo, F. J. *Opt. Express* **2006**, *14*, 9988.
(4) Tabor, C.; Van Haute, D.; El-Sayed, M. A. *ACS Nano* **2009**, 3, 3670.

(5) Wang, H.; Wu, Y.; Lassiter, B.; Nehl, C. L.; Hafner, J. H.; Nordlander, P.; Halas, N. J. *Proc. Natl. Acad. Sci. U.S.A.* **2006**, *103*, 10856.
(6) Fedotov, V. A.; Rose, M.; Prosvirnin, S. L.; Papasimakis, N.; Zheludev, N. I. *Phys. Rev. Lett.* **2007**, *99*, 147401.
(7) Christ, A.; Martin, O. J. F.; Ekinci, Y.; Gippius, N. A.; Tikhodeev, S. G. *Nano Lett.* **2008**, *8*, 2171.
(8) Nelayah, J.; Kociak, M.; Stephan, O.; García de Abajo, F. J.; Tence, M.; Henrard, L.; Taverna, D.; Pastoriza-Santos, I.; Liz-Marzan, L. M.; Colliex, C. *Nat. Phys.* **2007**, *3*, 348.
(9) Vesseur, E. J. R.; De Waele, R.; Kuttge, M.; Polman, A. *Nano Lett.* **2007**, *7*, 2843.
(10) Olmon, R. L.; Krenz, P. M.; Jones, A. C.; Boreman, G. D.; Raschke, M. B. *Opt. Express* **2008**, *16*, 20295.
(11) Brüche, E. *Z. Phys.* **1933**, *86*, 448.
(12) Beversluis, M. R.; Bouhelier, A.; Novotny, L. *Phys. Rev. B* **2003**, *68*, 115433.
(13) Fleischer, M.; Stanciu, C.; Stade, F.; Stadler, J.; Braun, K.; Heeren, A.; Häffner, M.; Kern, D. P.; Meixner, A. J. *Appl. Phys. Lett.* **2008**, *93*, 111114.
(14) García de Abajo, F. J. *Rev. Mod. Phys.* **2010**, *82*, 209.
(15) Vogelgesang, R.; Dmitriev, A. *Analyst* **2010**, *135*, 1175.
(16) Bouhelier, A.; Beversluis, M. R.; Novotny, L. *Appl. Phys. Lett.* **2003**, *83*, 5041.
(17) Danckwerts, M.; Novotny, L. *Phys. Rev. Lett.* **2007**, *98*, 026104.
(18) Zayats, A. V.; Sandoghdar, V. *J. Microsc.* **2001**, *202*, 94.
(19) Butet, J.; Duboisset, J.; Bachelier, G.; Russier-Antoine, I.; Benichou, E.; Jonin, C.; Brevet, P.-F. *Nano Lett.* **2010**, *10*, 1717.
(20) Takahashi, S.; Zayats, A. V. *Appl. Phys. Lett.* **2002**, *80*, 3479.
(21) Bouhelier, A.; Beversluis, M.; Hartschuh, A.; Novotny, L. *Phys. Rev. Lett.* **2003**, *90*, 013903.
(22) Lippitz, M.; van Dijk, M. A.; Orrit, M. *Nano Lett.* **2005**, *5*, 799.
(23) Kim, S.; Jin, J.; Kim, Y.-J.; Park, I.-Y.; Kim, Y.; Kim, S.-W. *Nature* **2008**, *453*, 757.
(24) Canfield, B. K.; Husu, H.; Kontio, J.; Viheriälä, J.; Rytkönen, T.; Niemi, T.; Chandler, E.; Hrin, A.; Squier, J. A.; Kauranen, M. *New J. Phys.* **2008**, *10*, 013001.
(25) Husu, H.; Siikanen, R.; Mäkitalo, J.; Lehtolahti, J.; Laukkanen, J.; Kuittinen, M.; Kauranen, M. *Nano Lett.* **2012**, *12*, 673.
(26) Canfield, B. K.; Kujala, S.; Jefimovs, K.; Turunen, J.; Kauranen, M. *Opt. Express* **2004**, *12*, 5418.
(27) Canfield, B. K.; Husu, H.; Laukkanen, J.; Bai, B.; Kuittinen, M.; Turunen, J.; Kauranen, M. *Nano Lett.* **2007**, *7*, 1251.
(28) Feth, N; Linden, S.; Klein, M. W.; Decker, M.; Niesler, F. B. P.; Zeng, Y.; Hoyer, W.; Liu, J.; Koch, S. W.; Moloney, J. V.; Wegener, M. *Opt. Lett.* **2008**, *33*, 1975.
(29) Valev, V. K.; Smisdom, N.; Silhanek, A. V.; De Clercq, B.; Gillijns, W.; Ameloot, M.; Moshchalkov, V. V.; Verbiest, T. *Nano Lett.* **2009**, *9*, 3945.
(30) Huttunen, M. J.; Bautista, G.; Decker, M.; Linden, S.; Wegener, M.; Kauranen, M. *Opt. Mater. Express* **2011**, *1*, 46.
(31) Kontio, J. M.; Husu, H.; Simonen, J.; Huttunen, M. J.; Tommila, J.; Pessa, M.; Kauranen, M. *Opt. Lett.* **2009**, *34*, 1979.
(32) Wang, H.; Goodrich, G. P.; Tam, F.; Oubre, C.; Nordlander, P.; Halas, N. J. *J. Phys. Chem. B* **2005**, *109*, 11083.
(33) Canfield, B. K.; Kujala, S.; Laiho, K.; Jefimovs, K.; Turunen, J.; Kauranen, M. *Opt. Express* **2006**, *14*, 950.
(34) Husu, H.; Canfield, B. K.; Laukkanen, J.; Bai, B.; Kuittinen, M.; Turunen, J.; Kauranen, M. *Appl. Phys. Lett.* **2008**, *93*, 183115.
(35) Klein, M. W.; Enkrich, C.; Wegener, M; Linden, S. *Science* **2006**, *313*, 502.
(36) van Nieuwstadt, J. A. H.; Sandtke, M.; Harmsen, R. H.; Segerink, F. B.; Prangsma, J. C.; Enoch, S; Kuipers, L. *Phys. Rev. Lett.* **2006**, *97*, 146102.
(37) McMahon, M. D.; Lopez, R.; Haglund, R. F.; Ray, E. A.; Bunton, P. H. *Phys. Rev. B* **2006**, *73*, 041401.
(38) Kogelnik, H.; Li, T. *Appl. Opt.* **1966**, *5*, 1550.
(39) Youngworth, K. S.; Brown, T. G. *Opt. Express* **2000**, *7*, 77.
(40) Dorn, R.; Quabis, S.; Leuchs, G. *Phys. Rev. Lett.* **2003**, *91*, 233901.
(41) Novotny, L.; Beversluis, M. R.; Youngworth, K. S.; Brown, T. G. *Phys. Rev. Lett.* **2001**, *86*, 5251.
(42) Chizhik, A. I.; Chizhik, A. M.; Khoptyar, D.; Bär, S.; Meixner, A. J. *Nano Lett.* **2011**, *11*, 1131.
(43) Chizhik, A. M.; Chizhik, A. I.; Gutbrod, R.; Meixner, A. J.; Schmidt, T.; Sommerfeld, J.; Huisken, F. *Nano Lett.* **2009**, *9*, 3239.
(44) Failla, A. V.; Qian, H.; Qian, H.; Hartschuh, A.; Meixner, A. J. *Nano Lett.* **2006**, *6*, 1374.
(45) Züchner, T.; Failla, A. V.; Steiner, M.; Meixner, A. J. *Opt. Express* **2008**, *16*, 14635.
(46) Yew, E. Y. S.; Sheppard, C. J. R. *Opt. Commun.* **2007**, *275*, 453.
(47) Khunsin, W.; Brian, B.; Dorfmuller, J.; Esslinger, M.; Vogelgesang, R.; Etrich, C.; Rockstuhl, C.; Dmitriev, A.; Kern, K. *Nano Lett.* **2011**, *11*, 2765.
(48) Mäkitalo, J.; Suuriniemi, S.; Kauranen, M. *Opt. Express* **2011**, *19*, 23386.
(49) Johnson, P. B.; Christy, R. W. *Phys. Rev. B* **1972**, *6*, 4370.
(50) Juan, M. L.; Righini, M.; Quidant, R. *Nat. Photonics* **2011**, *5*, 349.

Paper 5

Mikko J. Huttunen, Jouni Mäkitalo, Godofredo Bautista, and Martti Kauranen.

Multipolar second-harmonic emission with focused Gaussian beams

New Journal of Physics **14**, 113005 (2012)

doi: 10.1088/1367-2630/14/11/113005

New Journal of Physics
The open access journal for physics

Multipolar second-harmonic emission with focused Gaussian beams

Mikko J Huttunen[1], **Jouni Mäkitalo, Godofredo Bautista and Martti Kauranen**

Department of Physics, Tampere University of Technology, FI-33101 Tampere, Finland
E-mail: mikko.j.huttunen@tut.fi

New Journal of Physics **14** (2012) 113005 (10pp)
Received 27 June 2012
Published 7 November 2012
Online at http://www.njp.org/
doi:10.1088/1367-2630/14/11/113005

Abstract. We show that electric-dipole-allowed surface second-harmonic (SH) generation with focused Gaussian beams can be described in terms of Mie-type multipolar contributions to the SH signal. In contrast to the traditional case, where Mie multipoles arise from field retardation across nanoparticles, the multipoles here arise from the confined source volume and the tensorial properties of the SH response. We demonstrate this by measuring strongly asymmetric SH emission into reflected and transmitted directions from a nonlinear thin film with isotropic surface symmetry, where symmetric emission is expected using traditional formalisms based on plane-wave excitation. The proposed multipole approach provides a convenient way to explain the measured asymmetric emission. Our results suggest that the separation of surface and bulk responses, which have dipolar and higher-multipolar character, respectively, may be even more difficult than thought. On the other hand, the multipolar approach may allow tailoring of focal conditions in order to design confined and thin nonlinear sources with desired radiation patterns.

S Online supplementary data available from stacks.iop.org/NJP/14/113005/mmedia

[1] Author to whom any correspondence should be addressed.

Contents

1. Introduction

The optical responses of materials are usually described by considering only electric-dipole interactions between light and matter. Such an electric-dipole approximation is justified by the fact that the higher-multipole interactions, most importantly magnetic-dipole and electric-quadrupole interactions, tend to be much weaker [1]. Such interactions, however, need to be considered, e.g., to explain optical activity of chiral materials [2].

For the case of nanostructured materials, one needs to consider two different types of multipole effects. The first arises from the atomic-level light–matter interaction Hamiltonian [3] and the other from Mie scattering theory even when the atomic-level interaction has purely electric-dipole origin [4]. In the latter case, retardation of electromagnetic fields across nanoscale particles gives rise to effective multipole terms in the scattering pattern. Although Mie theory is usually associated with spherical particles, it is possible to show that any scattering pattern outside a finite sphere enclosing the sources can always be expanded in similar multipole terms [1, p 439]. Multipole effects can become considerable when the particle sizes are comparable to wavelength, as recent studies of nanoparticles have shown [5–12]. But a complete understanding of such phenomena is still lacking in order to utilize multipole effects in applications such as in metamaterials or optical antennas [13–15].

Multipole effects have particular importance in nonlinear optics, because second-order nonlinear effects are electric-dipole-forbidden in centrosymmetric materials [16]. A dipole-allowed second-order signal can therefore arise only from the broken symmetry at the material surface or interface [17]. The second-order effects, however, can also occur in the bulk of centrosymmetric materials due to magnetic and quadrupole effects. Separation between the surface and the bulk effects has been notoriously difficult [18–20], only recently achieved in an unambiguous and quantitative way [21, 22]. Effective, Mie-type multipoles can also play a role in nonlinear optics as shown by several nonlinear studies from colloids and arrays of nanoparticles [5–12, 23–28].

Independent of their atomic-level or effective origin, the various multipole sources differ with regard to their far-field radiation patterns and polarization [1]. More specifically, interference between appropriate multipole terms can be used to control the directionality of the radiation pattern [14, 24]. In nonlinear optics, this could lead to nanoscale sources, in other words optical antennas, with emission enhanced in one direction and suppressed in the opposite direction. In traditional nonlinear optics, this is only possible through phase-matching effects, which require samples much larger than wavelength.

In this paper, we show that multipole effects can occur also due to the finite profile of focused Gaussian laser beams. In addition, we show that the multipole effects can even be efficiently controlled in nonlinear optics by using focused Gaussian beams, although the atomic-level light–matter interaction has an electric-dipole origin. The source region is then inhomogeneous and limited by diffraction to the scale of a wavelength. On the other hand, from the viewpoint of far-field radiation, the source region is well confined, implying that the radiation pattern can be expressed as a multipole expansion, where a number of multipoles are expected to contribute to the total radiation pattern. We demonstrate these effects by measuring second-harmonic generation (SHG) from thin films of silicon nitride (SiN), which have the symmetry of an isotropic surface. The experiments are performed using focused Gaussian TEM_{00} beams at normal incidence. By fully accounting for the vector properties of the spatially varying focal fields and the tensorial character of the nonlinearity, we observe strong differences between the SHG signals emitted in the transmitted and reflected directions. The results are shown to be compatible with the characteristics of the effective multipole moments of the source distribution.

2. Theory and simulations

In order to understand qualitatively how focused beams lead to effective multipole effects, we write the second-harmonic (SH) polarization at a frequency ω in the form

$$\mathbf{P}(\mathbf{r}) = \epsilon_0 \chi^{(2)}(\mathbf{r}) : \mathbf{E}(\mathbf{r})\mathbf{E}(\mathbf{r}) \; \forall \mathbf{r} \in \mathbb{R}^3, \tag{1}$$

where $\mathbf{E}$ is the field at the fundamental frequency $\omega/2$, $\chi^{(2)}_{ijk}$ is the second-order susceptibility tensor for SHG and $\mathbf{r} = (x, y, z)$ denotes the position vector in the three-dimensional Euclidean space $\mathbb{R}^3$. This form represents the traditional electric-dipole approach to nonlinear optics, where the fields and the nonlinear source polarization are spatially varying [29, 30]. For the case when the fundamental beam is a focused Gaussian beam, the source polarization decays rapidly in space and can be expressed using the Helmholtz decomposition as [1, p 241]

$$\mathbf{P} = \mathbf{P}_v + \nabla \times \mathbf{P}_p, \tag{2}$$

where $\nabla \times \mathbf{P}_p$ is the divergence-free and $\mathbf{P}_v$ is the curl-free part. In the presence of nonlinear magnetization $\mathbf{M}$, the effective source polarization would be of the form [19]

$$\mathbf{P}_{\text{eff}} = \mathbf{P} + \frac{1}{\omega^2 \mu} \nabla \times \mathbf{M}, \tag{3}$$

where μ is the permeability. Comparison of equations (2) and (3) thus suggests that the divergence-free part of the polarization is equivalent to a magnetic source term.

The connection between the spatially varying sources and the multipole approach can be made explicit by expressing the electric component of the emitted field at the SH frequency as [1, p 431]

$$\mathbf{E}_{SH} = \eta \sum_{l=1}^{\infty} \sum_{m=-l}^{l} \left[\frac{\mathrm{i}}{k} a^{E}_{l,m} \nabla \times h^{(1)}_l(kr) \mathbf{X}_{l,m} + a^{M}_{l,m} h^{(1)}_l(kr) \mathbf{X}_{l,m} \right], \quad r = |\mathbf{r}| > R, \tag{4}$$

where $a^{\mathrm{E}}_{l,m}$ and $a^{\mathrm{M}}_{l,m}$ are electric and magnetic multipole moments, respectively, $\mathbf{X}_{l,m}$ are the vector spherical harmonics (functions of the spherical polar angles), $h^{(1)}_l$ are the spherical Hankel functions of the first kind and lth order, η is the intrinsic impedance and k is the

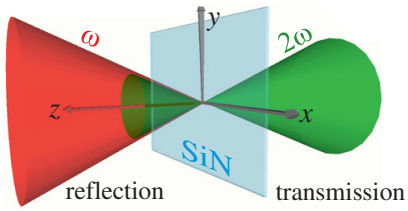

Figure 1. Schematic representation of the focusing scheme and the coordinates used. For the case of a thin, homogeneous surface sample, the SH emission is traditionally thought to be symmetric.

wavenumber of the SH field. The sources are required to vanish outside a sphere S of radius R. The time-dependence $\exp(-\mathrm{i}\omega t)$ is also assumed. Note that the electric (magnetic) moments of successive orders have opposite parity, whereas the electric and magnetic terms of a given order also have opposite parity [1, p 436]. An obvious way to control the directional properties of the emission is therefore to interfere an electric dipole source with a magnetic dipole and/or electric quadrupole. The multipole moments are obtained from the electric-dipole sources as (for the derivation see the supplementary data, available from stacks.iop.org/NJP/14/113005/mmedia)

$$a^E_{l,m} \propto \int_S Y^*_{l,m} \left(-c\nabla \cdot \mathbf{P} \frac{\partial}{\partial r}(r j_l(kr)) + k\omega \mathbf{r} \cdot \mathbf{P} j_l(kr) \right) \mathrm{d}V, \tag{5}$$

$$a^M_{l,m} \propto \int_S Y^*_{l,m} \mathbf{r} \cdot (\nabla \times \mathbf{P}) j_l(kr) \mathrm{d}V, \tag{6}$$

where $Y_{l,m}$ are the spherical harmonics and j_l are the spherical Bessel functions of the first kind and lth order [1, p 441]. Note that for sources confined to volumes much less than wavelength $kr \ll 1$, the second term of the integrand in equation (5) vanishes. For $l = 1$ the first term becomes $\nabla \cdot \mathbf{P} Y^*_{1,m} r$, and its integration yields the components of the total dipole moment in the volume. For larger sources, the interpretation is more complicated, because a number of electric and magnetic multipoles can contribute to the emission in the far field. The interpretation of equation (6) is always relatively straightforward, i.e. an effective magnetic moment arises from the curl of the source polarization. Thus we see that in general a non-zero $\nabla \times \mathbf{P}$ is required to obtain a magnetic response.

In order to demonstrate these general principles and study the role of $\nabla \times \mathbf{P}$ in SHG, we use samples with isotropic achiral surface symmetry. Such samples have the highest possible surface symmetry and thus provide a convenient model case to investigate the role of the various multipoles in the nonlinear response. Our samples are thin films (20 and 50 nm thicknesses) of amorphous SiN, prepared by depositing SiN on fused silica substrates using plasma enhanced chemical vapor deposition [33]. Such samples have full rotational symmetry about the film normal. They are therefore equivalent to isotropic surfaces with the non-vanishing components of the electric-dipole susceptibility tensor $\chi^{(2)}_{ijk}$ as zzz, $zxx = zyy$ and $xxz = xzx = yyz = yzy$, where z is the film normal (figure 1). In addition, phase matching issues can be neglected because of the small film thickness. The focusing conditions correspond to normal incidence, numerical aperture (NA) of 0.8 and a pupil filling factor of 1. Note that the focusing conditions

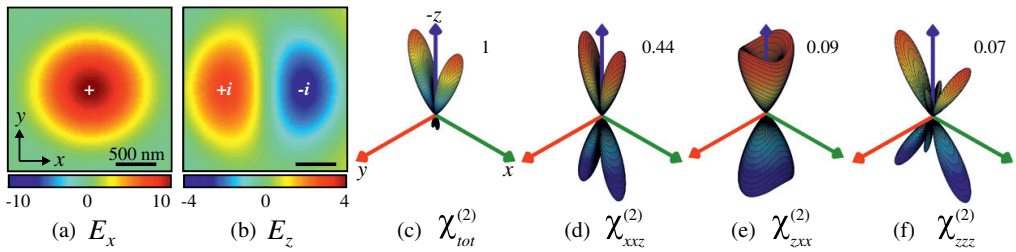

Figure 2. Calculated amplitudes of (a) x- and (b) z-components of the fundamental electric field and the corresponding radiated SH powers per unit solid angle from the isotropic SiN surface (c–f). The field amplitudes in panels (a) and (b) are normalized to 10. The tensor components used in the calculations are indicated in plots (c–f). The numbers beside the patterns denote the maximum values of the emitted power, normalized to the maximum value of the full $\chi^{(2)}$ tensor case.

give rise to longitudinal (z direction) field components required for coupling with the present susceptibility tensor at normal incidence.

For a qualitative understanding, we first consider an x-polarized fundamental beam and calculate the resulting electric field at the waist of the focused beam using an angular spectrum representation (figures 2(a) and (b)). The normal (z) component of the focal field is odd in x, i.e. it consists of two lobes with opposite phases. The other components, on the other hand, are even. It is then easy to see that the nonlinear polarization $\mathbf{P}$ due to the zzz or zxx components can never be an odd function (with respect to the x coordinate) [1]. But when the xxz component and the corresponding $\mathbf{P}$ are also considered, we see that similarly to E_z, also P_x is now an odd function. This leads to a situation where the contribution from $\nabla \times \mathbf{P}$ over the interaction volume can be expected to be large.

Using equation (1), we then calculate the source polarization for SHG at the beam waist ($z = 0$), and finally the emitted SH powers per unit solid angle using both Green's function approach [31, 32] and the proposed multipole approach. As expected, both approaches led to the same results, which are shown in figures 2(c)–(f). In order to understand the origin of the directionality and the interference effects in the SH emission, we present the results separately for different susceptibility components. In the calculations, we use relative values of $zzz = 1$, $zxx = 0.19$ and $xxz = 0.2$ for the non-zero susceptibility components, corresponding to the recently measured values for the SiN films [33]. For simplicity, only free-space Green's functions are considered, since reflections due to the interfaces cannot explain the measured differences of SH emission and would only improve the quantitative accuracy of the proposed multipolar formalism. Also, the scattered fields at the fundamental frequency are neglected in the calculations since the samples are transparent and thus weakly scattering. Finally, we calculate the normalized multipole moments $a^{\mathrm{E}}_{l,m}$ and $a^{\mathrm{M}}_{l,m}$ and find that the only non-zero electric moments occur for $m = 0, \pm 2$. The non-zero magnetic moments correspond to $m = \pm 2$ and the first seven of the l terms are found to be most dominant. We note that when using isolated tensor components, the non-vanishing moments are such that corresponding multipoles have the same parity. When considering the full tensor, this condition is no longer met and interference can occur.

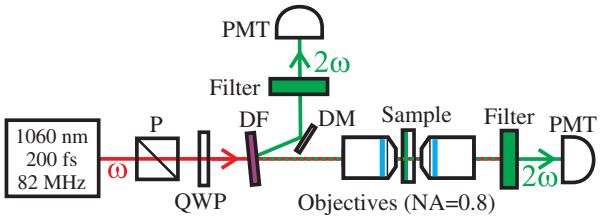

Figure 3. The setup for measuring transmitted and reflected SH emission. The fundamental beam was first linearly polarized with a polarizer (P) and passed through a rotating quarter-wave plate (QWP). In order to keep the input polarization pure, the dichroic filter (DF) was only slightly tilted from normal incidence. The reflected SHG from DF was guided to a photomultiplier tube (PMT) using a D-shaped mirror (DM). Interference filters were used in both detection arms to block the fundamental beams.

3. Experiment

In our experiments, we measure the transmitted and reflected total radiated SH powers into the far-field while changing the polarization of the input beam (figure 1). The polarization measurements are important because our calculations predict that, in addition to different SH emission strengths in the two directions, their polarization dependences are qualitatively different, allowing key evidence to be obtained even without relying on precise calibration of the signal collection efficiencies in reflection and transmission.

For measurements, a custom-built SHG microscope setup with input femtosecond laser (central wavelength at 1060 nm) providing 200 fs pulses at 82 MHz repetition frequency was used (figure 3). The fundamental beam with an average power of 10 mW was focused onto the samples with an NA = 0.8 microscope objective. The reflected SHG emission was collected by the same focusing objective, and the transmitted SH emission was collected by an additional identical microscope objective placed to the back of the sample. The collected SH emission thus corresponds now to the calculated SH powers per unit solid angle (figures 2(c)–(f)), integrated over the numerical aperture (NA = 0.8) of the collecting objectives. In addition, the use of high-NA collecting objectives is important, since there is no radiation into the strictly forward and backward directions, as can be seen in figure 2(c). The SH emission was then separated from the fundamental beam by dichroic and interference filters, and measured simultaneously by two photomultiplier tubes connected to a photon counting unit. The polarization control of the input beam was done by a rotating QWP, and measurement times of 30 s and angle steps of 5° for the QWP were used. The QWP angles of 0°, 90°, 180°, etc corresponded to linear input polarization and angles of 45°, 135°, 225° and 315° to circular input polarizations.

4. Results and discussion

First we measured SHG responses from gold nanodots (radius 75 nm) in order to calibrate the relative detection efficiencies of both detection arms. The collection efficiency for the transmitted SHG was seen to differ from that of reflected SHG by a factor of 2.13, which was used for the mutual calibration of the two SHG signals. We emphasize, however, that

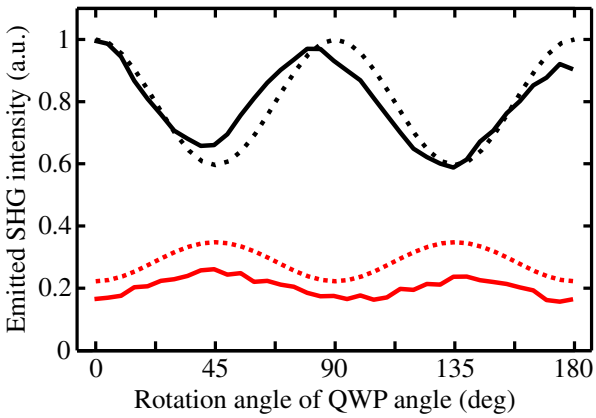

Figure 4. Measured SHG responses from an SiN thin film (thickness 50 nm) as a function of rotating QWP. The transmitted (black line) and the reflected (red line) emission clearly differ from each other and agree well with the calculations (dotted lines).

the calibration was performed only to increase the accuracy of our measurements, and is not necessary for demonstrating the effect.

After the calibration, we measured the SHG from SiN thin films. Figure 4 shows the measured and calculated SHG responses as a function of the rotation angle of the QWP from the SiN film with a thickness of 50 nm. The average ratio for transmitted and reflected SHG was measured to be 4.06, and more importantly, the polarization dependences of the reflected and transmitted SHG responses clearly differ from each other. The measured SHG responses also correspond surprisingly well with the modeled responses based on both the Green's function and the proposed multipolar approaches (see section 2 for details). For the calculations, no fitting besides normalization to the maximum of transmitted SHG response was performed.

We emphasize that our samples are highly transparent and very thin (thickness less than $\lambda/10$). Possible phase matching or Fabry–Perot issues can be ruled out due to the sample thickness, because no significant phase accumulation of the fields can occur over such a short distance. Neither can absorption explain the observed differences, since it could not explain the polarization dependences. The samples should therefore emit symmetrically in the transmitted and reflected directions. We also exclude any response from the fused silica substrate as an explanation, since we were not able to get any measurable SHG from the substrate even with input beam powers exceeding 30 mW. The most plausible explanation for the results is thus interference between multipoles of different parities, in particular between electric and magnetic multipoles. We believe that magnetic multipoles play an important role due to non-vanishing $\nabla \times \mathbf{P}$. This is also supported by the calculated multipole moments, where the magnetic moments were considerably large as is seen in figure 5.

The proposed multipole approach also provides an elegant explanation for the measured polarization dependence of the SH emission. When the input polarization changes from linear to circular, the calculated multipole moments change, respectively. The behavior is seen in figure 5(e), where the calculated multipole moments for left-handed circular input polarization

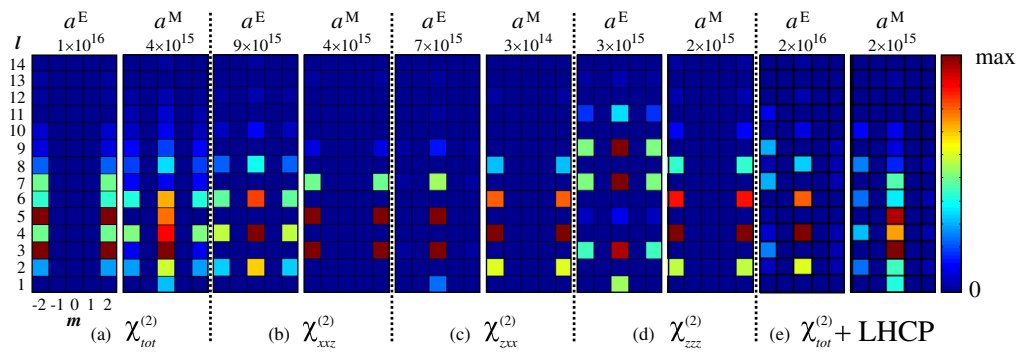

Figure 5. The magnitudes of the multipole moments of the nonlinear polarization source induced by a focused TEM_{00} beam. The tensor components used in the calculations are indicated in plots (a)–(e). The vertical axis corresponds to the l values and the horizontal axis to the m values. The numbers above the plots indicate the maximum value. It is important to note that only when (a) the full $\chi^{(2)}$ tensor is considered, multipoles with different parity arise, giving rise to interference effects. Interference effects between different multipoles can also occur when circularly polarized input beams are used (e), but are reduced compared to linearly polarized input (a).

are shown. In essence, the strengths of multipoles with different parities are reduced by changing the input polarization into circular. This leads to reduced interference effects and thus a decreased ratio between the transmitted and the reflected emission as was measured.

Our results provide new insights for understanding the connection between SHG and multipolar effects. Firstly, the results show the power of focused beam geometry and consequent theoretical formalism [32, 34], since SHG is forbidden from our samples at normal incidence and in the limit of plane-wave excitation [16]. Secondly, the results show that electric-dipole interactions can give rise to strong effective magnetic responses, if the source polarization is spatially varying and the condition $\nabla \times \mathbf{P} \neq 0$ is satisfied. In our case, this occurred when the excitation field was a focused TEM_{00} Gaussian beam and the second-order susceptibility had non-zero xxz component.

Interestingly, our results have similarities to the suggestion of Bethune already in 1981 that multimode beams could enhance the bulk responses of higher-multipole origin in surface SHG [35], as was further studied by Bernal and Maytorena [36]. In our case, however, the higher-multipole responses arise from atomic-level electric-dipole responses, and do not rely on atomic-level higher multipoles. This suggests that the dilemma of differentiating the bulk and surface contributions from each other could be even harder than previously thought, in particular when focused Gaussian beams are used. This problem is due to the fact that the separation of bulk and surface contributions in general relies on measuring either interference effects or different polarization dependences of the SH emission [21, 22, 24]. But our calculations and experimental data show that similar effects can also occur when the source volume is confined.

The results also demonstrate the general principle that the SH emission from confined volumes can be affected by tailoring the excitation, in our case the focusing, conditions.

In addition, the introduced multipole approach is expected to facilitate more arbitrary control of SH emission by providing an understanding of how certain types of multipoles could be enhanced, e.g. by utilizing higher-order vector beams.

5. Conclusion

To conclude, we have shown that traditional electric-dipole-allowed SHG can be interpreted in terms of effective higher-multipole terms when the excitation occurs using focused Gaussian beams. In particular, magnetic terms become important whenever the quantity $\nabla \times \mathbf{P}$ is non-vanishing. The approach was demonstrated using thin SiN films as the nonlinear source, where the SH emission was strongly asymmetric between the reflected and transmitted directions. Such multipolar approaches provide a way of obtaining directional nonlinear emission from confined and thin source volumes, where traditional phase matching is irrelevant. Nonlinear sources with desired radiation patterns can therefore be tailored by the choice of focal conditions to enable or suppress selected multipoles in the response.

Acknowledgments

We would like to acknowledge Outi Hyvärinen and Janne Simonen at the Optoelectronics Research Center (Finland) for kindly providing the samples. This work was funded by the Academy of Finland (project 134973). MJH acknowledges support from the Graduate School of Modern Optics and Photonics in Finland and the Emil Aaltonen Foundation. JM acknowledges support from the Graduate School of Tampere University of Technology.

References

[1] Jackson J D 1998 *Classical Electrodynamics* (New York: Wiley)
[2] Buckingham A D and Stiles P J 1974 *Acc. Chem. Res.* **7** 258–64
[3] Loudon R 1983 *The Quantum Theory of Light* (New York: Oxford University Press)
[4] Bohren C F and Huffman D R 1998 *Absorption and Scattering of Light by Small Particles* (New York: Wiley)
[5] Oldenburg S J, Hale G D, Jackson J B and Halas N J 1999 *Appl. Phys. Lett.* **75** 1063
[6] Kelly K L, Coronado E, Zhao L L and Schatz G C 2003 *J. Phys. Chem.* B **107** 668
[7] Krenn J R, Schider G, Rechberger W, Lamprecht B, Leitner A, Aussenegg F R and Weeber J C 2000 *Appl. Phys. Lett.* **77** 3379
[8] Dadap J I, Shan J and Heinz T F 2004 *J. Opt. Soc. Am.* B **21** 1328
[9] Pavlyukh Y and Hübner W 2004 *Phys. Rev.* B **70** 245434
[10] de Beer A G F and Roke S 2009 *Phys. Rev.* B **79** 155420
[11] Gonella G and Dai H-L 2011 *Phys. Rev.* B **84** 121402
[12] Roke S and Gonella G 2011 *Annu. Rev. Phys. Chem.* **63** 353
[13] Soukoulis C M, Linden S and Wegener M 2007 *Science* **315** 47
[14] Curto A G, Volpe G, Taminiau T H, Kreuzer M P, Quidant R and van Hulst N F 2010 *Science* **329** 930–3
[15] Novotny L and van Hulst N 2011 *Nature Photon.* **5** 83
[16] Boyd R W 2008 *Nonlinear Optics* (Amsterdam: Elsevier)
[17] Shen Y R 1989 *Nature* **337** 519
[18] Guyot-Sionnest P, Chen W and Shen Y R 1986 *Phys. Rev.* B **33** 8254
[19] Guyot-Sionnest P and Shen Y R 1987 *Phys. Rev.* B **35** 4420
[20] Sipe J E, Mizrahi V and Stegeman G I 1987 *Phys. Rev.* B **35** 9091

[21] Figliozzi P, Sun L, Jiang Y, Matlis N, Mattern B, Downer M C, Withrow S P, White C W, Mochàn W L and Mendoza B S 2005 *Phys. Rev. Lett.* **94** 047401
[22] Cattaneo S and Kauranen M 2005 *Phys. Rev.* B **72** 033412
[23] Nappa J, Russier-Antoine I, Benichou E, Jonin Ch and Brevet P F 2006 *J. Chem. Phys.* **125** 184712
[24] Kujala S, Canfield B K, Kauranen M, Svirko Y and Turunen J 2007 *Phys. Rev. Lett.* **98** 167403
[25] Bachelier G, Russier-Antoine I, Benichou E, Jonin C and Brevet P-F 2008 *J. Opt. Soc. Am.* B **25** 955–60
[26] Butet J, Bachelier G, Russier-Antoine I, Jonin C, Benichou E and Brevet P-F 2010 *Phys. Rev. Lett.* **105** 077401
[27] Zdanowicz M, Kujala S, Husu H and Kauranen M 2011 *New J. Phys.* **13** 023025
[28] Czaplicki R, Zdanowicz M, Koskinen K, Laukkanen J, Kuittinen M and Kauranen M 2011 *Opt. Express* **19** 26866–71
[29] Boyd G D 1968 *J. Appl. Phys.* **39** 3597
[30] Carrasco S, Saleh B E A, Teich M C and Fourkas J T 2006 *J. Opt. Soc. Am.* B **23** 2134
[31] Novotny L and Hecht B 2007 *Principles of Nano-Optics* (Cambridge: Cambridge University Press)
[32] Cheng J and Xie X S 2002 *J. Opt. Soc. Am.* B **19** 1604
[33] Ning T, Pietarinen H, Hyvärinen O, Simonen J, Genty G and Kauranen M 2012 *Appl. Phys. Lett.* **100** 161902
[34] Huttunen M J, Erkintalo M and Kauranen M 2009 *J. Opt. A: Pure Appl. Opt.* **11** 034006
[35] Bethune D S 1981 *Opt. Lett.* **6** 287
[36] Bernal R and Maytorena J A 2004 *Phys. Rev.* B **70** 125420

Tampereen teknillinen yliopisto
PL 527
33101 Tampere

Tampere University of Technology
P.O.B. 527
FI-33101 Tampere, Finland

ISBN 978-952-15-3067-8
ISSN 1459-2045